Structured Light for Quantum Sensing, Information, and Imaging.

by

Dilip Paneru

A thesis submitted to
the University of Ottawa in partial fulfillment
of the requirements for the degree of
Doctor of Philosophy
in Physics

Department of Physics
Faculty of Science
University of Ottawa

Abstract

The emergence and development of quantum optics as a discipline in the latter half of the twentieth century has established photons as one of the most promising candidates for future technologies in computing, metrology, communication, and imaging. In imaging and sensing, a series of recent theoretical works and proof-of-concept experiments have shown that by examining the mode structure of photons, one can build optical systems with resolutions below the Rayleigh–Abbe limit. Building upon these developments, in one of our works, we investigate the use of higher-order Hermite–Gauss (HG) modes for sensing optically induced transverse displacements. We show that projective measurements onto neighboring modes are optimal and sufficient in the small-displacement regime, and that the sensitivity—quantified by the Fisher information—scales linearly with the order of the mode used. We generalize the calculations to arbitrary displacements and varying degrees of coherence between the displaced modes, and perform a proof-of-concept experiment with higher-order HG modes, obtaining an order-of-magnitude enhancement in sensitivity compared to the fundamental mode. This approach enables enhanced displacement sensitivity with minimal measurements and highlights the potential of structured light for ultrasensitive displacement sensing, particularly for birefringence measurements with broadband or low-coherence light sources. We also consider displacement sensing in the light field originating from a biphoton source, which possesses rich high-dimensional correlations in its biphoton mode structure. We show that the Fisher information is proportional to the degree of entanglement, or equivalently, its Schmidt rank. In addition to sensing, photons structured in their transverse degrees of freedom also provide a convenient toolkit for quantum computing and communication due to the high dimensionality of their Hilbert space. In one of the works presented, we introduce a technique for nonlocal transfer of high-dimensional computational results using spatial correlations in photon pairs. We expect these findings to be useful in future photonic quantum networks, where computational resources are distributed and users can access the results of complex computations via a centrally located quantum processor. We also experimentally implement the protocol in down-converted photon pairs and demonstrate the transfer of unitaries in one-dimensional

and two-dimensional transverse momentum spaces. In another work, we address the noise inherent in quantum computing circuits and simulate the interaction between a qubit and its environment by manipulating transverse momentum modes. This study, performed by fabricating three liquid-crystal metasurfaces, provides a practical solution for quantum state purification, demonstrating a versatile approach for simulating open-qubit dynamics. Combining the transverse spatial structure with polarization yields the so-called vector modes of photons. Structuring two-qubit interference, or the Hong–Ou–Mandel (HOM) effect, offers significant potential to extend the applications of such modes beyond the classical regime. We demonstrate the simultaneous generation of all four Bell states in polarization by exploiting HOM interference of vector modes. These results represent a significant step toward manipulating HOM interference within structured photons, offering promising applications in high-dimensional quantum information processing, quantum communication, and sensing. On the algorithmic side of photonic information processing, we propose a quantum pattern recognition algorithm to identify images obtained from quantum imaging techniques with correlated photons—such as "interaction-free" or "ghost" imaging. Interfacing these imaging techniques with quantum pattern recognition promises a significantly improved image acquisition and identification system, with potential applications in medical diagnostics and biological imaging.

Acknowledgements

First and foremost, I am deeply grateful to my supervisor, Prof. Ebrahim Karimi, for his supervision, expert scientific guidance, and continued and generous support throughout the course of my studies. His eagerness to explore science at the fundamental level was truly inspiring and something we shared. I deeply value all our collaborative scientific adventures, as well as the many memorable moments beyond the lab. The countless group parties, outings, and spontaneous gatherings added so much joy to my time here. It has been a privilege to work in such a dynamic and supportive environment, both scientifically and socially.

I also acknowledge the financial support from the University of Ottawa.

I am indebted to all members of the Structured Quantum Optics (SQO) group, past and present, whose time overlapped with mine. My Ph.D. has been a truly memorable and enjoyable experience because of all of you. I will fondly remember our moments together—the science we were part of, the trips, retreats, Christmas parties, conferences, and the frequent, ever-present coffee breaks. I really appreciate the group's eagerness to find any excuse to have fun (not that we ever needed one in the first place).

In particular, I am very grateful to Francesco Di Colandrea for the shared experiments and valuable discussions—scientific and otherwise. I appreciate your immense commitment and camaraderie, both in scientific and culinary adventures. I am also thankful to Alessio D'Errico for his friendship and scientific advice. I appreciate your levelheadedness and calm. I am equally grateful to Yingwen for his help and guidance during experiments; I learned a lot from all of you.

For their friendship and good memories, I am grateful to Francesco, Alessio, Tareq, Lukas, Felix, Nazanin, and Tugrul. I truly appreciate the time we spent together—whether attending conferences in different corners of the world or simply hanging out and having fun in Ottawa. My time in the group and in Ottawa was memorable because of all of you. I feel privileged to have shared part of this journey together.

I would also like to acknowledge Tanya Sohrabi for her contagious enthusiasm and eagerness for science. I am likewise grateful to Yishai, Farid, Qasem, Blondie, Kevin, Rojan, James, Christian, Ashlin, John, Alicia, Manuel, Xiaoqin, and Reza (in no particular order). I appreciate our conversations, and it has been a pleasure sharing my time in the group with all of you.

I would like to thank Jordan and Tara for their assistance with all things administrative. I also acknowledge Vahid Salari, Florence Grenapin, and all my co-authors—without you, the work in this thesis would not have been possible.

I am also thankful for my friends in the Advanced Research Complex (ARC), in particular Jean Luc, for the beer outings, fun discussions, and good banter. I also appreciate Amit for his friendship and the time we shared during our studies in Ottawa. I am deeply indebted to my friends from Nepal, Bishal I and Bishal II, for their friendship and support.

Most importantly, I would like to thank my parents and my sister back in Nepal, whose constant and unconditional support—despite the geographical distance—has continued to push me forward. This Ph.D. journey is theirs as well.

Dedication

This thesis is dedicated to my mom, my dad and my sister.

Statement of originality and collaborative contributions

To the best of his knowledge, the author states that the work described in this PhD thesis constitutes original research in the field of physics.

E. Karimi initiated the work of Chapter 2 on Biphoton Spatial Mode Demultiplexing. D. Paneru, F. Grenapin and E. Karimi performed the theory. D. Paneru, F. Grenapin, and A. D'errico performed the experiment. F. Grenapin prepared the initial draft, and all the authors were involved in writing the final manuscript.

D. Paneru conceived of the work of Chapter 2 on displacement sensing with Higher Order Hermite Gauss modes and developed the theory. D. Paneru conducted the experiment with the supervision of E. Karimi and A. D'errico. D. Paneru prepared the initial draft, and all authors contributed to the final manuscript.

D. Paneru and F. D. Colandrea conceived the idea for the work in Chapter 3 on the high-dimensional non-local unitary transfer. D. Paneru developed the theory for general unitary operators. F. D. Colandrea developed the theory adapted to translation-invariant operators and designed the holograms. D. Paneru and F. D. Colandrea performed the experiment and data analysis. D. Paneru and F. D. Colandrea prepared the first draft of the manuscript. A. D'Errico, and E. Karimi supervised the project. All authors discussed the results and contributed to the final version of the manuscript.

E. Karimi and Y. Zhang conceived of the project on structured Hong Ou Mandel in Chapter 3. D. Paneru, Y. Zhang, and F. D. Colandrea did the theory and simulations. X. Gao, Y. Zhang, D. Paneru, and F. D. Colandrea, performed the experiment. X. Gao drafted the initial manuscript and all the authors were involved in the final manuscript.

F. D. Colandrea conceived the idea and developed the theory for the work in chapter 3 on Engineering single qubit noises, with contributions from A. D'Errico. and M. Arienzo. F. D. Colandrea, T. Jaouni, and J. Grace fabricated the metasurfaces. F. D. Colandrea, J. Grace, and D. Paneru performed the experiment. F. D. Colandrea, T. Jaouni, and J.Grace analyzed the data. F.D. Colandrea and A. D'Errico. prepared the first version of the manuscript. A. D'Errico. and E. Karimi supervised the project.

V. Salari and E. Karimi developed the idea for the work in chapter 4 and consulted it with D.Paneru, S. Barzanjeh., M. Rezaee, and E. Saglamyurek to design the protocol. V. Salari, M. Ghadimi, and M. Abdar developed the algorithm, D. Paneru performed the experiments under the supervision of E. Karimi. All authors contributed to discussions. V. Salari, D. Paneru, and E. Karimi wrote the manuscript, and V. Salari, S. Barzanjeh, and E. Karimi revised the final version. V. Salari and D. Paneru contributed equally to this work.

List of Publications

Ph.D.

1. **Paneru, Dilip**, Alessio D'Errico, and Ebrahim Karimi. "Transverse distance estimation with higher-order Hermite-Gauss modes." *Physical Review A* 113.1 (2026): L011702.

2. Di Colandrea, F., Jaouni, T., Grace, J., **Paneru, D.**, Arienzo, M., D'Errico, A., & Karimi, E., "Engineering qubit dynamics in open systems with photonic synthetic lattices" *Physical Review Research* **7**, 023236 (2025).

3. **Paneru, D.**, Di Colandrea, F., D'Errico, A., & Karimi, E., "Nonlocal transfer of high-dimensional unitary operations", *Quantum* **9**, 1855 (2025).

4. Gao, X., **Paneru, D.**, Di Colandrea, F., Zhang, Y., & Karimi, E., "Generation of the Complete Bell Basis via Hong-Ou-Mandel Interference", *Physical Review A* **112**, 012215 (2025).

5. Salari, V., **Paneru, D**., Saglamyurek, E., Ghadimi, M., Abdar, M., Rezaee, M., Aslani, M., Barzanjeh, S., & Karimi E., "Quantum face recognition protocol with ghost imaging." *Scientific Reports* **13**, 2401 (2023). (**joint first author**)

6. Grenapin, F., **Paneru, D.**, D'Errico, A., Grillo, V., Leuchs, G., & Karimi, E., "Superresolution enhancement in biphoton spatial-mode demultiplexing", *Physical Review Applied* **20**, 024077 (2023).

M.Sc.

1. Paneru, D., Te'eni, A., Peled, B. Y., Hubble, J., Zhang, Y., Carmi, A. & Karimi, E. (2020), "Experimental tests of Multiplicative Bell Inequalities", *Physical Review Research*, **3**, L012025 (2021).

2. Paneru, D., Cohen, E., Fickler, R., Boyd, R. W. & Karimi, E., "Entanglement: quantum or classical?", *Reports on Progress in Physics*, **83**(6), 064001, (2020).

3. Paneru D. & Cohen E.," Past of a particle in an entangled state", *International Journal of Quantum Information*, **15**(08), 1740019, (2017).

Table of Contents

List of Figures

Chapter 1

Introduction

The early twentieth century marked a significant shift in our understanding of nature with the advent of quantum mechanics – a theoretical framework developed to address the inadequacies of classical physics. Confronted with enigmatic phenomena such as blackbody radiation, the photoelectric effect, discrete atomic spectra, and Compton scattering, the classical worldview was unraveling, giving way to a deeper, more mysterious picture. The quantization of energy by Planck [1], whereby energy is absorbed or emitted in discrete packets called "quanta"; Einstein's explanation of the photoelectric effect [2], which proposed that light is emitted as a stream of particles or "photons"; and Bohr's atomic model [3], which accounted for the discrete hydrogen spectra—together constituted the bedrock of this development. These ideas were later developed by Schrödinger and Heisenberg, with their wave and matrix formulations of quantum mechanics [4, 5], and eventually unified under Dirac's formalism, giving form to the quantum theory as we know it today.

Conceptually, the core ideas emerging out of the quantum formalism—such as superposition, where a particle can "be present" in multiple paths, leading to wave-like behavior; the idea of uncertainty in complementary measurements, captured by the Heisenberg uncertainty principle; or entanglement, where two or more particles are non-locally correlated with each other—presented stark contrasts to the classical way of thinking about the universe. This even led Einstein and others to question the reality or the completeness of quantum theory in their seminal paper [6], and these non-intuitive ideas continue to influence the current understanding of quantum mechanics and drive current technological innovations.

While early quantum mechanics focused on single-particle systems and their deterministic wavefunctions, it became clear by mid-century that a field-theoretic description was necessary for describing indistinguishable particles and multi-particle states. This need led to the development of second quantization—a formalism in which fields are quantized.

In this framework, creation and annihilation operators act on Fock states, allowing for a unified description of bosons and fermions and facilitating the treatment of quantum optical systems. Quantum electrodynamics (QED), as developed by Feynman, Schwinger, and Tomonaga, demonstrated the power of this approach [7, 8, 9], successfully accounting for radiative corrections and vacuum fluctuations. This second-quantized perspective would later underpin the formal machinery of quantum optics.

The second half of the twentieth century also saw another remarkable technological achievement that fueled the development of quantum optics, the building of the LASER. Following up on the proposal by Schawlow and Townes to implement the optical analogue of the microwave laser (MASER), first built in 1953, Theodore Maiman demonstrated the working of the first LASER in 1960 [10] at Hughes Research Laboratories. Lasers allowed one to generate a very narrow and intense beam of light at very sharp wavelengths, and soon they were almost ubiquitous, from being commonplace in physics laboratories to being used in personal computers, communication systems, cash registers, manufacturing, and surgery. Although the science of lasers predated the invention of the laser itself, the rapidly advancing field needed solid theoretical foundations. Soon, in the 1950s and 1960s, after a collection of works by Klauder, Sudarshan, and Glauber, the quantization principles were applied to the electromagnetic field, and also the concept of "coherent state" [11, 12] was developed. These developments made it evident that classical electromagnetic theory was inadequate to explain some properties of light, particularly those related to the statistics of photons. Soon Clauser demonstrated the detection of heralded single photons via an atomic cascade in mercury, [13], and Kimble et al. demonstrated the signature anti-bunching characteristic of the single photon sources, demonstrating sub-Poissonian statistics [14]. This was quickly followed by observation of an even more "quantum" effect of the two-photon interference at the beam splitter, called the Hong-Ou-Mandel effect [15].

The generation of squeezed states [16, 17, 18] of light, where one of the quadratures can have uncertainty below that of the vacuum noise, marked a promising application of quantum optics in sensing and metrology. Several works have shown that using entanglement and squeezing can overcome classical sensitivity bounds, such as the standard quantum limit (SQL), which scales as the number of particles $1/\sqrt{N}$. For instance, a new class of interferometry based on four-wave mixing or parametric amplification can be shown to achieve a sensitivity of $1/N$, or the Heisenberg limit [19]. Large-photon-number path entangled states also known as N00N [20] are also used to achieve a similar phase sensitivity. Entanglement between photon pairs in the spatial domain has also been utilized in quantum imaging. In particular, ghost imaging and quantum illumination protocols demonstrate how non-classical light can be used to image or detect objects in noisy environments with greater sensitivity and noise tolerance than classical illumination [21, 22].

Ghost imaging, for instance, uses entangled photon pairs to reconstruct an image using correlations, despite one of the photons never interacting with the object, which reduces the probe illumination, thereby making it an attractive candidate for imaging sensitive tissues. Quantum illumination enhances target detection in noisy environments by exploiting entangled probe-idler pairs, even when entanglement is destroyed by loss. Recent advancements in optical mode engineering have pushed quantum imaging toward practical superresolution. For instance, by utilizing the spatial information contained in the higher-order Hermite-Gauss modes, experiments have demonstrated resolution below the Rayleigh limit and enhanced estimation variance scaling [23, 24].

Alongside these experimental developments, a formal theory for quantum detection and estimation [25] has also been developed, where the Quantum Fisher Information (QFI) quantifies the ultimate sensitivity and bounds achievable by any unbiased estimator via the Quantum Cramér-Rao Bound. A rigorous mathematical framework for quantum metrology is provided by quantum estimation theory, where the Quantum Fisher Information (QFI) sets the ultimate bound on precision via the Quantum Cramér-Rao bound [25, 26]. Optimizing quantum states and measurements based on QFI has become a standard approach in the design of quantum sensors, including atomic clocks, interferometers, and gravimeters.

All of these developments in the study of quantum properties of light were also being paralleled by the development of quantum adaptations to information theory. Classical information theory was another hallmark development of the twentieth century. Harry Nyquist's 1924 work on telegraphy, established a quantitative relationship between bandwidth and signal transmission rate, laying early groundwork for the field [27]. In 1928, Ralph Hartley introduced a logarithmic measure of information content, now known as the Hartley measure, providing one of the first mathematical frameworks for information [28]. Claude Shannon, called the father of information theory, in his masters thesis, (perhaps the most significant masters thesis in history), proved that Boolean electrical switches could be used to perform logic functions, thus laying the foundation for the digital computer. In another groundbreaking paper, "A Mathematical Theory of Communication", he introduced the concepts of entropy, channel capacity, and coding, formally founding information theory as a scientific discipline [29]. Soon, coding theory was developed notably with the introduction of Hamming's error-correcting codes, which addressed the communication through noisy channels [30].

On the foundational side of quantum theory, following up on the EPR argument, John Bell in 1964 developed an inequality [31] that is satisfied by classical or local hidden variable theories but violated by quantum theory. Experimental demonstrations since, notably by Clauser and Freedman [32] in 1972, among many others, have confirmed quantum nonlocality, falsifying the classical description of the quantum phenomena. On the other extreme of the question of what can be achieved through quantum non-locality, people have also wondered if one can send signals faster than the speed of light. This was quickly shown to hinge on the cloneability of quantum states, which was proven to be impossible in a work by Wooters and Zurek, leading to the no-cloning theorem [33]. These works mark the start of the field of quantum information theory. Several important works followed, notably Bennett and Brassard's introduction of the BB84 protocol, which showed the use of quantum states of light to transfer information [34]. This essentially marked the beginning of the field of quantum key distribution, also known as quantum key establishment (QKD). Peter Shor's quantum prime factorization algorithm [35] showed that quantum computers can provide exponential speedup in factoring large prime numbers. Coincidentally, classical encryption schemes like the RSA algorithm base their security upon the difficulty of solving the prime factoring problem in classical computers. Thus, in addition to demonstrating that quantum computers are exponentially superior to classical computers in performing certain tasks and thereby reinvigorating research in quantum computing, this result also underscores the strong need to develop the field of quantum cryptography. Subsequently, Grover came up with a quantum algorithm for another widely used and important problem of searching through an unstructured list, which provided a polynomial speedup compared to classical algorithms.

This thesis broadly encompasses the works done in structured quantum optics, in particular, the use of structured spatial profiles of photons in quantum sensing, imaging and quantum information. Chapter 2 starts with the work done on optical displacement sensing with Higher-Order Hermite-Gauss modes, where we derive the Fisher information for projective measurements and show sensitivity enhancement proportional to the mode order, essentially proving that higher-order modes are better suited for measuring small optical separations. To provide the background and set the stage for the work, we also briefly introduce the idea of spatial modes and discuss their generation and detection in the laboratory. In the second part of the chapter, we present the theory and experimental results on displacement sensing using spatially correlated photon pairs and show the enhancement in sensitivity obtained through the high-dimensional correlations. Chapter 3 is concerned with the experiments conducted on quantum information. First work is on the transfer of high-dimensional unitary operators in a distributed quantum network between parties using a spatially correlated bi-photon state. The second work focuses on the structured Hong-Ou-Mandel experiment, where the distribution of the Bell states at the output of a Hong-Ou-Mandel beam splitter is tailored using q-plates. Lastly, we also present a work on the simulation of several single-qubit noises using liquid crystal devices by coupling the spatial and polarization degrees of freedom of light. Chapter 4 presents the work on quantum imaging combined with the postprocessing of quantum images with a novel quantum algorithm on pattern recognition. We introduce the concepts of quantum imaging, particularly that of ghost imaging, as background for the article. Note that due to overlap, sometimes significant, between the works, the organization into three main chapters is for structural purposes rather than a literal classification.

Chapter 2

Spatial modes in Displacement Sensing

This chapter is based on the following articles:

1. **Paneru, Dilip**, Alessio D'Errico, and Ebrahim Karimi. "Transverse distance estimation with higher-order Hermite-Gauss modes." *Physical Review A* 113.1 (2026): L011702.

   DOI: https://doi.org/10.1103/h91l-w8w7

2. Grenapin, F., **Paneru, D.**, D'Errico, A., Grillo, V., Leuchs, G., & Karimi, E. (2023). Superresolution enhancement in biphoton spatial-mode demultiplexing. *Physical Review Applied, 20(2)*, 024077.

   DOI: https://doi.org/10.1103/PhysRevApplied.20.024077

2.1 Spatial Modes of Light

Maxwell's equations govern the propagation of electric and magnetic fields in vacuum or through any medium. Maxwell's equations in vacuum are,

$$\nabla \cdot \mathbf{E} = 0, \qquad \nabla \cdot \mathbf{B} = 0, \tag{2.1}$$

$$\nabla \times \mathbf{E} = -\frac{\partial \mathbf{B}}{\partial t}, \qquad \nabla \times \mathbf{B} = \mu_0 \varepsilon_0 \frac{\partial \mathbf{E}}{\partial t}. \tag{2.2}$$

These four equations also lead to the wave equation satisfied by both the electric ($\mathbf{E}$) and the magnetic field ($\mathbf{B}$),

$$\left(\nabla^2 - \frac{1}{c^2}\frac{\partial^2}{\partial t^2}\right)\mathbf{f}(\mathbf{r}, t) = 0, \tag{2.3}$$

where $\mathbf{f}(\mathbf{r}, t)$ is a vector field that represents either $\mathbf{E}$ or $\mathbf{B}$. Any such solution to Maxwell's equations and the wave equation can be considered a mode of light. A mode defined by the vector field $\mathbf{f}(\mathbf{r}, t)$, should also satisfy the normalization condition,

$$\frac{1}{V}\int_{\mathbf{r}} |\mathbf{f}(\mathrm{r}, t)|^2 d\mathbf{r} = 1, \tag{2.4}$$

where the integral is carried out over a volume V containing the system under consideration. Depending upon the degree of the freedom of light, there are different families of modes in space, polarization, time, frequency, etc. It is always helpful to define an orthonormal and complete basis of modes onto which any arbitrary electromagnetic field can be decomposed. For instance, for polarization, the set of horizontal and vertical polarization, $|H\rangle, |V\rangle$, consists of an orthonormal and complete set. Spatial modes of light refer to the modes that are structured in space, i.e in either the transverse or the longitudinal degree of freedom. These transverse modes are solutions to the Helmholtz equation under the paraxial approximation, where the field envelope varies slowly in the longitudinal direction. The most common examples/solutions in Cartesian coordinates are described by Hermite-Gaussian functions, while in cylindrical coordinates they are described by the Laguerre-Gaussian modes [36, 37]. For instance, the transverse profile of the Hermite Gauss (HG) modes is given by:

$$\psi_{nm}(x, y, z) = \frac{A}{w(z)} H_m\left(\frac{\sqrt{2}x}{w(z)}\right) H_n\left(\frac{\sqrt{2}y}{w(z)}\right) \exp\left(-\frac{x^2+y^2}{w^2(z)}\right) \tag{2.5}$$

$$\exp\left(-ikz - i(m+n+1)\zeta(z) + i\frac{k(x^2+y^2)}{2R(z)}\right). \tag{2.6}$$

where m, n are the mode indices along x, and y respectively, $H_{m/n}(.)$ is the m/nth Hermite polynomial, $w(z) = w_0\sqrt{1+(z/z_R)^2}$ is the beam waist, and w_0 is the beam waist at $z = 0$,

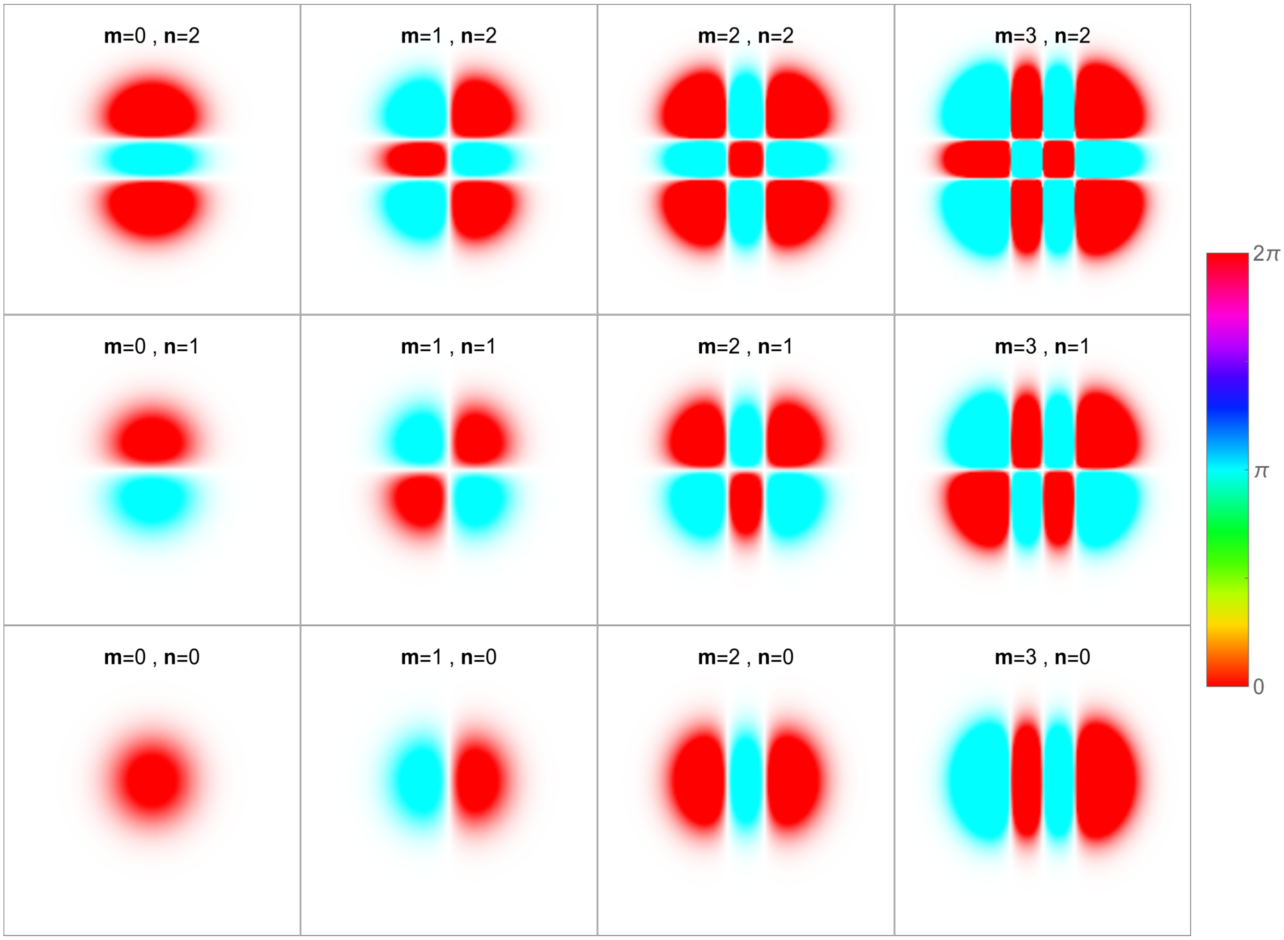

Figure 2.1: **Hermite Gauss Modes.** Phase profiles modulated by the corresponding intensity profiles of a few HG modes with the indices $m \in \{0, 1, 2, 3\}$, and $n \in \{0, 1, 2\}$.

$z_R = \frac{\pi w_0^2}{\lambda}$ is the Rayleigh's range, $R(z) = z(1 + (z_R/z)^2$ is the radius of the curvature of the wavefront, and $\zeta(z) = (m + n + 1)\arctan(z/z_R)$ is the Guoy phase. These modes form a complete, orthonormal basis set for paraxial beams in free space or within stable optical cavities. The phase profiles modulated by the intensity for these modes are plotted in Figure 2.1.

2.1.1 Creation of Spatial Modes

In optical systems, spatial modes refer to the transverse field distributions of light beams, such as Gaussian, Hermite–Gaussian, Laguerre–Gaussian, or other orthogonal basis modes that form complete sets for representing arbitrary optical fields. The creation of specific spatial modes is typically achieved using beam-shaping optics such as spatial light modulators (SLMs) [38], digital micromirror devices (DMDs), phase plates, or specially designed refractive and diffractive optical elements. For example, Laguerre–Gaussian modes carrying orbital angular momentum can be generated using q-plates [39], spiral phase plates [40], or holographic phase masks encoded on an SLM. The accurate creation and detection of spatial modes are essential for applications in optical communication, quantum information, microscopy, and precision metrology, where modal purity and crosstalk play crucial roles in performance.

2.1.2 Detection of Spatial Modes

Detection of spatial modes is vital in both classical and quantum technologies, where the spatial degrees of freedom are used for multiplexing or encoding information. It is central to applications in quantum communication, mode-division multiplexing, optical metrology, and super-resolution imaging, where distinguishing closely multiplexed entangled spatial modes is critical [41]. The detection of spatial modes in optics involves projecting an incoming optical field onto a predefined set of orthogonal spatial basis functions, such as Hermite-Gaussian (HG), Laguerre-Gaussian (LG), or any custom-designed modal sets. A common approach uses mode-selective detection via coupling into a single-mode fiber (SMF), which effectively acts as a matched filter for the fundamental Gaussian mode. By preceding the fiber with mode-transforming optics, such as spatial light modulators (SLMs), custom refractive elements, or phase masks, the incoming field can be selectively converted to the fiber's acceptance mode, enabling projective measurements onto arbitrary spatial modes with high fidelity [42, 43]. For instance, to detect the Orbital Angular momentum (OAM) carried by an incoming light beam, one can impinge the beam onto a phase profile which is conjugate to the OAM being detected, which then converts the desired OAM mode into a fundamental Gaussian whereby it can be detected by coupling into a single-mode fiber.

More advanced techniques include mode sorters that deterministically separate spatial modes into distinct output channels. For example, phase-unwrapping transformations such as log-polar coordinate mappings have been employed to convert azimuthal variations of orbital angular momentum (OAM) modes into transverse displacements, which can be separated using Fourier optics [44, 45]. Interferometric detection strategies—such as those based on Mach–Zehnder or Sagnac interferometers—allow coherent projection onto arbitrary superpositions of spatial modes, which is particularly useful for measuring quantum states [46]. In addition, digital holography and wavefront sensing combined with computational reconstruction enable real-time mode decomposition of complex beams.

In both of our works on displacement sensing with Hermite Gauss modes, we perform the mode detection using a technique called intensity-flattening [47]. In this technique, a phase hologram corresponding to the conjugate mode of the desired projection is displayed in the spatial light modulator [38], and it is coupled to a single-mode fiber after suitable demagnification. The need for demagnification can be understood as follows. Say we would like to determine the content of a transverse mode $\phi(x, y)$ in the incoming field $\psi(x, y)$. After displaying the conjugate profile, $\phi^*(x, y)$ on the SLM and coupling to the single-mode fiber, the signal intensity detected in the fiber is proportional to (in the SLM plane),

$$I = N \left| \int_x \int_y \phi^*(x, y)\psi(x, y)e^{-(x^2+y^2)/w^2} dxdy \right|^2, \tag{2.7}$$

where N is a constant proportional factor, and w is the waist of the fiber mode at the SLM plane. If the waist of the single-mode fiber, w is much larger than the extent of the individual modes considered, then it can be factored out of the integral as a constant, and the Intensity is proportional to

$$I = N' \left| \int_x \int_y \phi^*(x, y)\psi(x, y) dxdy \right|^2, \tag{2.8}$$

which is proportional to the inner product of the incoming field with the particular mode.

2.2 Quantum Metrology

Quantum metrology [48] is a rapidly advancing field where the quantum properties of a particle, such as entanglement and superposition, are used to enhance the measurement and estimation of certain quantities of interest that characterize the whole or part of a given system. In classical measurement theory, the central limit theorem dictates that the standard error of a measurement scheme is reduced by a factor of $N^{1/2}$ when repeated N times. This factor or limit is variously known as “shot noise”, or the standard quantum limit (SQL). Ideally, the goal of quantum metrology is to improve this limit using quantum properties to approach the Heisenberg-like scaling of errors as N^{-1}, dictated by the Heisenberg uncertainty relations. In general, quantum metrology encompasses any technique that uses quantum effects to enhance classical measurement techniques, be it noise suppression using correlated measurements [49, 50], or enhanced sensitivity [51, 52].

2.2.1 Quantum Parameter Estimation and Cramér Rao Bound

Quantum parameter estimation is a cornerstone of quantum metrology, focusing on the precise determination of physical parameters—such as phase shifts, frequencies, or magnetic fields—using quantum systems. Unlike classical estimation, quantum techniques leverage uniquely quantum resources such as entanglement and squeezing to achieve sensitivities beyond the classical shot-noise limit. The framework is often formalized through the quantum Cramér-Rao bound, which sets the minimum achievable variance of an estimator given the quantum Fisher information [53, 54, 55]. As a framework, quantum parameter estimation is routinely applied in high-precision spectroscopy, atomic clocks, gravitational wave detection, and in emerging quantum sensing technologies [48, 56] in general.

Recent advances in the field have expanded the theoretical and practical toolkit available for optimal estimation. Techniques such as adaptive measurements, Bayesian inference, and quantum error correction are being developed to deal with challenges posed by noise, decoherence, and resource limitations [57, 58]. There is also a growing interest in multiparameter quantum estimation, where simultaneous estimation of several parameters introduces trade-offs in sensitivity [59]. Overall, quantum parameter estimation is not only central to quantum-enhanced measurement technologies but also provides deep insights into the nature of quantum information, measurement, and control.

2.2.2 Fisher Information and the Quantum Cramér Rao bound

Fisher information describes the amount of information a measurement result can provide about the parameter, say 's', being estimated. The standard error Δs in the estimates of the measured parameter is lower bounded as,

$$\Delta s \geq \frac{1}{\sqrt{\mathcal{FI}_n(s)}}, \tag{2.9}$$

where

$$\mathcal{FI}_n(s) = \sum_n \frac{1}{P_n(s)} \left(\frac{\partial P_n(s)}{\partial s} \right)^2, \tag{2.10}$$

is the Fisher Information associated with the selected Positive Operator Valued Measure (POVM) measurement $\{\Pi_i\}$, and $\mathcal{P}_n(s) = Tr[\Pi_i \rho]$, and ρ is the density matrix of the system.

The error bound from the (2.10) gives the lower bound related to the selected POVM $\{\Pi_i\}$. The Fisher Information optimized over all possible sets of POVM measurements is also referred to as the Quantum Fisher Information [60]. The Quantum Cramér-Rao Lower Bound, which is the minimum possible standard error on the unbiased estimation of the parameter, is given by the inverse of the Quantum Fisher Information.

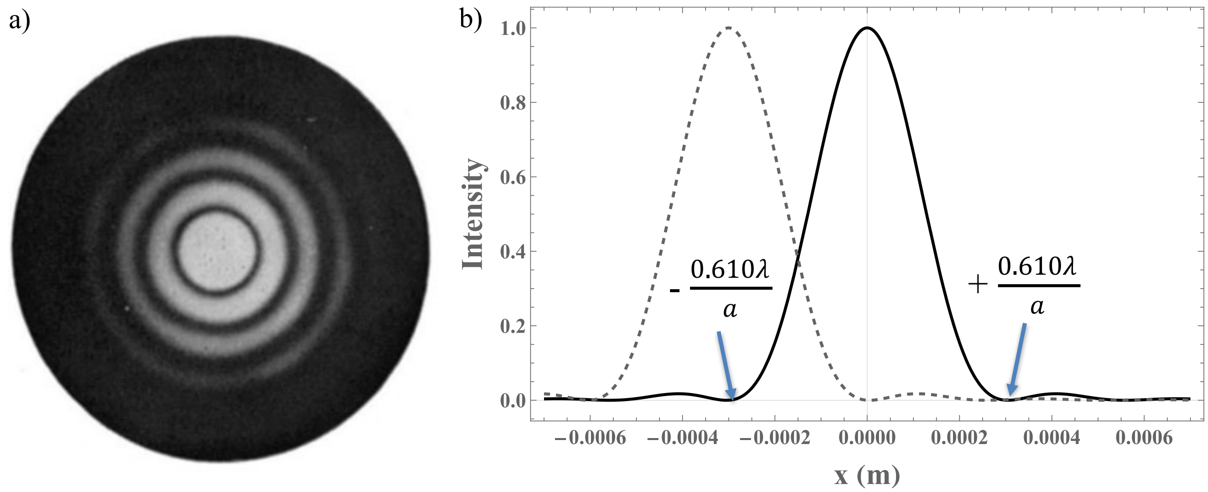

Figure 2.2: **Diffraction and resolution limits** a) Airy pattern for the diffraction of a point source passing through a circular aperture. (Image taken from Principles of Optics (7th ed.), by M. Born & E. Wolf, 1999, Cambridge University Press, p. XX. Copyright 1999 by Cambridge University Press.) b) One dimensional intensity profile (solid) showing the location of the first minimas. Intensity profile of a second point source (dashed) displaced at the location of the minima. a: radius of the aperture.

2.3 Optical Resolution limits

In optics, the resolution limit of any imaging system is fundamentally constrained by diffraction, which causes light to spread when passing through an aperture.

Fundamentally, this effect limits the ability of the imaging system to distinguish two closely spaced objects. For instance, the diffraction of a point source from a circular aperture results in an intensity distribution (also known as Airy distribution) with alternating rings of maxima and minima, (shown in Figure 2.2. a)). Qualitatively, two point sources are just resolvable when the principal maximum of one diffraction pattern coincides with the first minimum of the other (see Figure 2.2 b)).

Mathematically, the minimum resolvable angle θ_{min} is given by,

$$\theta_{\text{min}} = 0.61\frac{\lambda}{a},$$

where λ is the wavelength of light and a is the radius of the aperture. This leads to a spatial resolution limit in imaging systems also referred to as the Rayleigh's criterion [61],

$$\Delta x \approx 0.61\frac{\lambda}{\text{N.A.}},$$

where N.A. is the numerical aperture. Rayleigh's criterion, while not a strict boundary, provides a practical threshold for resolution, especially in incoherent imaging. Overcoming this limit requires advanced techniques such as near-field scanning [62], structured illumination [63], or fluorescence microscopy [64].

2.4 Spatial Mode Demultiplexing (SPADE)

Spatial mode de-multiplexing (SPADE) is an optical measurement technique designed to estimate the separation between closely spaced incoherent point sources by examining the mode content of the electromagnetic field after the apertures. It was first proposed by Tsang and colleagues in 2016 [23], how one can circumvent the so-called Rayleigh's limit by sorting into modes tailored to the point spread function (PSF) of the imaging system. From a fisher information perspective, the inability to resolve the point sources below the Rayleigh's limit can be understood from the fact that the fisher information in intensity measurements vanishes as the separation approaches zero (also referred to as Rayleigh's curse [65]). Instead of detecting light intensity in the image plane, SPADE projects the collected optical field onto a set of orthogonal spatial modes—such as Hermite-Gaussian modes—using mode-selective optics and photon-counting detectors. The method leverages the fact that the separation information resides in higher-order modes, which are typically inaccessible to standard image-plane detection. Experimental implementations of SPADE are often sensitive to optical misalignment, modal crosstalk and noise. Nevertheless, several experiments such as Tang et al. [66] and Tham et al. [65] have demonstrated spatial mode sorting and separation estimation with precision beyond the classical Rayleigh limit, highlighting SPADE's potential for applications in superresolution microscopy, astronomical imaging, and quantum metrology. Recent practical demonstration [67] has also achieved a sensitivity of five orders of magnitude below the Rayleigh limit (~ 20 nm).

2.5 Spontaneous parametric down conversion (SPDC)

Spontaneous parametric down-conversion is an optical process in which a pump photon, interacting with a nonlinear crystal, is converted into a pair of lower-energy photons, typically referred to as the signal and idler photons. The quantum state of these photon pairs is intrinsically entangled in multiple degrees of freedom, including polarization, frequency, and notably, the transverse spatial domain. The strong correlations between the down-converted photons arise due to the conservation of transverse momentum and energy, which are imposed by the phase-matching conditions within the nonlinear crystal [68, 69]. In particular, the conservation principles imply that the wave vectors obey,

$$\mathbf{k_s} + \mathbf{k_i} = \mathbf{k_p}, \tag{2.11}$$

where $\mathbf{k_s}$, $\mathbf{k_i}$, and $\mathbf{k_p}$ are signal, idler and pump wave vectors respectively and

$$\omega_p = \omega_s + \omega_i, \tag{2.12}$$

where ω_p, ω_s, and ω_i, are pump, signal and idler wavelengths. SPDC has been widely used as a primary source of heralded single photon pairs in quantum cryptography, quantum metrology, quantum imaging, experimental Bell tests, and quantum communication, among other applications. Depending upon the polarisation of the pump and the signal/idler photons obtained, the SPDC process can be classified into three different types: Type 0 (Signal, idler and the pump photons have the same polarisation), Type I (signal and idler polarisation is orthogonal to that of the pump photon), and Type II (The polarisation of the signal and idler are orthogonal to each other). The spatial correlations inherent in SPDC can be probed and engineered through various configurations of the pump beam, crystal properties, and collection optics, making spatial entanglement a rich resource for quantum imaging, high-dimensional quantum information protocols, and quantum metrology. The quantum state of the photon pair produced via SPDC can be written as

$$|\psi\rangle = |vac\rangle + \int d\mathbf{k}_s d\mathbf{k}_i \psi(\mathbf{k_s}, \mathbf{k_i}) |\mathbf{k}_s\rangle |\mathbf{k}_i\rangle . \tag{2.13}$$

Assuming that the pump photon propagates along the z axis, and that the dimension of the crystal in x and y direction is very large compared to the pump profile, the bi-photon amplitude can be written as [69],

$$\Psi(\vec{q}_s, \vec{q}_i) = \mathcal{N} e^{-\omega_p^2/4|\mathbf{q}_s + \mathbf{q}_i|^2} \mathrm{sinc}(L\Delta k_z/2), \tag{2.14}$$

where $\mathrm{sinc}(x) = sin(x)/x$ is the sinc function, $\mathbf{q}_s$ and $\mathbf{q}_i$ are the transverse momentum vectors (or spatial frequency coordinates) of the signal and idler photons, where L is the length of the crystal, w_p is the width of the gaussian pump, and Δk_z is the longitudinal wave vector mismatch.

2.5.1 Schmidt Decomposition of SPDC

To quantitatively characterize spatial entanglement, one can perform a Schmidt decomposition of the biphoton wavefunction into orthonormal spatial mode pairs [70]. In Schmidt decomposition, the bipartite wave function can be written as $\Psi(\mathbf{q}_s, \mathbf{q}_i) = \sum_j \sqrt{\lambda_j} u_j(\mathbf{q_s}) v_j(\mathbf{q_i}))$, where $u_j(\mathbf{q_s})$, $v_j(\mathbf{q_i})$ are the Schmidt modes with λ_j the corresponding eigenvalue. The Schmidt number $K = 1/\sum_j \lambda_j^2$ quantifies the effective number of spatial modes and thus the degree of entanglement [70, 71]. To perform the Schmidt decomposition, it is helpful to approximate the phase-matching term as follows. First we use the paraxial approximation and write $\Delta k_z \approx |\mathbf{q}_s - \mathbf{q}_i|^2$, and then replace the sinc function by a Gaussian function.

$$\mathrm{sinc}(L\Delta k_z/2) \approx \mathrm{sinc}(b^2|\mathbf{q}_s - \mathbf{q}_i|^2) \approx e^{-b^2|\mathbf{q}_s-\mathbf{q}_i|^2}, \tag{2.15}$$

where $b^2 = L/4k_p$ and k_p is the momentum of the pump. The approximated biphoton wavefunction is then [70],

$$\Psi(\vec{q}_s, \vec{q}_i) = \mathcal{N} e^{-|\mathbf{q}_s+\mathbf{q}_i|^2/\sigma^2} e^{-b^2|\mathbf{q}_s-\mathbf{q}_i|^2}, \tag{2.16}$$

where $\sigma = 2/\omega_p$. In this form, the Schmidt eigenmodes are equivalent to the energy eigenfunctions of a two-dimensional isotropic harmonic oscillator, which implies that one can find expansions in terms of Hermite-Gauss or Laguerre-Gauss modes, with a properly chosen waist. The Schmidt rank of such a decomposition is given by $K = \frac{1}{4}(b\sigma + \frac{1}{b\sigma})^2$.

When the decomposition is performed in the Hermite–Gaussian (HG) mode basis[72, 73]—well-suited for Cartesian geometries—the wavefunction takes the form

$$\Psi(\vec{\rho}_s, \vec{\rho}_i) = \sum_{n,m} \sqrt{\lambda_{nm}}\, \phi_{nm}(\vec{\rho}_s)\phi_{nm}(\vec{\rho}_i),$$

where λ_{nm} are the Schmidt coefficients, and ϕ_{nm} are HG modes of order n, m, with the individual eigenvalues given by,

$$\lambda_{mn} = \frac{4b\sigma}{1 + b\sigma^2} \left|\frac{b\sigma - 1}{b\sigma + 1}\right|^{m+n}. \tag{2.17}$$

The set of particular HG modes that form the basis of the Schmidt decomposition are defined by the waist (τ) of the fundamental gaussian, where $\tau = 2\sqrt{\frac{b}{\sigma}}$. This is also referred as the Schmidt waist [72].

2.6 Research Summary

In the rest of the chapter, we present two research works conducted on displacement sensing. In the first, we investigate the use of higher-order Hermite-Gauss modes for sensing optically induced transverse displacements [74], and show that projective measurements onto adjacent spatial modes provide optimal Fisher information, scaling linearly with the mode order m. This performance advantage persists at larger displacements, where general expressions confirm that higher-order modes continue to outperform the fundamental Gaussian mode. Our approach enables enhanced displacement sensitivity with only a couple projective measurements, offering a scalable alternative to conventional SPADE. A proof-of-principle experiment using spatial light modulators is also conducted, showing enhanced sensitivity. In the second article [75], we use the Schmidt decomposition of the SPDC and show that the enhancement of the sensitivity in displacement measurements is proportional to the Schmidt rank K of the system. We also perform a proof-of-concept experiment with down-converted photon pairs, obtaining results that are aligned with the theory.

Transverse Distance Estimation with Higher-Order Hermite-Gauss modes

Dilip Paneru,[1,*] Alessio D'Errico,[1,2] and Ebrahim Karimi[1,2,3]

[1] *Nexus for Quantum Technologies, University of Ottawa, Ottawa ON, Canada, K1N 5N6*
[2] *National Research Council of Canada, 100 Sussex Drive, Ottawa ON, Canada, K1A 0R6*
[3] *Institute for Quantum Studies, Chapman University, Orange, California 92866, USA*

(Dated: June 4, 2025)

We explore the use of higher-order Hermite-Gauss modes for sensing optically induced transverse displacements. In the small-displacement regime, we show that projective measurements onto the two neighboring spatial modes yield optimal Fisher information, linearly scaling with the mode order m. We further extend the analysis to arbitrary displacement values and derive general expressions for the Fisher information, demonstrating that higher-order modes continue to outperform the fundamental Gaussian mode even at larger separations. This approach enables enhanced displacement sensitivity with only a minimal number of measurements, offering a simple and scalable alternative to conventional Spatial Mode Demultiplexing schemes. We provide a proof-of-principle experimental demonstration using spatial light modulators, showing an order-of-magnitude reduction in estimation variance when employing Hermite-Gauss modes of order $m = 8$ and $m = 17$. These results highlight the potential of structured light for ultrasensitive displacement sensing and may enable new applications in birefringence measurements with broadband or low-coherence light sources.

Keywords: Hermite-Gauss, Superresolution, SPADE, parameter estimation

Estimating transverse displacements is an essential task in numerous technological applications. In traditional imaging systems, resolution is linked to the precision with which one can determine the separation between two-point sources. This precision, in turn, is fundamentally limited by diffraction effects governed by the wavelength of light and the aperture size of the optical system [1]. Conventional intensity-based measurements suffer from vanishing Fisher information as the displacement between sources approaches zero, effectively linking Rayleigh's curse to an intrinsic loss of information. The recognition of this resolution limit has driven research into alternative imaging techniques that surpass the optical Rayleigh limit, including near-field imaging [2, 3] and electron-based methods, such as scanning and transmission electron microscopy [4, 5]. There is also growing interest in monitoring small transverse displacements. Approaches based either on incoherent methods, such as the Moiré effect [6], or coherent ones, such as linear photonic gears [7–9] or super-oscillations [10, 11], have been demonstrated. An alternative measurement scheme based on spatial mode demultiplexing (SPADE) was first proposed in ref. [12]. In contrast with direct imaging, SPADE utilizes projection on spatial modes tailored to the Point Spread Function (PSF) of the optical system, enabling the extraction of maximal Fisher information regardless of separation distance. This conceptual breakthrough has since inspired extensive theoretical and experimental developments, leading to adaptations of SPADE for various imaging systems [13–16], coherent sources [17–19], and studies on noise-related limitations [20, 21]. Furthermore, SPADE has been extended to multi-parameter and higher-dimensional estimation problems [22, 23], with 2D imaging simulations [24] and experimental reconstructions–leveraging techniques such as deconvolution and machine learning [25] –demonstrating resolution improvements beyond the Rayleigh limit. These findings reinforce the connection between two-point source distinguishability and overall 2D imaging resolution.

Here, we examine the problem of transverse distance estimation within the framework shown in Fig. 1, considering a probe field whose spatial profile can be tailored as desired. Specifically, we aim to detect the transverse displacement caused by anomalous refraction through a birefringent material, where the displacement is directly proportional to the material's thickness t. We theoretically calculate the Fisher information associated with this separation when the probe fields are the Higher-Order Hermite-Gauss modes. We find that the optimal mode projections for finding the separation consist of two nearest-neighboring modes of the input probe mode. Fisher information is evaluated in both the small- and large-separation regimes. In the small-separation regime, we find that the Fisher information scales linearly with the input mode number m, as expressed in Eq. 5, thereby showing that higher-order modes are significantly sensitive to distance estimation. We also address the situation where one is experimentally limited by the numerical aperture of the optics involved, and show that even in such cases, the factor of $\sqrt{m}$ enhancement persists. These findings suggest a promising method toward ultrasensitive parameter es-

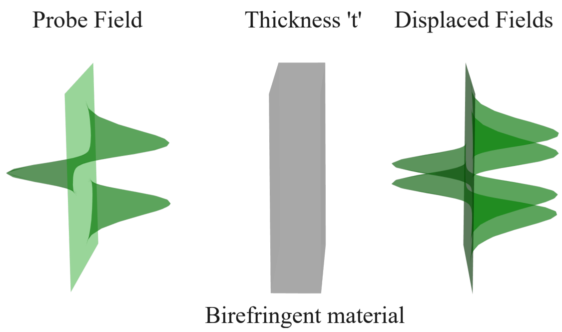

Figure 1. **Conceptual Illustration.** A schematic demonstrating how higher-order Hermite–Gauss modes can enhance sensitivity in transverse displacement estimation. Unpolarized light, prepared in a specific spatial mode (here, Hermite–Gauss mode with order $m = 2$, $n = 0$), is incident on a birefringent material. Due to the difference in refractive indices along the fast and slow axes, the beam experiences a transverse shift proportional to the material's thickness t. As shown in the manuscript, using a higher-order input mode and projecting onto the two adjacent Hermite–Gauss modes yields a sensitivity enhancement that scales with the mode order.

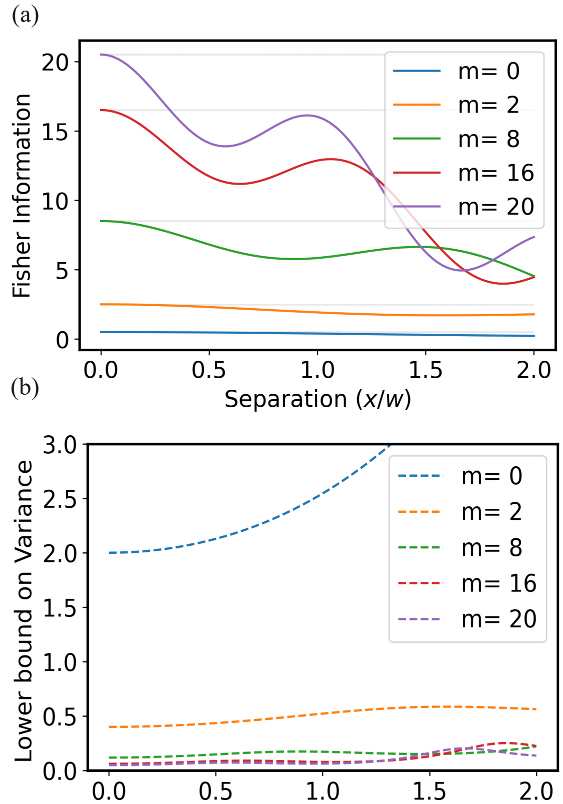

Figure 2. **Total Fisher Information and Cramér–Rao Bounds.** (a) Total Fisher information obtained from projections onto modes $m-1$, m, and $m+1$, for an input field prepared in the m-th Hermite-Gauss mode. The thin gray line represents the total Fisher information obtainable from projections onto all modes for the same input, which asymptotically approaches $m+1/2$, as discussed in the main text. (b) The corresponding Cramér–Rao bound for displacement estimates based on measurements in modes $m-1$, m, and $m+1$.

timation using structured light. We further support our theoretical analysis with a proof-of-concept experiment, which demonstrates an order-of-magnitude improvement in sensitivity compared to measurements using the fundamental mode.

In what follows, we formulate the problem in more precise terms. Suppose that we send an unpolarized incoherent Hermite-Gauss beam of order m through a birefringent material. The material induces a transverse displacement between the two orthogonal polarization components aligned with its fast and slow axes. Our goal is to estimate the transverse displacement parameter 's', which is proportional to the thickness 't' of the birefringent sample. It is well established that, under direct intensity measurements, the Fisher information vanishes as $s \to 0$ [26], a manifestation of Rayleigh's curse in displacement sensing.

The output beams, displaced by the birefringence, emerge in the following states:

$$\begin{aligned} \left|\Psi^{+}\right\rangle &= |\Psi(x+s/2)\rangle = |\mathcal{HG}_m(x+s/2)\rangle\,, \\ \left|\Psi^{-}\right\rangle &= |\Psi(x-s/2)\rangle = |\mathcal{HG}_m(x-s/2)\rangle\,, \end{aligned} \tag{1}$$

where $\langle x|\mathcal{HG}_m(x)\rangle = \frac{1}{\sqrt{2^m m! \sqrt{\pi}}}\mathcal{H}_m(\sqrt{2}x)e^{-\frac{x^2}{2}}$, is the m-th order Hermite-Gauss mode with an unit waist. The net separation between the two states is the parameter to estimate 's'. For our calculations, we assume that the parameter 's' is normalized with respect to the waist.

The overall state $\hat{\rho}_s$, which is an incoherent mixture of a positively and a negatively displaced state about the origin, can be written as

$$\hat{\rho}_s = \frac{1}{2}\left[\left|\Psi^{+}\right\rangle\left\langle\Psi^{+}\right| + \left|\Psi^{-}\right\rangle\left\langle\Psi^{-}\right|\right]. \tag{2}$$

For small separations, one can expand the displaced wavefunctions Ψ^{+} and Ψ^{-} in terms of a Taylor series with higher-order derivatives as

$$\begin{aligned} \langle x|\Psi(x \pm s/2)\rangle &\approx \langle x|\Psi\rangle \pm \frac{s}{2}\langle x|\Psi\rangle' + O(s^2) \\ &\approx \langle x|\mathcal{HG}_m\rangle \pm \frac{s}{2}\langle x|\mathcal{HG}_m(x)\rangle'\,. \end{aligned} \tag{3}$$

Here, $'$ denotes derivative with respect to x, i.e., $\partial/\partial x$, and all terms beyond the first-order in s are neglected.

The resulting expression can be further simplified using the recurrence relation for Hermite–Gauss modes:

$$\frac{\partial}{\partial x}\left|\mathcal{HG}_m\right\rangle = \sqrt{\frac{m}{2}}\left|\mathcal{HG}_{m-1}\right\rangle - \sqrt{\frac{m+1}{2}}\left|\mathcal{HG}_{m+1}\right\rangle.$$

Both $\Psi^{\pm}$ are related to the adjacent Hermite-Gauss modes of $m-1$ and $m+1$. Hence if we perform projective measurement onto the modes, $|m+1\rangle = |\mathcal{HG}_{m+1}(x)\rangle$, and $|m-1\rangle = |\mathcal{HG}_{m-1}(x)\rangle$ for the state in Equation (2) the detection probabilities are given by,

$$P_{m\pm 1} \;=\; \frac{1}{2}\left|\left\langle m\pm 1\middle|\Psi^{+}\right\rangle\right|^2 + \frac{1}{2}\left|\left\langle m\pm 1\middle|\Psi^{-}\right\rangle\right|^2.$$

Using the orthonormality of Hermite-Gauss expansion and the explicit form for the derivative, one can show that,

$$P_{m+1} = \frac{s^2}{8}(m+1), \quad \text{and} \quad P_{m-1} = \frac{s^2}{8}m. \tag{4}$$

The total Fisher information per photon in this set of measurements is given by,

$$\begin{aligned}\mathcal{FI} \;&=\; \frac{1}{P_{m+1}}\left(\frac{\partial P_{m+1}}{\partial s}\right)^2 + \frac{1}{P_{m-1}}\left(\frac{\partial P_{m-1}}{\partial s}\right)^2 \\ &=\; \frac{m+1}{2} + \frac{m}{2} \\ &=\; m + \frac{1}{2}.\end{aligned} \tag{5}$$

We observe that the Fisher information is nonzero and scales linearly with the mode number m, with the enhancement achieved through only two measurements. This scaling in Fisher information, and consequently in sensitivity, is significantly more accessible in practice compared to schemes based on multi-photon N00N states, which become experimentally challenging to implement for photon numbers $N > 2$.

The corresponding standard error in the estimates scales as,

$$(\Delta\sigma)^2 \geq \frac{1}{\mathcal{FI}} \geq \frac{1}{m+1/2}. \tag{6}$$

A further extension of the analysis to arbitrary separations, along with the derivation of a general expression for the Fisher information associated with the two-mode projections, is provided in Appendix A. The variances associated with different measurement schemes using various Hermite–Gauss modes, along with the corresponding Fisher information, are shown in Figure 2. Moreover, we consider the case where the induced displacements are coherent, with a known degree of coherence. We observe a similar scaling of Fisher information with the mode number, and note that the maximum Fisher information approaches that of the incoherent case when the two displacements are out of phase – See Appendix B for details of the calculations.

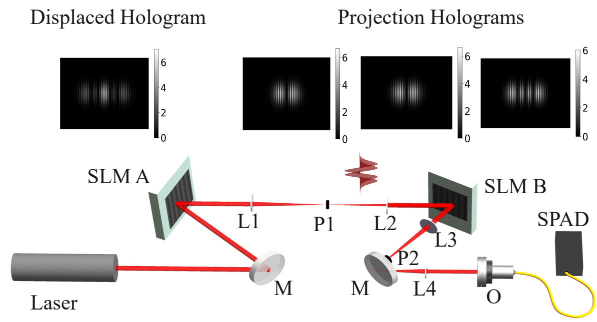

Figure 3. **Schematic of the Experimental Setup.** A suitably attenuated Gaussian beam is directed onto Spatial Light Modulator A (SLM A), which generates a superposition of two displaced Hermite-Gauss modes of the desired order by displaying a custom-designed hologram. A second modulator, SLM B, together with a demagnification imaging system, performs the required mode projections. Optical components are labeled as follows: M - Mirror; L1–L4 - Lenses; P1, P2 - Pinholes used to isolate the first diffraction order; O - Objective lens and translation stage; SPAD - Single-Photon Avalanche Diode.

An important consideration is that the spatial extent of a Hermite-Gauss mode of order m scales as $\sim w_0\sqrt{m+1/2}$, where w_0 is the beam waist of the fundamental mode. Consequently, higher-order modes typically require a larger aperture in the detection optics. When accounting for this scaling in practical implementations, the Fisher information scales as $\mathcal{FI} \sim \sqrt{m+1/2}$. However, in the *ideal case*–where the detection aperture does not impose any constraints–the Fisher information retains its optimal scaling of $\mathcal{FI} \sim (m+1/2)$ (see Eq. (5)). We experimentally implemented the scheme using Hermite-Gauss modes with orders $m = 0, 1, 2, 8$, and 17. The experimental setup is illustrated in Fig. 3. A suitably attenuated 808 nm laser beam was directed onto a Spatial Light Modulator (SLM) programmed with a custom-designed hologram [27] to generate superpositions of displaced Hermite-Gauss modes of the desired order. The mode generated at any given instant takes the form:

$$\begin{aligned}|\Psi\rangle \;&=\; |\Psi(x+s/2)\rangle + e^{i\phi}\,|\Psi(x-s/2)\rangle \\ &=\; |\mathcal{HG}_m(x+s/2)\rangle + e^{i\phi}\,|\mathcal{HG}_m(x-s/2)\rangle,\end{aligned} \tag{7}$$

where $e^{i\phi}$ is a randomly chosen phase factor between the two modes. For each set of measurements corresponding to a particular mode m, we randomly sample the relative phase $\phi \in [-\pi, +\pi]$ in order to simulate an incoherent mixture of the displaced modes, as described by the density matrix in Eq. (2). The resulting beam is then directed to a second Spatial Light

Modulator, which displays a hologram corresponding to the appropriate projection mode. The output is coupled into a single-mode fibre and detected using a Single-Photon Avalanche Diode (SPAD) connected to a photon-counting module. For each mode m, we first optimize the coupling efficiency to minimize crosstalk between adjacent modes $m-1$, m, and $m+1$. Displacements are then introduced in the range $s \in [0, 1.4w]$ in steps of $w/100$, where w is the beam waist–this step size is close to the resolution limit of the SLM. For each displacement value, photon counts are accumulated for projections onto modes $m-1$, m, and $m+1$, across randomly sampled phase values. From the photon count statistics, we extract mode probabilities and estimate the displacement using a Maximum Likelihood Estimation (MLE) approach. The variances in the estimated displacements are then computed and plotted in Fig. 5. We observe an order-of-magnitude improvement in estimation precision when comparing lower-order modes with higher-order cases, particularly for $m = 8$ and $m = 17$.

In summary, we have demonstrated that probing incoherent transverse displacements using higher-order Hermite-Gauss (HG) modes leads to a sensitivity enhancement that scales linearly with the mode order, provided that projective measurements are performed onto neighboring spatial modes. This stands in contrast to conventional direct imaging techniques, which suffer from diminished Fisher information in the small-displacement regime. We presented a proof-of-principle experimental realization, observing an order-of-magnitude improvement in sensitivity compared to standard SPADE measurements when using HG modes with order $m \geq 8$. Our findings also offer a reinterpretation of the recent experiment reported in Ref. [28], where SPADE was applied to a correlated photon-pair source, and the transverse displacement was introduced on the idler photon. In that work, the observed Fisher information scaled with the square root of the Schmidt number, providing an effective estimate for the number of entangled HG modes comprising the biphoton state. Under the Klyshko picture, detection in mode m on the signal arm corresponds to post-selecting a process in which the idler photon is prepared in the same HG mode, undergoes a transverse displacement, and is subsequently projected onto neighboring modes – an operationally equivalent scenario to our present experiment. Future investigations may explore this approach with pump beams prepared in higher-order HG modes, potentially revealing a pathway to quantum-enhanced displacement sensing. In our implementation, we employed sequential projective techniques based on amplitude flattening, which inherently involve a trade-off between mode-dependent losses and inter-mode crosstalk [29]. However, advanced mode projection strategies, such as those utilizing multi-

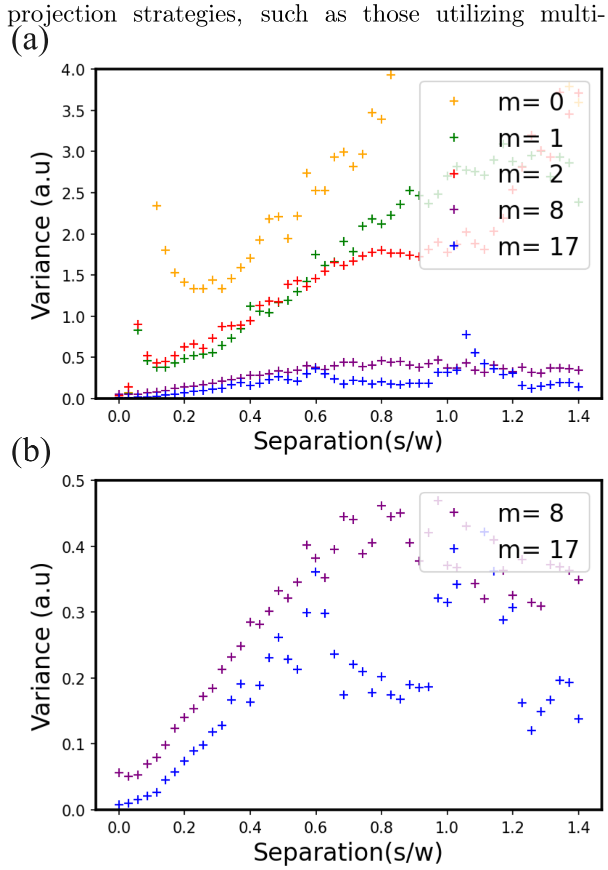

Figure 4. **Experimentally Measured Variances.** (a) Variances in displacement estimates extracted from optimal projections for input modes $m = 0$, 1, 8, and 17. (b) A magnified view of the variances for $m = 8$ and $m = 17$, highlighting the improvement in precision relative to the fundamental mode $m = 0$ shown in (a). An order-of-magnitude reduction in estimation error is observed for the higher-order modes.

plane light converters, have recently been demonstrated for SPADE at the single-photon level [30, 31], and could serve as a robust alternative for practical deployment. We therefore believe that the techniques demonstrated in this work, combined with state-of-the-art optical technologies, hold strong promise for the development of compact and precise devices capable of detecting minute displacements–particularly in applications involving nanoscale systems [32] and high-resolution imaging of birefringent materials.

Acknowledgments– This work was supported by the Canada Research Chair (CRC) Program, the Joint Center for Extreme Quantum Photonics (JCEP) of NRC-uOttawa through the Quantum Sensors Challenge Program at the National Research Council of Canada, and the Quantum Enhanced Sensing and Imaging Alliance Consortium Quantum Grant (QuEnSI).

[1] L. Rayleigh, The London, Edinburgh, and Dublin Philosophical Magazine and Journal of Science **8**, 261 (1879).
[2] E. Ash and G. Nicholls, Nature **237**, 510 (1972).
[3] E. Betzig and J. K. Trautman, Science **257**, 189 (1992).
[4] M. Von Ardenne, Zeitschrift für Physik **109**, 553 (1938).
[5] J. Tersoff and D. R. Hamann, Physical review letters **50**, 1998 (1983).
[6] O. Kafri and I. Glatt, *The physics of moiré metrology* (Wiley New York, 1990).
[7] R. Barboza, A. Babazadeh, L. Marrucci, F. Cardano, C. de Lisio, and V. D'Ambrosio, Nature communications **13**, 1080 (2022).
[8] H. Zang, Z. Xi, Z. Zhang, Y. Lu, and P. Wang, Science Advances **8**, eadd1973 (2022).
[9] H. Zang, Z. Zhang, Z. Huang, Y. Lu, and P. Wang, Science Advances **10**, eadk2265 (2024).
[10] G. H. Yuan and N. I. Zheludev, Science **364**, 771 (2019).
[11] A. N. Jordan, J. C. Howell, N. Vamivakas, and E. Karimi, arXiv preprint arXiv:2505.22925 (2025).
[12] M. Tsang, R. Nair, and X.-M. Lu, Physical Review X **6**, 031033 (2016).
[13] R. Kerviche, S. Guha, and A. Ashok, in *2017 IEEE International Symposium on Information Theory (ISIT)* (IEEE, 2017) pp. 441–445.
[14] M. Paúr, B. Stoklasa, Z. Hradil, L. L. Sánchez-Soto, and J. Rehacek, Optica **3**, 1144 (2016).
[15] P. Boucher, C. Fabre, G. Labroille, and N. Treps, Optica **7**, 1621 (2020).
[16] W.-K. Tham, H. Ferretti, and A. M. Steinberg, Physical review letters **118**, 070801 (2017).
[17] Z. Hradil, J. Řeháček, L. Sánchez-Soto, and B.-G. Englert, Optica **6**, 1437 (2019).
[18] K. Liang, S. A. Wadood, and A. Vamivakas, Optica **8**, 243 (2021).
[19] S. Kurdzialek, Quantum **6**, 697 (2022).
[20] M. Gessner, C. Fabre, and N. Treps, Physical Review Letters **125**, 100501 (2020).
[21] Y. L. Len, C. Datta, M. Parniak, and K. Banaszek, International Journal of Quantum Information **18**, 1941015 (2020).
[22] J. Yang, S. Pang, Y. Zhou, and A. N. Jordan, Physical Review A **100**, 032104 (2019).
[23] S. Zhou and L. Jiang, Physical Review A **99**, 013808 (2019).
[24] K. K. Bearne, Y. Zhou, B. Braverman, J. Yang, S. Wadood, A. N. Jordan, A. Vamivakas, Z. Shi, and R. W. Boyd, Optics Express **29**, 11784 (2021).
[25] A. Pushkina, G. Maltese, J. Costa-Filho, P. Patel, and A. Lvovsky, Physical Review Letters **127**, 253602 (2021).
[26] M. Tsang, R. Nair, and X.-M. Lu, Physical Review X **6**, 031033 (2016).
[27] E. Bolduc, N. Bent, E. Santamato, E. Karimi, and R. W. Boyd, Optics letters **38**, 3546 (2013).
[28] F. Grenapin, D. Paneru, A. D'Errico, V. Grillo, G. Leuchs, and E. Karimi, Physical Review Applied **20**, 024077 (2023).
[29] F. Bouchard, N. H. Valencia, F. Brandt, R. Fickler, M. Huber, and M. Malik, Optics express **26**, 31925 (2018).
[30] C. Rouvière, D. Barral, A. Grateau, I. Karuseichyk, G. Sorelli, M. Walschaers, and N. Treps, Optica **11**, 166 (2024).
[31] L. Santamaria, F. Sgobba, and C. Lupo, Optica Quantum **2**, 46 (2024).
[32] M. Choi, C. Pluchar, W. He, S. Guha, and D. Wilson, arXiv preprint arXiv:2411.04980 (2024).

Appendix A: Fisher Information at Arbitrary Separation

Here, we extend the Fisher Information Analysis to the regime of arbitrary large displacements and show that the sensitivity is enhanced even at large separations depending upon the mode order m. At large separations, the mth mode in addition to $m-1$, and $m+1$ also contains a significant amount of Fisher information for the separation parameter. Thus our optimal projections for large enough separations is

$$|m+1\rangle = |\mathcal{HG}_{m+1}(x)\rangle \quad (A1)$$
$$|m\rangle = |\mathcal{HG}_{m}(x)\rangle \quad (A2)$$
$$|m-1\rangle = |\mathcal{HG}_{m-1}(x)\rangle \quad (A3)$$

We first evaluate the probability for projection unto $|m+1\rangle$

$$\begin{aligned} P_{m+1} &= \frac{1}{2}\left|\langle m+1|\Psi^+\rangle\right|^2 + \frac{1}{2}\left|\langle m+1|\Psi^-\rangle\right|^2 \\ &= \frac{1}{2}\left|\langle m+1|m^+\rangle\right|^2 + \frac{1}{2}\left|\langle m+1|m^-\rangle\right|^2 \end{aligned} \quad (A4)$$

where, $|m^{\pm}\rangle$ refer to the displaced HG mode, $\mathcal{HG}_m(x \pm s/2)$. We proved in our previous work [28] that for $m \geq n$

$$\langle m|n^{\pm}\rangle = \sqrt{\frac{n!}{m!}} 2^{\frac{n-m}{2}} (\mp s)^{m-n} e^{-\frac{s^2}{4}} \mathcal{L}_n^{m-n}(\frac{s^2}{2}) \quad (A5)$$

which gives us,

$$\langle m+1|m^{\pm}\rangle = \sqrt{\frac{1}{m+1}} 2^{\frac{-1}{2}} (\mp s)^1 e^{-\frac{s^2}{4}} \mathcal{L}_m^1(\frac{s^2}{2}). \quad (A6)$$

Substituting this in Eqn (A4) and simplifying we get,

$$P_{m+1} = \frac{1}{8(m+1)} e^{-\frac{s^2}{8}} s^2 \left(\mathcal{L}_m^1\left(\frac{s^2}{8}\right)\right)^2. \quad (A7)$$

And similarly, the probability for projection unto $|m-1\rangle$, and $|m\rangle$ can be evaluated and the final expression assumes the form,

$$P_{m-1} = \frac{1}{8m} e^{-\frac{s^2}{8}} s^2 \left(\mathcal{L}_{m-1}^1\left(\frac{s^2}{8}\right)\right)^2 \quad (A8)$$
$$P_m = e^{-\frac{s^2}{8}} \left(\mathcal{L}_m^0\left(\frac{s^2}{8}\right)\right)^2. \quad (A9)$$

The Fisher information in these two projections then can be evaluated as,

$$\begin{aligned} \mathcal{FI} &= \sum_{i=1,0,-1} \frac{1}{P_{m+i}}\left(\frac{\partial P_{m+i}}{\partial s}\right)^2 \\ &= \frac{e^{-\frac{s^2}{8}}\left(s^2\mathcal{L}_{m-1}^2\left(\frac{s^2}{8}\right) + \left(0.5s^2-4\right)\mathcal{L}_m^1\left(\frac{s^2}{8}\right)\right)^2}{32(n+1)} \\ &+ \frac{e^{-\frac{s^2}{8}}\left(s^2\mathcal{L}_{m-2}^2\left(\frac{s^2}{8}\right) + \left(0.5s^2-4\right)\mathcal{L}_{m-1}^1\left(\frac{s^2}{8}\right)\right)^2}{32n} \\ &+ \frac{e^{-\frac{s^2}{8}}\left(s\mathcal{L}_m\left(\frac{s^2}{8}\right) + 2s\mathcal{L}_{m-1}^1\left(\frac{s^2}{8}\right)\right)^2}{16}. \end{aligned}$$

The Fisher Information approaches the previously derived value of $m+\frac{1}{2}$ for $s \to 0$. The Cramer-Rao bounds for the variances can be derived using $(\Delta\sigma)^2 \geq \frac{1}{\mathcal{FI}}$. The variances for different measurements using different modes along with the Fisher Information are plotted in Figure 2.

Appendix B: Fisher Information for coherent separations

Here we extend the calculation of fisher information for coherent displacements. Say the material introduces coherent displacement with a coherence parameter γ, where $\gamma = e^{i\phi}$, between the positively and negatively displaced states. The normalized state after such interaction becomes,

$$\begin{aligned} |\Psi\rangle &= \frac{1}{\sqrt{2}}\left(|\Psi^+\rangle + \gamma\,|\Psi^-\rangle\right) \\ &= \frac{1}{\sqrt{2}}\left(|\mathcal{HG}_m(x-s/2)\rangle + \gamma\,|\mathcal{HG}_m(x+s/2)\rangle\right). \end{aligned}$$

For small separations, one can expand the displaced wavefunctions in terms of a Taylor series with higher order derivatives as before,

$$\langle x|\Psi(x \pm s/2)\rangle \approx \langle x|\Psi\rangle \pm s/2\,\langle x|\Psi\rangle' + O(s^2) \quad (B1)$$
$$\approx \langle x|\mathcal{HG}_m\rangle \pm s/2\,\langle x|\mathcal{HG}_m(x)\rangle' \quad (B2)$$

Hence if we perform projective measurement onto the modes,

$$|m+1\rangle = |\mathcal{HG}_{m+1}(x)\rangle, \quad (B3)$$
$$|m-1\rangle = |\mathcal{HG}_{m-1}(x)\rangle, \quad (B4)$$

for the state in Equation B1 the detection probabilities are given by,

$$P_{m\pm1} = \frac{1}{2}\left|\langle m\pm1|\Psi^+\rangle + \gamma\,\langle m\pm1|\Psi^-\rangle\right|^2$$

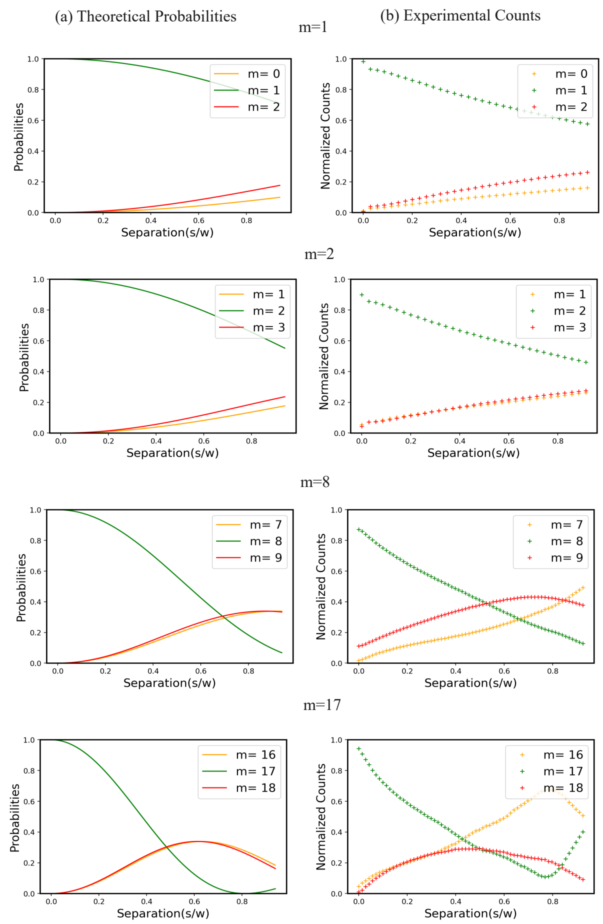

Figure 5. Theoretical Probabilities (a) versus the Experimental counts (b) for the $m-1$, m, and $m+1$th modes for $m = 1$, $m = 2$, $m = 8$, and $m = 17$.

Using the orthonormality of Hermite Gauss expansion and the explicit form for the derivative, one can show that,

$$P_{m+1} = \frac{s^2}{8}(m+1)(1-\gamma)^2, \quad \text{and} \quad P_{m-1} = \frac{s^2}{8}m(1-\gamma)^2. \tag{B5}$$

The total Fisher information per photon in this set of measurements is given by,

$$\begin{aligned} \mathcal{FI} &= \frac{1}{P_{m+1}}\left(\frac{\partial P_{m+1}}{\partial s}\right)^2 + \frac{1}{P_{m-1}}\left(\frac{\partial P_{m-1}}{\partial s}\right)^2 \\ &= \left(\frac{m+1}{2} + \frac{m}{2}\right)(1-\gamma)^2 \\ &= \left(m + \frac{1}{2}\right)(1-\gamma)^2 . \end{aligned} \tag{B6}$$

We see that the Fisher information is maximized and approaches the incoherent case as $\gamma = -1$ or $\phi = \pi$, i.e. when the two displacement are out of phase with each other. Whereas in case of displacements that are in phase, the Fisher Information is zero. We see that the enhancement obtained from the mode order m is still present.

Superresolution Enhancement in Biphoton Spatial-Mode Demultiplexing

Florence Grenapin,[1] Dilip Paneru,[1] Alessio D'Errico,[1,*] Vincenzo Grillo,[2] Gerd Leuchs,[1,3] and Ebrahim Karimi[1,3]

[1] *Nexus for Quantum Technologies, University of Ottawa, Ottawa, Ontario K1N 6N5, Canada*
[2] *Istituto Nanoscienze, Consiglio Nazionale delle Ricerche, Via G. Campi 213/A, Modena 41125, Italy*
[3] *Max Planck Institute for the Science of Light, Erlangen 91058, Germany*

(Received 31 January 2023; revised 14 June 2023; accepted 26 July 2023; published 31 August 2023)

Imaging systems measuring intensity in the far field succumb to Rayleigh's curse, a resolution limitation dictated by the finite aperture of the optical system. Many proof-of-principle and some two-dimensional imaging experiments have shown that, by using spatial mode demultiplexing (SPADE), the field information collected is maximal, and, thus, the resolution increases beyond the Rayleigh criterion. Hitherto, the SPADE approaches are based on resolving the lateral splitting of a Gaussian wave function. Here, we consider the case in which the light field originates from a biphoton source, i.e., spontaneous parametric down-conversion, and a horizontal separation is introduced in one of the two photons. We show that a separation induced in the signal photon arm can be superresolved using coincidence measurements after projecting both photons on Hermite-Gauss modes. Remarkably, the Fisher information associated with the measurement is enhanced compared to the ordinary SPADE techniques by $\sqrt{K}$, where K is the Schmidt number of the two-photon state that quantifies the amount of spatial entanglement between the two photons.

DOI: 10.1103/PhysRevApplied.20.024077

I. INTRODUCTION

The resolution of far-field optical imaging systems based on direct intensity measurements is limited by the point spread function (PSF), a diffraction phenomenon dictated by light wavelength and aperture width of the optics involved [1]. The accuracy of this measurement diverges for small separations of two-point sources; an effect also referred to as "Rayleigh's curse." The discovery of this phenomenon has encouraged research efforts in other fields of imaging, such as near-field imaging [2,3] or imaging based on electronic effects [4,5], which goes beyond the optical Rayleigh limit. In 2016, Tsang and his colleagues proposed a simple spatial mode demultiplexing (SPADE) scheme, which is robust to the resolution curse [6]. It shows that our ability to estimate a separation between two incoherent point sources collapses as the separation approaches zero when using conventional intensity measurements, thus assimilating Rayleigh's curse to an intrinsic loss of Fisher information at small separations. The SPADE scheme proposed uses spatial mode sorting, with mode projections tailored to the PSF of the imaging system, which collects maximal Fisher information regardless of the separation magnitude. This has prompted many further theoretical and experimental findings in recent years, exploring applications and modifications of SPADE for different imaging systems [7–10], coherent point sources [11–13], limitations in the presence of cross-talk or other noise sources [14,15], and even extensions to higher-dimensional objects [16,17]. Although the explicit model estimating all points of an arbitrary two-dimensional (2D) object is vastly complicated to derive in terms of Fisher information, 2D imaging simulations [18] and experiments [19] using postprocessing algorithms (deconvolution, machine learning) have shown an increase in resolution beyond the Rayleigh limit. This solidifies the intuition relating the distinguishability of two-point sources to the overall resolution of a 2D imaging system.

The main idea behind SPADE is to estimate the separation between two-point sources by looking at the alteration of the field's phase, in particular, at the change in phase symmetry, which can be efficiently probed by the Hermite-Gauss (HG) decomposition for the usual Gaussian PSF. In this work, we address the following question: can the spatial correlations emerging from two-photon sources enhance the resolution sensitivity? We show that it is possible to superresolve a separation using mode sorting in coincidence measurements with a PSF that is itself entangled in the form of spontaneous parametric down-conversion (SPDC) light. More specifically, we consider a two-photon wave function that allows a Schmidt decomposition in HG modes, with Schmidt number K. An incoherent displacement, which mimics the effect of a transmitting sample, is applied on one of the two photons, and the displacement is estimated by projecting the resulting state on direct products of HG modes. We note that the somewhat related inverse problem of generating a spatially or temporally shaped pure photon state in one beam of an entangled pair (ghost interference) likewise requires the projection on pure states in the other beam of the entangled pair [20]. Our main result shows that the Fisher information, whose inverse gives a lower bound on the estimation error, scales as $\sqrt{K}/2$, where $K = 1$ corresponds to the separable case of a Gaussian point spread function. Hence, any spatially entangled two-photon source provides an advantage with respect to the ordinary SPADE. Here, we derive this result and present a first proof-of-principle experimental implementation. We conclude by discussing the possible settings in which the two-photon SPADE can give a practical advantage.

II. THEORY

To understand the resolution limits of a given experimental technique, one must evaluate the lower bound on the achievable uncertainty of the estimator δ (which, in our case, is the lateral displacement). This limit is given by the Cramer-Rao bound [6,21]: the estimator's standard error is lower bounded by the inverse of the Fisher information $\Delta\delta \geq 1/\sqrt{n\mathcal{FI}}$ [22,23], where n corresponds to the number of repeated measurements and the Fisher information, $\mathcal{FI}$, can be calculated from the probabilities $\mathcal{P}_j$ of a given measurement outcome j as $\mathcal{FI} = \sum_j (1/\mathcal{P}_j)(\partial\mathcal{P}_j/\partial\delta)^2$. In the following, we consider the problem of resolving an incoherent transverse displacement of a photon that is in a spatially correlated state with another idler photon. We calculate the Fisher information for a biphoton spatial mode demultiplexing scheme and compare the result with the classical SPADE, which emerges from the uncorrelated limit of our scenario.

In a typical imaging setup, the image plane of a point source is described by a two-dimensional PSF $\Psi(\mathbf{r})$ [with $\mathbf{r} = (x, y)$]. In the case of two incoherent point sources separated horizontally by a distance s, the wave function in the image plane can be described by the mixed state $\rho = \frac{1}{2}(|\Psi^+\rangle\langle\Psi^+| + |\Psi^-\rangle\langle\Psi^-|)$, where $\langle x|\,\Psi^\pm\rangle := \Psi(x \pm s/2, y)$. An intensity measurement, which corresponds to a projective measurement in the position bases, results in outcomes with distribution $I(x,y) = \frac{1}{2}(|\Psi^+|^2 + |\Psi^-|^2)$. The Fisher information for the direct imaging method is known to rapidly fall to zero for separations smaller than the width of the point spread function [6]. However, by mode sorting using modes that form orthogonal bases for space containing the PSF (SPADE), the total Fisher information remains constant across all values of s [6]. Optimal bases are ones in which most of the Fisher information for small s is captured in the first couple of measurements, making schemes like binary SPADE [10] simple and attractive. We show in Appendix A how a projection on the derivative of the PSF with respect to the coordinate associated with the direction of the displacement is an optimal projection for the small separation regime. More rigorous ways to determine optimal measurement bases have been developed [7].

In a coincidence imaging setup with entangled SPDC photon pairs, there is no pure wave function describing one of the single photons' quantum states. The single particle state is maximally mixed, which can mimic a Gaussian in its intensity pattern when viewed on the camera. The pure state describing the entangled particles is a biphoton state of signal and idler that can be expressed in the Schmidt basis of HG modes [24]:

$$|\Psi\rangle = \sum_{m,n} C_{mn}\,|m,n\rangle_s \otimes |m,n\rangle_i\,. \qquad (1)$$

Here the C_{mn} coefficients are the Schmidt coefficients of the HG decomposition and $|m,n\rangle$ states are the 2D HG modes of order (m,n) with a beam waist parameter w: $\langle x,y|\,m,n\rangle := \mathrm{HG}_{m,n}(x,y) = \mathcal{N}\exp(-(x^2 + y^2)/w^2)H_m(\sqrt{2}x/w)H_n(\sqrt{2}y/w)$ with the $H_m(x)$ Hermite polynomials and $\mathcal{N}$ a normalization constant. In this basis, the correlations are diagonal: a signal photon in a particular $|i,j\rangle$ mode is entangled with an idler photon in that exact mode (see Appendix B). In practice, any action occurring on one photon, such as the typical diffraction causing PSFs, is also reflected in the biphoton wave function. The Schmidt coefficients can be given an analytical expression (see Refs. [25,26]): $C_{m,n} = |(\gamma-1)/(\gamma+1)|^{m+n}4\gamma/(1+\gamma)^2$ with $\gamma = (1/w_p)\sqrt{L\lambda_p/2\pi}$ a parameter defined by crystal length L, pump beam waist w_p, and wavelength λ_p. Here, we investigate how two-photon SPADE allows us to superresolve separation introduced in one of the photon paths as if the PSF was of the form of the source (just as in Refs. [9,10])—which is the biphoton wave function described above.

Finding the optimal basis of projection for SPADE is not as straightforward as in the single-photon PSF cases. Although the derivative of the biphoton PSF with respect to the signal photon's coordinates can be calculated directly (Appendix B), this is a nonseparable state for which it is challenging to devise a single-shot projector experimentally. However, we note that interesting progress is being made in that direction [27]). Instead, as in ordinary SPADE, we consider the projection on the basis of direct products of HG modes $\{|m,n\rangle_s\langle m,n| \otimes |m,n\rangle_i\langle m,n|\}$. The expression for a projection onto mode $\mathrm{HG}_{k,l}(x_i,y_i)$ in the idler arm and $\mathrm{HG}_{k',l'}(x_s,y_s)$ in the signal arm can be derived as

$$ {}^{k',l'}_{k,l}\mathcal{P}_{\text{coinc}} = \frac{1}{2} C^2_{k',l}\delta_{l,l'} \sum_{\pm} |\langle k|\, k'^{\pm}\rangle|^2. \qquad (2)$$

With $s = 0$, the correlations are diagonal: only projections where $k = k'$ have nonzero outcomes. As s increases, contributions from the first off-diagonal modes appear. Equation (2) can be given an analytical expression using the result $\langle m|\, n^{\pm}\rangle = \sqrt{m!/n!}\, 2^{(m-n)/2}(\pm s/2)^{n-m} e^{-s^2/16}$ $\mathcal{L}_m^{n-m}(s^2/8)$, where $\mathcal{L}_i^{\alpha}$ is the αth generalized Laguerre polynomial of order i, α and $n \geq m$ (see Appendix C for the derivation).

For small values of s, we consider the expansion of ${}^{k',l'}_{k,l}\mathcal{P}_{\text{coinc}}$ to the order of $(s/2)^2$ by substituting $|m^{\pm}\rangle = |m\rangle \pm s\,|m\rangle'/4 + O(s^2/16)$ into Eq. (2). The result $\mathcal{P}_{kl}^{k'l'} \approx C^2_{k',l}\{\delta_{k,k'}\{1 - s^2(2k'+1)/8\} + \delta_{k,k'-1}k'/2 + \delta_{k,k'+1}(k'+1)/2\}\delta_{l,l'}$ implies that, for each mode k considered in the signal beam, only the neighboring k' modes give nonzero coincidence counts: $\mathcal{P}_{kl}^{kl} \approx C^2_{k,l}(1 - s^2(2k+1)/8)$, $\mathcal{P}_{kl}^{k+1,l} \approx s^2 C^2_{k+1,l}(k+1)/8$, $\mathcal{P}_{kl}^{k-1,l} \approx s^2 C^2_{k-1,l}k/8$. Of these terms, only the $k = k', k' \pm 1$ modes varying quadratically with the separation will translate to a nonzero Fisher information in the small separation regime, $s \to 0$ (see Appendix D):

$$\mathcal{FI}_{kl}^{kl}(s) \approx \frac{[C^2_{k,l}(2k+1)s/2]^2}{4 - s^2(2k+1)/2} \to 0, \qquad (3a)$$

$${}^{k+1}_{k}\mathcal{FI}_{\text{coinc}} = \tfrac{1}{2}(k+1)C^2_{k+1,l}, \qquad (3b)$$

$${}^{k-1}_{k}\mathcal{FI}_{\text{coinc}} = \tfrac{1}{2}kC^2_{k-1,l}. \qquad (3c)$$

Since the Fisher information in these particular projections is independent of the separation s, the variance of our separation estimates does not suffer from the so-called Rayleigh curse, similar to the SPADE technique for a single photon.

The total Fisher information can then be obtained by summing the individual contributions from all of the detected modes. Interestingly, for small values of s, the total has an upper bound dictated by the strength of the spatial correlation between the photon pair. More precisely,

$${}^{\text{tot}}_{\text{2D}}\mathcal{FI}_{\text{coinc}} = \gamma + \gamma^{-1} = \frac{\sqrt{K}}{2} \geq \frac{1}{2}, \qquad (4)$$

where $K = \frac{1}{4}[\gamma + 1/\gamma]^2$ is the Schmidt rank often used to quantify the strength of bipartite entanglement (see

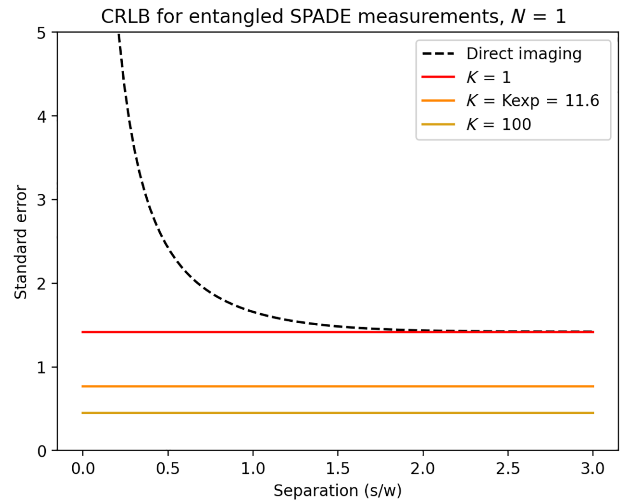

FIG. 1. Cramer Rao lower bounds (CRLBs) versus the separation (units of the Schmidt waist, $w = \sigma_s$). Classical SPADE measurements (lower bounded by $K = 1$) attain the SQL precision. Higher values of entanglement provide an advantage over classical SPADE. Kexp, experimental Schmidt number.

Appendix B for the derivation). This leads to a corresponding lower bound in the achievable precision as

$$\Delta\hat{s}^2 \geq \frac{2}{\sqrt{K}}, \qquad (5)$$

where $\Delta\hat{s}^2$ is the variance in the separation estimates. The result suggests that the precision in the measurement of near-zero separations is limited only by the strength of the spatial correlations, thereby suggesting high-dimensional entanglement as a promising resource for superresolution measurements. Not only does the method circumvent the so-called "Rayleigh curse" like the ordinary SPADE (which is bounded by the special case of $K = 1$; see Fig. 1), but it also offers further enhancement proportionate to the correlations in the system. In what follows, we describe in detail an experimental implementation and results of the method outlined above, along with some simulation results.

III. METHODS

For the purpose of a simpler experimental implementation in the laboratory, we considered a smaller subspace spanned by modes with $l = 0$ (i.e., $\text{HG}_{00}, \text{HG}_{01}, \text{HG}_{02}, \ldots, \text{HG}_{0n}$) for both the signal and idler photons. The total Fisher information associated with this set of joint projective measurements can be written as (see Appendix D)

$${}^{\text{tot}}_{\text{1D}}\mathcal{FI}_{\text{coinc}} = \frac{1}{2} + \frac{1}{2}\left(\frac{1-\gamma}{1+\gamma}\right)^2. \qquad (6)$$

Experimentally, we reconstructed the correlation matrices in the HG basis for a biphoton state generated via SPDC for different traverse separations. The separation was then inferred from the observed correlation matrices using maximum likelihood estimation.

A. Experimental realization

The down-converted photon pairs are generated by pumping a 0.5-mm-thick type-I barium borate crystal (BBO) with a 200-mW 405-nm pump beam obtained from the second harmonic generation (SHG) of a 1-GHz 100-fs laser beam. The pump beam is focused to a waist of $w_p = 40\ \mu\text{m}$ at the BBO crystal, which sets a value of $\gamma = 0.15$. The value of γ determines the waist of the Schmidt modes, the Schmidt coefficients in the Hermite Gauss basis, and the Schmidt rank K [26,28]. The generated photon pairs are then split into two paths by a 50:50 beam splitter (BS), and the signal photon travels through an asymmetrical Mach-Zender interferometer (MZI), which introduces a transverse separation between the horizontal and the vertical polarization components of the beam. Two mirrors are placed on translation stages, specific combinations of which allow us to generate a tunable symmetric separation about the center of the undisplaced beam. The MZI also ensures that a path difference of approximately 20 cm exists between the horizontal and the vertical polarization components, which ensures that we have two incoherent point sources. In each of the signal and the idler arms, projections onto the spatial Schmidt modes are realized via the amplitude flattening technique [29,30], whereby a combination of appropriate holograms displayed in spatial light modulators (SLMs) along with suitable demagnification to the fibre plane approximates the ideal projective measurement for a particular spatial mode. The first order of the diffracted light is selected with a pinhole and coupled into a single-mode fibre (SMF) after being filtered by bandpass filters 810 ± 5 nm to ensure the collection of degenerate pairs. Each SMF is then connected to a single-photon avalanche-diode (SPAD) detector (Excelitas SPCM-AQRH-14-FC), and coincidence counts are registered via a time-correlated single-photon counting system. Further details on the experimental setup with the essential components are illustrated in Fig. 2.

To determine the experimental Schmidt waist, multiple sets of data for differing waists of projection were taken for a zero displacement, and the experimental projection waist was chosen so as to have as close to a diagonal density matrix as possible. For each applied separation, the setup was realigned so that the center of the displaced beam was coupled to the fibre. The coincidence counts in the diagonal modes for zero separation account for at least 82% of the total counts in the 7×7 cross-talk matrix. The deviation from a perfectly diagonal decomposition can be attributed to several factors, including a deviation of the pump beam shape from a Gaussian mode and modal cross-talk in the detection scheme. These factors can be tackled, in principle, by improved control of the pump shape (e.g., through spatial filtering or the use of SLMs) and the use of other detection schemes, respectively. Indeed, the recent advances in spatial mode sorting through multiplane converters allow, in principle, a lossless and low cross-talk detection scheme [31].

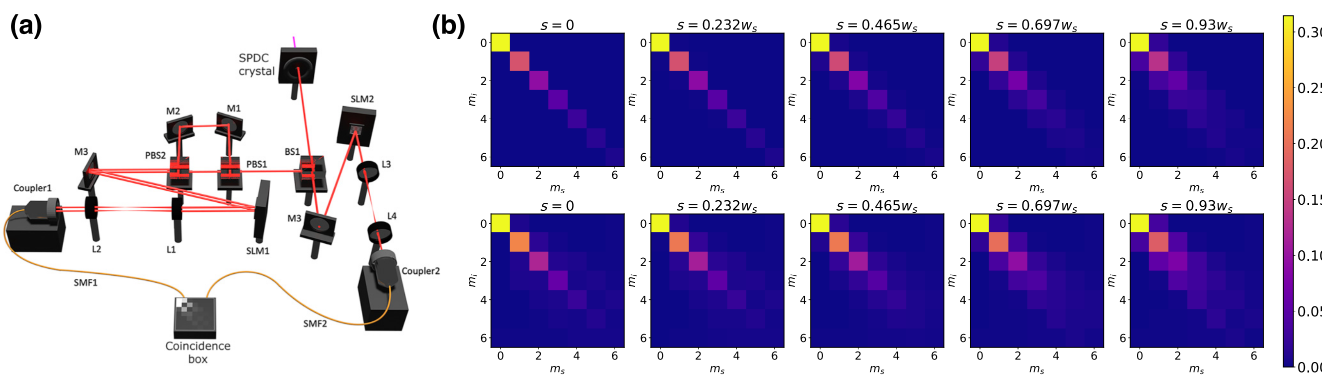

Experimental setup

Theoretical (top) and experimental (bottom) correlation matrices

FIG. 2. (a) A 405-nm laser shines a 1-mm type-I BBO crystal generating degenerate down-converted photon pairs. Idler and signal photons are separated by a 50:50 beam splitter (BS). An unbalanced MZI interferometer implements an incoherent lateral displacement on the signal photon. The two photons are then projected on HG modes by coupling to single-mode fibers (SMFs) after being spatially modified by holograms displayed on spatial light modulators (SLM1 and SLM2). The photons are then detected by a pair of single-photon avalanche-diode (SPAD) detectors and then the coincidence events are detected via a coincidence counting module. PBS, polarizing beam splitter; M1–M3, mirrors; L1–L4, lenses. (b) Theoretical (top) and experimental (bottom) cross-talk matrices showing coincidence counts for the first 7×7 joint projections on signal and idler photons for five different values of separation s between 0 and $0.93w$. We can see the off-diagonal coefficients becoming more prominent as the separation increases.

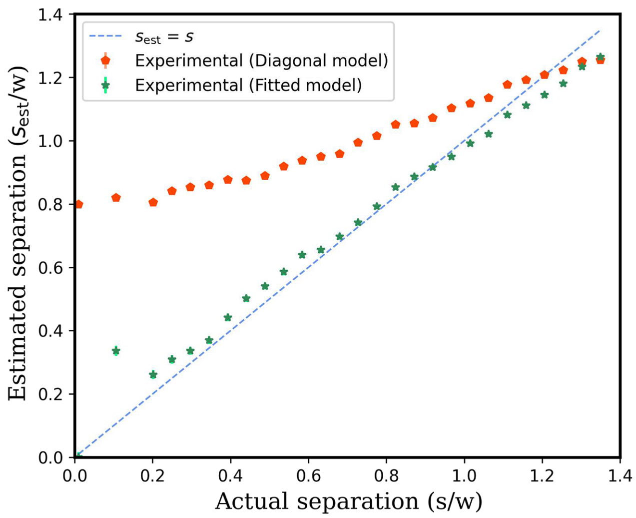

FIG. 3. Estimates from the data versus the actual separation (units of the Schmidt waist, $w = \sigma_s$). The estimation was first performed assuming an ideal theoretical model, i.e., a perfectly diagonal mode decomposition (red) where probabilities are defined by Eq. (2). We see a significant deviation from the ideal $s_{\text{est}} = s$ estimates, most likely due to modal cross-talk, attenuation, and dark counts. Therefore, in order to account for these effects, a linear fitting of the counts, as functions of the theoretical probabilities, was performed before the estimation, the results of which closely match the ideal curve (green).

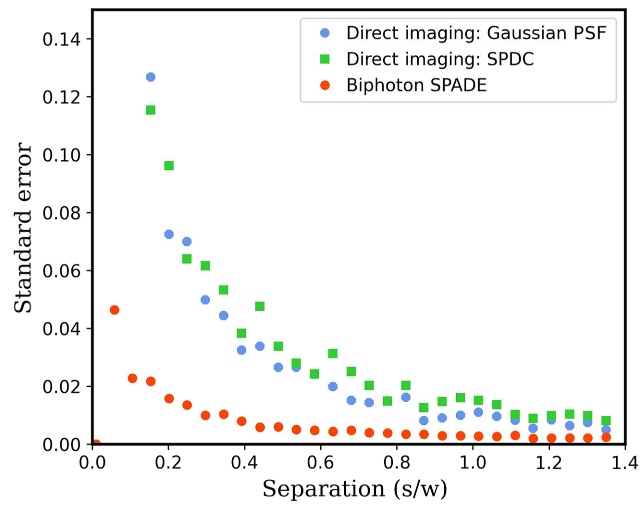

FIG. 4. Simulation results for biphoton SPADE compared with direct imaging of both Gaussian and SPDC PSFs for $N = 37\,000$ photons (separation scaled in units of the Schmidt waist, $w = \sigma_s$). A 50-pixel array was used for direct imaging simulation, corresponding to intensity measurements at 50 different points. Similarly, for the biphoton SPADE ($K = 11.6$), the simulation was done for 49 mode projections with combinations of Hermite-Gauss modes with indices $n = 0, m = 0, \ldots, 6$ for each signal and idler. A maximum likelihood estimation was performed on generated samples, and the standard error in the separation estimates was plotted.

IV. RESULTS

We applied evenly spaced lateral displacements at increments of $0.0465\sigma_s$, from a separation $s = 0$ to $s = 1.35\sigma_s$, and recorded the outcomes of the joint measurements onto modes HG_{n_i,m_i} in the idler arm and HG_{n_s,m_s} in the signal arm for $n_{i/s} = 0$ and $m_{i/s} = 0, 1, \ldots, 6$. Each set of data is then a 7×7 matrix containing 49 joint projection outcomes, the coincidence counts for each of which were accumulated for up to 60 s. The 7×7 matrix sums were normalized to account for laser intensity fluctuations. For such small separations, to a very good approximation, it can be safely assumed that almost all of the generated photons are in the 7×7 Hilbert space. In total, for each separation, approximately 37 000 photons were collected. The results for a few sets of displacements, along with the corresponding theoretical predicted outcomes [Eq. (2)] are illustrated in the form of correlation matrices [see Fig. 2(b)]. The figure shows that the experimental outcomes closely match the corresponding theoretical predictions. We also see the modes just outside the diagonal starting to increase in significance symmetrically with increasing separation. In order to obtain the estimates of the separation parameter s, first, we perform the least-squares fitting for the normalized counts (or, equivalently, probabilities) to the expression $P_{ij} = \alpha_{ij}\mathcal{P}_{ij} + \beta_{ij}$, where the $\mathcal{P}_{ij}$ are the theoretical probabilities given by Eq. (2), α_{ij} is a scaling factor to account for attenuation for different modes, and β_{ij} is an additive factor to account for the spurious photon counts. For each separation, we then applied a maximum likelihood estimation procedure, maximizing the likelihood function defined as $L(s) := (N!/\prod n_{ij}!)\prod_{ij} P_{ij}(s)^{n_{ij}}$, where the $n_{i,j}$ are the photon counts for the joint projection onto HG_{0i} for the signal and HG_{0j} for the idler, and N is the total photon counts in all of the modes for that particular separation. The results of the estimation are shown in Fig. 3.

In order to compare the precision in the estimates obtained from this method with direct imaging, we also performed simulation runs of the experimental outcomes for the direct imaging of the SPDC point sources whose mode decomposition is characterized by $\gamma = 0.15$. The simulation results are plotted in Fig. 4. We see that the biphoton SPADE outperforms the direct imaging of the SPDC and also the direct imaging of the Gaussian with the same waist as the Schmidt waist, offering an order-of-magnitude advantage especially for near zero separations.

V. DISCUSSION AND CONCLUSION

We have theoretically derived optimal projective measurements for separation estimation using a biphoton wave function generated via the SPDC process. The Fisher information for projection onto these modes remains constant even for near zero separation, which shows that the measurement scheme is not plagued by the so-called "Rayleigh curse" inherent in direct imaging. Moreover, the precision in the proposed method is limited only by the strength of the spatial correlations inherent in the photon pairs. In particular, we show that the total Fisher information of the separation estimation is proportional to the square root of the Schmidt rank (K) of the system. Therefore, depending upon the strength of the correlations in the system, the method even offers further enhancement that scales with K compared to ordinary SPADE, which corresponds to the trivial case of $K = 1$. As a proof of concept, we also experimentally implemented the scheme using down-converted photon pairs and obtained results that are in good agreement with the theoretical predictions. We also performed simulations comparing the precision in our estimates with the case of direct imaging, where we indeed observed at least an order-of-magnitude improvement, especially for near zero separations, where the errors start to diverge. Our theoretical and experimental results suggest the potential of using high-dimensional entanglement for further enhancing superresolution measurements. Combined with neural networks (see, e.g., Ref. [19]), this technique can provide a new tool for high-resolution imaging in low-light conditions of passive samples with variable transmissivity. As a perspective, we believe that these ideas may also have an appeal in electron microscopy where the resolution problem is very relevant, especially when trying to separate two close pointlike objects such as atoms. Optimal measurements (to which SPADE belongs) in the single electron framework have been already studied [32], but the recent advances in controlling entangled electrons [33,34] could pave the way to increase the resolution below 10 pm, which would be the highest spatial resolution achieved so far. More generally, the Schmidt decomposition of an electron pair could provide a new framework for advanced metrology in quantum transmission electron microscopy.

ACKNOWLEDGMENTS

E.K. acknowledges scientific discussions with Professor Aephraim Steinberg. This work was supported by the Canada Research Chair (CRC) Program, NRC-uOttawa Joint Centre for Extreme Quantum Photonics (JCEP) via the Quantum Sensors Challenge Program at the National Research Council of Canada, and the European Union's Horizon 2020 Research and Innovation Programme under Grant Agreement No 766970 (QSORT).

APPENDIX A: OPTIMAL PROJECTION

Fisher information describes the amount of information a measurement contains about a certain parameter being estimated. The Cramer-Rao lower bound, which is the minimum possible variance on the unbiased estimation of the parameter, is given by the inverse of the Fisher information [22],

$$\sigma_{\text{crlb}} \geq \frac{1}{\sqrt{\mathcal{FI}}} \geq \frac{1}{\sqrt{\text{Tr}[(\partial\rho/\partial\delta)L]}}, \tag{A1}$$

where ρ is the state of the system, δ is the parameter to be estimated, and L is the so-called symmetric logarithmic operator defined as $\rho L + L\rho = 2\partial\rho/\partial\delta$. The higher the Fisher information associated with a particular set of measurements, the better the precision in the estimates.

In superresolution schemes for separation estimation with the so-called spatial mode demultiplexing, a projective measurement is carried out in spatial modes (most commonly in the Hermite-Gauss basis). The Fisher information of a parameter δ, in the basis of such a set of spatial modes $\{|j\rangle\langle j|\}$, is given by

$$\mathcal{FI} = \sum_j \frac{1}{\mathcal{P}_j}\left(\frac{\partial \mathcal{P}_j}{\partial\delta}\right)^2, \tag{A2}$$

where $\mathcal{P}_j$ is the probability associated with the successful projection in the corresponding mode $|j\rangle$.

In the small separation regime, where errors from direct imaging start to diverge, one can find an optimal basis of projective measurements for which the Fisher information remains constant. For a general PSF $|\Psi(x)\rangle$, the "optimal" mode of projection is proportional to its derivative, which can be seen as follows. The displaced PSFs $\langle x_s|\Psi\rangle^{\pm} = \langle x_s|\Psi(x\pm s)\rangle$, where $\delta = 2s$, can be expanded in terms of the derivatives of the original PSF as

$$\langle x_s|\Psi\rangle^{\pm} = \sum_n \frac{(\pm s)^n \langle x_s|\Psi\rangle^{(n)}}{n!}, \tag{A3}$$

where $\langle x_s|\Psi\rangle^{(n)}$ is the nth derivative in x_s of $\langle x_s|\Psi\rangle$. For small separations, we can consider only up to the first-order term in the separation,

$$\langle x_s|\Psi\rangle^{\pm} \approx \langle x_s|\Psi\rangle \pm s\,\langle x_s|\Psi\rangle^{(1)} + O(s^2). \tag{A4}$$

If the two displaced PSFs are incoherent then the resulting state is characterized by a completely mixed state,

$$\rho = \tfrac{1}{2}[|\Psi\rangle^{+}\langle\Psi| + |\Psi\rangle^{-}\langle\Psi|], \tag{A5}$$

where $|\Psi\rangle^{\pm}$ refer to the wave functions displaced by $\pm s$ in the x axis.

If we substitute Eq. (A4) into Eq. (A5), we find the density matrix approximated for small separations,

$$\rho_{\approx}|\Psi\rangle\langle\Psi| + s^2|\Psi\rangle^{(1)}\langle\Psi|^{(1)} + \frac{s^2}{2}(|\Psi\rangle^{(2)}\langle\Psi| + |\Psi\rangle\langle\Psi|^{(2)}). \tag{A6}$$

The probability of successful projection onto the normalized first derivative mode is

$$\begin{aligned}\mathcal{P}_{\rm der} &\approx \frac{1}{\mathcal{N}}\,\langle\Psi|^{(1)}\,\rho_{\rm BI}\,|\Psi\rangle^{(1)}\\ &\approx \frac{s^2}{\mathcal{N}}|\,\langle\Psi|^{(1)}\,|\Psi\rangle^{(1)}\,|^2\\ &\approx \frac{s^2}{\mathcal{N}}\\ &= \frac{\delta^2}{4\mathcal{N}},\end{aligned} \tag{A7}$$

where $\mathcal{N}$ is the normalization factor. The Fisher information can be calculated as

$$\mathcal{FI}_{\rm der} = \frac{1}{\mathcal{P}_{\rm der}}\left(\frac{\partial\mathcal{P}_{\rm der}}{\partial\delta}\right)^2 = \mathcal{N}. \tag{A8}$$

We see that in the small separation regime, the Fisher information in the derivative mode is a constant regardless of the separation.

APPENDIX B: SCHMIDT DECOMPOSITION OF SPDC

The biphoton state generated in the SPDC process can be decomposed into a superposition of the tensor product of two linear combinations of Hermite-Gauss modes [Eq. (B1)],

$$|\Psi\rangle = \sum_{m,n}\sum_{m',n'} C_{mn}^{m'n'}\,|m,n\rangle_s \otimes \left|m',n'\right\rangle_i. \tag{B1}$$

Hermite-Gauss $\mathcal{HG}$ modes $|m,n\rangle = |m\rangle\otimes|n\rangle$ form an orthonormal basis of spatial modes for the transverse plane and have the following expressions (2D and 1D, respectively) in adimensional coordinates:

$$\langle x_o,y_o|\,m,n\rangle = \frac{1}{\sqrt{2^m 2^n m!\,n!\,\pi}}\mathcal{H}_m(x_o)e^{-x_o^2/2}\otimes\mathcal{H}_n(y_o)e^{-y_o^2/2}, \tag{B2}$$

$$\langle x_o|\,m\rangle = \frac{1}{\sqrt{2^m m!\,\sqrt{\pi}}}\mathcal{H}_m(x_o)e^{-x_o^2/2}. \tag{B3}$$

Here $\mathcal{H}_i(x_k)$ is the ith-order Hermite polynomial for variable x_k, and $x_o = \sqrt{2}x/\sigma_s$ and $y_o = \sqrt{2}y/\sigma_s$, as defined in the main text. When expressed in the Schmidt basis of Hermite Gauss $\mathcal{HG}$ modes, the original SPDC state can be simplified to [24,26,28]

$$|\Psi\rangle = \sum_{m,n} C_{mn}\,|m,n\rangle_s\otimes|m,n\rangle_i\,, \tag{B4}$$

where

$$C_{mn} = \frac{4\gamma}{(1+\gamma)^2}\left|\frac{1-\gamma}{1+\gamma}\right|^{(m+n)}$$

and γ is a constant determined by source parameters such as the crystal length and pump beam waist. When performing any sort of joint measurement (i.e., coincidence counts or coincidence imaging) on the entangled state, we consider a PSF of the form of the biphoton expression given in Eq. (B4). If a separation is introduced in the signal beam, it becomes a mixed state of two separated beams with the signal photon displaced in the x_s axis. The two-photon density matrix $\rho_{\rm BI}$ resembles Eq. (A5), with $\langle x_s|\,m^{\pm}\rangle_s = \sqrt{1/(2^m m!\,\sqrt{\pi})}\,\mathcal{H}_m(x_s\pm s)e^{-(x_s\pm s)^2/2}$:

$$\rho_{\rm BI} = \sum_{m,n}\sum_{u,v} C_{mn}C_{uv}^{*}\,|m,n\rangle_i\ {}_i\langle u,v|\otimes[|m^+,n\rangle_s\ {}_s\langle u^+,v| + |m^-,n\rangle_s\ {}_s\langle u^-,v|]. \tag{B5}$$

The derivative of the PSF [Eq. (B4)] in x_s has the form

$$|\Psi\rangle^{(1)} = \sum_{m,n} C_{mn}\,|m\rangle_s^{(1)}\,|n\rangle_s\otimes|m,n\rangle_i\,,$$

where we can find from the recurrence relations of the Hermite polynomials that

$$|m\rangle_s^{(1)} = \sqrt{\frac{m}{2}}\,|m-1\rangle_s - \sqrt{\frac{m+1}{2}}\,|m+1\rangle_s\,. \tag{B6}$$

So, the derivative becomes a maximally entangled state with the expression

$$|\Psi\rangle^{(1)} = \sum_{m,n} C_{m,n}\left(\sqrt{\frac{m}{2}}\,|m-1\rangle_s - \sqrt{\frac{m+1}{2}}\,|m+1\rangle_s\right)|n\rangle_s \otimes|m,n\rangle_i\,. \tag{B7}$$

Projecting onto such a state is not trivial and is outside the scope of this experiment. We instead chose to use measurements readily available to us experimentally in a setup with entangled photon pairs. A variety of measurements (either categorized as joint or single-photon measurements) are possible that will determine the projection outcomes $\mathcal{P}_i$. Using a joint basis of $\mathcal{HG}$ modes as the mode sorting basis, with elements $|k,l\rangle_s\,\langle k,l|_s\otimes\left|k',l'\right\rangle_i\left\langle k',l'\right|_i$, the projection outcomes $\mathcal{P}_{kl}^{k'l'}$ can be expressed as

$$\begin{aligned}\mathcal{P}_{kl}^{k',l'} &= {\rm Tr}[|k,l\rangle_s\,\langle k,l|_s\otimes\left|k',l'\right\rangle_i\left\langle k',l'\right|_i\,\rho_{\rm BI}]\\ &= \langle k,l|_s\otimes\left\langle k',l'\right|_i\rho_{\rm BI}\,|k,l\rangle_s\otimes\left|k',l'\right\rangle_i\\ &= \tfrac{1}{2}C_{k',l}^2\{|\langle k\left|k'^{+}\right\rangle|^2 + |\langle k\left|k'^{-}\right\rangle|^2\}\delta_{l,l'}.\end{aligned} \tag{B8}$$

APPENDIX C: ANALYTICAL EXPANSION OF $\langle m|\, n^{\pm}\rangle$

The inner product between an $\mathcal{HG}$ function of mode m and a displaced $\mathcal{HG}$ function of mode n can be written as

$$\langle m|\, n^{\pm}\rangle = \int_{-\infty}^{+\infty} \mathcal{HG}_m(x)\mathcal{HG}_n(x \pm s)dx.$$

Applying a change of variables $u = x \pm s/2$ and inserting the expressions into Eq. (B3), we obtain

$$\begin{aligned}\langle m|\, n^{\pm}\rangle &= \frac{1}{\sqrt{2^m 2^n m!\, n!\, \pi}} \int_{-\infty}^{+\infty} e^{-(1/2)[(u\mp s/2)^2+(u\pm s/2)^2]} \\ &\quad \mathcal{H}_m\left(u \mp \frac{s}{2}\right)\mathcal{H}_n\left(u \pm \frac{s}{2}\right)du \\ &= \frac{e^{-s^2/4}}{\sqrt{2^{m+n} m! n! \pi}} \int_{-\infty}^{+\infty} e^{-x^2} \\ &\quad \mathcal{H}_m\left(u \mp \frac{s}{2}\right)\mathcal{H}_n\left(u \pm \frac{s}{2}\right)du. \end{aligned} \tag{C1}$$

The integral in Eq. (C1) is given in a table of integrals [35], where, for $n \geq m$,

$$\begin{aligned}&\int_{-\infty}^{+\infty} e^{-x^2}\mathcal{H}_m(x+y)\mathcal{H}_n(x+z)dx \\ &\quad = 2^n \pi\, m!\, z^{n-m}\mathcal{L}_m^{n-m}(-2yz)\end{aligned} \tag{C2}$$

with $\mathcal{L}_i^{\alpha}$ the αth generalized Laguerre α polynomial of order i, α. So, the analytical expression for the inner product for $n \geq m$ is

$$\langle m|\, n^{\pm}\rangle = \sqrt{\frac{m!}{n!}} 2^{(m-n)/2}(\pm s)^{n-m}e^{-s^2/4}\mathcal{L}_m^{n-m}\left(\frac{s^2}{2}\right). \tag{C3}$$

APPENDIX D: BIPHOTON SPADE BASED ON PROJECTION ONTO HG MODES

Here, we derive the main result showing the relation between the Fisher information and the Schmidt rank (K) in biphoton SPADE. In the small separation limit [using Eqs. (A4) and (B6)] only three terms in Eq. (B8) are nonzero:

$$\begin{aligned}\mathcal{P}_{kl}^{k'l'} &\approx C_{k',l}^2\Bigg[\delta_{k,k'}^2\left\{1 - \frac{s^2}{2}(2k'+1)\right\} \\ &\quad + \delta_{k,k'-1}^2\frac{k'}{2} + \delta_{k,k'+1}^2\frac{k'+1}{2}\Bigg]\delta_{l,l'}^2,\end{aligned} \tag{D1}$$

$$\begin{aligned}\mathcal{P}_{kl}^{kl} \approx C_{k,l}^2\left(1 - \frac{s^2}{2}(2k+1)\right), \quad \mathcal{P}_{kl}^{k+1,l} \approx s^2 C_{k+1,l}^2\frac{k+1}{2}, \\ \mathcal{P}_{kl}^{k-1,l} \approx s^2 C_{k-1,l}^2\frac{k}{2}.\end{aligned} \tag{D2}$$

For $k = k'$, the $\mathcal{FI}$ about the parameter $\delta = 2s$ tends to 0. For $k = k' \pm 1$, the projection outcome has the same form as for optimal measurements, where $\mathcal{P}_i$ is proportional to δ^2:

$$\mathcal{FI}_{kl}^{kl}(s) \approx \frac{\left[C_{k,l}^2(2k+1)s\right]^2}{4 - 2s^2(2k+1)} \to 0, \tag{D3a}$$

$$\mathcal{FI}_{kl}^{k+1,l} \approx \frac{k+1}{2}C_{k+1,l}^2, \tag{D3b}$$

$$\mathcal{FI}_{kl}^{k-1,l} \approx \frac{k}{2}C_{k-1,l}^2. \tag{D3c}$$

For example, projecting the signal photon onto $|1,0\rangle_s$ and coupling the idler photon into a single-mode fiber (projection onto $|0,0\rangle_i$) would give a constant Fisher information, for small separations, of $\frac{1}{2}C_{0,0}^2$. The total $\mathcal{FI}$ is obtained by summing the nonvanishing $\mathcal{FI}$ across all HG mode measurements. Writing out the coefficients explicitly,

$$\begin{aligned}\mathcal{FI}_{kl}^{k+1,l} &\approx \frac{k+1}{2}C_{0,0}^2\left(\frac{1-\gamma}{1+\gamma}\right)^{2(k+1)}\left(\frac{1-\gamma}{1+\gamma}\right)^{2l}, \\ \mathcal{FI}_{kl}^{k-1,l} &\approx \frac{1}{2}kC_{0,0}^2\left(\frac{1-\gamma}{1+\gamma}\right)^{2(k-1)}\left(\frac{1-\gamma}{1+\gamma}\right)^{2l},\end{aligned}$$

and using

$$\begin{aligned}\sum_k k\left(\frac{1-\gamma}{1+\gamma}\right)^{2k} &= \frac{(1-\gamma)^2(1+\gamma)^2}{16\gamma^2}, \\ \sum_k \left(\frac{1-\gamma}{1+\gamma}\right)^{2k} &= \frac{(1+\gamma)^2}{4\gamma},\end{aligned}$$

we can calculate the sum over k for the 1D case,

$$\sum_k \mathcal{FI}_{kl}^{k+1,l} = \frac{1}{2}\left(\frac{1-\gamma}{1+\gamma}\right)^2 \approx 0.27, \tag{D4a}$$

$$\sum_k \mathcal{FI}_{kl}^{k-1,l} = \frac{1}{2}, \tag{D4b}$$

or the sum over all k, l,

$$\sum_{k,l} \mathcal{FI}_{kl}^{k+1,l} = \frac{(1-\gamma)^2}{8\gamma} \approx 0.60, \tag{D5a}$$

$$\sum_{k,l} \mathcal{FI}_{kl}^{k-1,l} = \frac{(1+\gamma)^2}{8\gamma} \approx 1.10. \tag{D5b}$$

The numerical values correspond to the Fisher information value for $\gamma = 0.15$, as in the experiment. Note that, for strong spatial correlations, the value of γ gets closer to 0 and the total Fisher information increases. In fact, the Schmidt number $K = (\gamma + \gamma^{-1})^2/4$, which is often used as a measure to describe the strength of spatial entanglement in the SPDC pair, can be found in the total Fisher information sum:

$$\sum_{k,l} \mathcal{FI}_{\text{coinc}} = \frac{1}{4}(\gamma + \gamma^{-1}) = \frac{1}{2}\sqrt{K} \geq \frac{1}{2}. \qquad \text{(D6)}$$

APPENDIX E: GAUSSIAN CASE ($\gamma = 1$)

Note that $\gamma = 1$ corresponds to a simple separable product state of a two Gaussian wave functions for the signal and idler. In that case, the total Fisher information according to Eq. (D6) reduces to $\frac{1}{2}(N/\sigma_s^2)$, which can be briefly seen as follows. The state after displacement can be represented by a density matrix $\rho = \frac{1}{2}[|0^+0\rangle\langle 0^+0| + |0^-0\rangle\langle 0^-0|]$. At the small separation regime the optimal mode of the projection is the first-order Hermite-Gauss mode $\mathcal{HG}_{01}$, for which the probability for a successful projection is given by

$$P_1 = \langle 10|\,\rho\,|10\rangle = \tfrac{1}{2}[|\langle 1|\,0^+\rangle|^2 + |\langle 1|\,0^-\rangle|^2].$$

Using Eq. (C3), we have $\langle 1|\,0^+\rangle = \langle 1^-|\,0\rangle = -\sqrt{1/2}\, se^{-s^2/4}$ and $\langle 1|\,0^-\rangle = \langle 1^+|\,0\rangle = \sqrt{1/2}\, se^{-s^2/4}$. The probability outcome P_1 is given by

$$P_1 = \tfrac{1}{2}s^2 e^{-s^2/2}$$

with Fisher information

$$\mathcal{FI}_1 = \frac{1}{P_1}\left(\frac{\partial P_1}{\partial(2s)}\right) = \frac{1}{4}\left(2 - 2s^2 + \frac{s^4}{2}\right)e^{-s^2/2} \approx \frac{1}{2}\left(\frac{N}{\sigma_s^2}\right).$$

The total Fisher information for the simple Gaussian case does indeed correspond to the total Fisher information when $\gamma = 1$. The entanglement scheme thus provides an advantage over classical SPADE for any level of entanglement with $\gamma < 1$.

[1] L. Rayleigh, XXXI. Investigations in optics, with special reference to the spectroscope, The London, Edinburgh, and Dublin, Philos. Mag. J. Sci. **8**, 261 (1879).

[2] E. Ash and G. Nicholls, Super-resolution aperture scanning microscope, Nature **237**, 510 (1972).

[3] E. Betzig and J. K. Trautman, Near-field optics: Microscopy, spectroscopy, and surface modification beyond the diffraction limit, Science **257**, 189 (1992).

[4] M. Von Ardenne, Das elektronen-rastermikroskop, Z. Phys. **109**, 553 (1938).

[5] J. Tersoff and D. R. Hamann, Theory and Application for the Scanning Tunneling Microscope, Phys. Rev. Lett. **50**, 1998 (1983).

[6] M. Tsang, R. Nair, and X.-M. Lu, Quantum Theory of Superresolution for Two Incoherent Optical Point Sources, Phys. Rev. X **6**, 031033 (2016).

[7] R. Kerviche, S. Guha, and A. Ashok, in *2017 IEEE International Symposium on Information Theory (ISIT)* (IEEE, Aachen, Germany, 2017), p. 441.

[8] M. Paúr, B. Stoklasa, Z. Hradil, L. L. Sánchez-Soto, and J. Rehacek, Achieving the ultimate optical resolution, Optica **3**, 1144 (2016).

[9] P. Boucher, C. Fabre, G. Labroille, and N. Treps, Spatial optical mode demultiplexing as a practical tool for optimal transverse distance estimation, Optica **7**, 1621 (2020).

[10] W.-K. Tham, H. Ferretti, and A. M. Steinberg, Beating Rayleigh's Curse by Imaging Using Phase Information, Phys. Rev. Lett. **118**, 070801 (2017).

[11] Z. Hradil, J. Řeháček, L. Sánchez-Soto, and B.-G. Englert, Quantum Fisher information with coherence, Optica **6**, 1437 (2019).

[12] K. Liang, S. A. Wadood, and A. Vamivakas, Coherence effects on estimating two-point separation, Optica **8**, 243 (2021).

[13] S. Kurdzialek, Back to sources—The role of losses and coherence in super-resolution imaging revisited, Quantum **6**, 697 (2022).

[14] M. Gessner, C. Fabre, and N. Treps, Superresolution Limits from Measurement Crosstalk, Phys. Rev. Lett. **125**, 100501 (2020).

[15] Y. L. Len, C. Datta, M. Parniak, and K. Banaszek, Resolution limits of spatial mode demultiplexing with noisy detection, Int. J. Quantum Inf. **18**, 1941015 (2020).

[16] J. Yang, S. Pang, Y. Zhou, and A. N. Jordan, Optimal measurements for quantum multiparameter estimation with general states, Phys. Rev. A **100**, 032104 (2019).

[17] S. Zhou and L. Jiang, Modern description of Rayleigh's criterion, Phys. Rev. A **99**, 013808 (2019).

[18] K. K. Bearne, Y. Zhou, B. Braverman, J. Yang, S. Wadood, A. N. Jordan, A. Vamivakas, Z. Shi, and R. W. Boyd, Confocal super-resolution microscopy based on a spatial mode sorter, Opt. Express **29**, 11784 (2021).

[19] A. Pushkina, G. Maltese, J. Costa-Filho, P. Patel, and A. Lvovsky, Superresolution Linear Optical Imaging in the Far Field, Phys. Rev. Lett. **127**, 253602 (2021).

[20] D. Sych, V. Averchenko, and G. Leuchs, Generic method for lossless generation of arbitrarily shaped photons, Phys. Rev. A **96**, 053847 (2017).

[21] E. Polino, M. Valeri, N. Spagnolo, and F. Sciarrino, Photonic quantum metrology, AVS Quantum Sci. **2**, 024703 (2020).

[22] V. Giovannetti, S. Lloyd, and L. Maccone, Advances in quantum metrology, Nat. Photonics **5**, 222 (2011).

[23] C. W. Helstrom, Quantum detection and estimation theory, J. Stat. Phys. **1**, 231 (1969).

[24] F. M. Miatto, H. di Lorenzo Pires, S. M. Barnett, and M. P. van Exter, Spatial Schmidt modes generated in parametric down-conversion, Eur. Phys. J. D **66**, 1 (2012).

[25] M. Fedorov, Y. M. Mikhailova, and P. Volkov, Gaussian modelling and Schmidt modes of SPDC biphoton states, J. Phys. B: At., Mol. Opt. Phys. **42**, 175503 (2009).

[26] F. M. Miatto, T. Brougham, and A. M. Yao, Cartesian and polar Schmidt bases for down-converted photons, Eur. Phys. J. D **66**, 1 (2012).

[27] G. S. Thekkadath, L. Giner, X. Ma, J. Flórez, and J. S. Lundeen, Projecting onto any two-photon polarization state using linear optics, New J. Phys. **20**, 083033 (2018).

[28] S. Straupe, D. Ivanov, A. Kalinkin, I. Bobrov, and S. Kulik, Angular Schmidt modes in spontaneous parametric down-conversion, Phys. Rev. A **83**, 060302 (2011).

[29] E. Bolduc, N. Bent, E. Santamato, E. Karimi, and R. W. Boyd, Exact solution to simultaneous intensity and phase encryption with a single phase-only hologram, Opt. Lett. **38**, 3546 (2013).

[30] F. Bouchard, N. H. Valencia, F. Brandt, R. Fickler, M. Huber, and M. Malik, Measuring azimuthal and radial modes of photons, Opt. Express **26**, 31925 (2018).

[31] N. K. Fontaine, R. Ryf, H. Chen, D. T. Neilson, K. Kim, and J. Carpenter, Laguerre-Gaussian mode sorter, Nat. Commun. **10**, 1 (2019).

[32] F. Troiani, E. Rotunno, S. Frabboni, R. B. Ravelli, P. J. Peters, E. Karimi, and V. Grillo, Efficient molecule discrimination in electron microscopy through an optimized orbital angular momentum sorter, Phys. Rev. A **102**, 043510 (2020).

[33] S. Meier, J. Heimerl, and P. Hommelhoff, Few-electron correlations after ultrafast photoemission from nanometric needle tips, Nat. Phys., 1 (2023).

[34] R. Haindl, A. Feist, T. Domröse, M. Möller, J. H. Gaida, S. V. Yalunin, and C. Ropers, Coulomb-correlated electron number states in a transmission electron microscope beam, Nat. Phys., 1 (2023).

[35] I. S. Gradshteyn and I. M. Ryzhik, *Table of Integrals, Series, and Products* (Academic Press, San Diego, CA, 2014).

Chapter 3

High Dimensional Quantum Information and Simulation

This chapter is based on the following articles:

1. **Paneru, D.**, Di Colandrea, F., D'Errico, A., & Karimi, E. (2025). Nonlocal transfer of high-dimensional unitary operations. *Quantum* **9**, 1855.

   DOI: `https://doi.org/10.22331/q-2025-09-11-1855`

2. Gao, X., **Paneru, D.**, Di Colandrea, F., Zhang, Y., & Karimi, E. (2025). Generation of the Complete Bell Basis via Hong-Ou-Mandel Interference. *Physical Review A* **112**, 012215.

   DOI: `https://doi.org/10.1103/dcxb-ql1r`

3. Di Colandrea, F., Jaouni, T., Grace, J., **Paneru, D.**, Arienzo, M., D'Errico, A., & Karimi, E. (2025). Engineering qubit dynamics in open systems with photonic synthetic lattices. *Physical Review Research* **7**, 023236.

   DOI: `https://doi.org/10.1103/PhysRevResearch.7.023236`

3.1 Spatial Correlations in SPDC

Much of the background on the biphoton wavefunction produced in the parametric down conversion process has been covered in Section 2.5. As we mentioned previously, photons produced in parametric down conversion are highly correlated in position degree of freedom, and anti-correlated in the momentum degree of freedom. The biphoton wavefunction generated from Type-I degenerate SPDC from thin crystals can be expressed as,

$$|\psi\rangle = \mathcal{C} \int \mathrm{d}\mathbf{k} \; |\mathbf{k}\rangle_s \, |-\mathbf{k}\rangle_i \,, \tag{3.1}$$

where $\mathbf{k}$ is the transverse momentum, $\mathcal{C}$ a normalization factor, and s and i refer to signal and idler photon, respectively. Equation (3.1) expresses the momentum conservation for the SPDC process and assumes a plane-wave pump with a fairly large extent. The correlation in momentum is in principle of a really high dimension, and one can quantize such momentum in finite momentum step sizes and use them for finite-dimensional computing.

3.2 Hong-Ou-Mandel effect

The two-photon interference effect [15], most commonly referred to as the Hong-Ou-Mandel (HOM) effect, is a truly quantum effect where two indistinguishable photons interfere at the input of a beam splitter and exit the output ports together, a phenomenon known as "bunching" [15, 76]. A 50:50 lossless beam splitter mixes two input modes a and b into two output modes c and d, with the annhilation operators transformed as,

$$\hat{c} = \frac{1}{\sqrt{2}}(\hat{a} + \hat{b}), \qquad \hat{d} = \frac{1}{\sqrt{2}}(\hat{a} - \hat{b}).$$

Accordingly, the creation operators transform as:

$$\hat{a}^\dagger = \frac{1}{\sqrt{2}}(\hat{c}^\dagger + \hat{d}^\dagger), \qquad \hat{b}^\dagger = \frac{1}{\sqrt{2}}(\hat{c}^\dagger - \hat{d}^\dagger).$$

We consider an input state with two identical photons, with one photon in each input mode:

$$|\psi_{\text{in}}\rangle = \hat{a}^\dagger \hat{b}^\dagger \, |0\rangle \,.$$

Now applying the beam-splitter transformations:

$$\begin{aligned}
|\psi_{\text{out}}\rangle &= \left(\frac{1}{\sqrt{2}}(\hat{c}^\dagger + \hat{d}^\dagger)\right)\left(\frac{1}{\sqrt{2}}(\hat{c}^\dagger - \hat{d}^\dagger)\right)|0\rangle \\
&= \frac{1}{2}\left[\hat{c}^{\dagger 2} - \hat{c}^\dagger \hat{d}^\dagger + \hat{d}^\dagger \hat{c}^\dagger - \hat{d}^{\dagger 2}\right]|0\rangle \\
&= \frac{1}{2}\left[\hat{c}^{\dagger 2} - \hat{d}^{\dagger 2}\right]|0\rangle \\
&= \frac{1}{\sqrt{2}}\left(|2\rangle_c |0\rangle_d - |0\rangle_c |2\rangle_d\right).
\end{aligned}$$

Notice that the terms $\hat{c}^\dagger \hat{d}^\dagger$, and $\hat{d}^\dagger \hat{c}^\dagger$ cancel each other, meaning there is zero probability of detecting one photon in each output mode. This destructive interference is the hallmark of the Hong–Ou–Mandel effect, and gives rise to the famous Hong-Ou-Mandel dip when measuring coincidences between the two output ports. The visibility (V) of the dip is defined as,

$$V = \frac{C_{\max} - C_{\min}}{C_{\max}},$$

where $C_{\max}$ and $C_{\min}$ are respectively the maximum and minimum coincidences between the output arms. The visibility approaches one for perfectly indistinguishable photons.

3.3 Bell States

Bell states are the four maximally entangled states in the two-dimensional Hilbert space $\mathcal{H}_2 \otimes \mathcal{H}_2$, which form a complete orthonormal basis. Historically, they have been integral to the study of quantum foundations, depicting stark departures of quantum mechanics from the classical world (for example: the EPR state [6]) while also playing a vital role in quantum information science, some applications of which include quantum superdense coding [77], quantum communication and teleportation, quantum information processing, and the fundamental studies of quantum nonlocality. The four Bell states written in the polarization basis $\{|H\rangle, |V\rangle\}$ are,

$$\begin{aligned}
|\phi^{\pm}\rangle &= \frac{1}{\sqrt{2}}\left(|H\rangle_A |H\rangle_B \pm |V\rangle_A |V\rangle_B\right), \\
|\psi^{\pm}\rangle &= \frac{1}{\sqrt{2}}\left(|H\rangle_A |V\rangle_B \pm |V\rangle_A |H\rangle_B\right),
\end{aligned} \tag{3.2}$$

where the subscripts A and B represent the photon states for Alice and Bob, two spatially separated observers. These states are maximally entangled in that the reduced density matrix for either qubit is maximally mixed, i.e $\mathrm{Tr}_B(|\Phi^+\rangle\langle\Phi^+|) = \frac{I}{2}$. The state $|\psi^-\rangle$ which is the singlet state with the total spin of zero, is rotationally invariant. It remains in the same form under the application of the same local unitary to both of the qubits. Experimentally, Bell states have been generated using spontaneous parametric down-conversion (SPDC) in nonlinear crystals [78], trapped ions [79], superconducting qubits [80], and NV centers in diamond [81]. Verification of Bell states can be done through quantum state tomography by reconstructing the density matrix from measurements [82]. Bell states are integral to multiple quantum technologies such as quantum teleportation, where quantum states can be transmitted by using maximally entangled Bell states and classical communication [83], superdense coding [84], quantum key distribution (QKD), or entanglement swapping [85], and quantum error correction.

3.3.1 Generation of Bell States using a HOM beamsplitter

Bell states can also be generated upon postselection at the outputs of a beamsplitter. Consider, for instance, an input state with two photons but with orthogonal polarization,

$$|\psi_{\mathrm{in}}\rangle = \hat{a}_H^\dagger \hat{b}_V^\dagger |0\rangle ,$$

where $\hat{a}_H^\dagger$ is the creation operator for a photon in mode a with horizontal polarization (H), and $\hat{b}_V^\dagger$ is the creation operator for a photon in mode b with vertical polarization (V). As before, applying the beam-splitter transformations,

$$\begin{aligned} |\psi_{\mathrm{out}}\rangle &= \left(\frac{1}{\sqrt{2}}(\hat{c}_H^\dagger + \hat{d}_H^\dagger)\right)\left(\frac{1}{\sqrt{2}}(\hat{c}_V^\dagger - \hat{d}_V^\dagger)\right)|0\rangle \\ &= \frac{1}{2}\left[\hat{c}_H^\dagger \hat{c}_V^\dagger - \hat{c}_H^\dagger \hat{d}_V^\dagger + \hat{d}_H^\dagger \hat{c}_V^\dagger - \hat{d}_H^\dagger \hat{d}_V^\dagger\right]|0\rangle . \end{aligned}$$

Upon post selection on the coincident detection of photons in arms c and d, the state we obtain is,

$$\begin{aligned} |\psi_{\mathrm{c}}\rangle &= \frac{1}{\sqrt{2}}\left(-\hat{c}_H^\dagger \hat{d}_V^\dagger + \hat{d}_H^\dagger \hat{c}_V^\dagger\right)|0\rangle , \\ &= \frac{1}{\sqrt{2}}\left(-|H\rangle_C |V\rangle_D + |V\rangle_C |H\rangle_D\right), \end{aligned}$$

which is the $|\psi\rangle^-$ state with a minus sign in front. In one of our works [86] that follows, we show how we can generate all four Bell states by structuring the spatial mode and the polarization of the photons before the beamsplitter.

3.4 Quantum State Tomography

Quantum state tomography is the process of reconstructing the full quantum state of a system by performing a series of measurements on an ensemble of identically prepared systems. When the system under study is a state of a pair of entangled qubits, such as a Bell state, we use two-qubit quantum state tomography to characterize the density matrix.

3.4.1 Stokes Parameter Formalism

In quantum information, Stokes parameters describe the polarization state of a photon or the general state of a qubit. For a single qubit, the density matrix ρ can be written as:

$$\rho = \frac{1}{2}(I + \mathbf{r} \cdot \sigma).$$

where $\sigma = (\sigma_x, \sigma_y, \sigma_z)$ are the Pauli matrices,

$$\sigma_x = \begin{pmatrix} 0 & 1 \\ 1 & 0 \end{pmatrix}, \quad \sigma_y = \begin{pmatrix} 0 & -i \\ i & 0 \end{pmatrix}, \quad \sigma_z = \begin{pmatrix} 1 & 0 \\ 0 & -1 \end{pmatrix}.$$

and $\vec{r}$ is the Bloch vector, with components, $r_i = \mathrm{Tr}(\rho\sigma_i)$.

For two qubits, the density matrix can be expressed using a tensor product of Pauli matrices:

$$\rho = \frac{1}{4}\sum_{i,j=0}^{3} T_{ij}\, \sigma_i \otimes \sigma_j, \tag{3.3}$$

where $\sigma_0 = I$ and $\sigma_{1,2,3} = \sigma_{x,y,z}$. The parameters T_{ij} are called the generalized Stokes parameters,

$$T_{ij} = \mathrm{Tr}(\rho\, \sigma_i \otimes \sigma_j).$$

This representation contains 16 real parameters and completely characterizes any two-qubit density matrix. To determine the Stokes parameters T_{ij}, one can perform the joint measurements on both qubits in various bases corresponding to the Pauli operators. One measures all combinations $\sigma_i \otimes \sigma_j$ for $i, j \in \{0, x, y, z\}$ to extract the full set of Stokes parameters. Once the Stokes parameters T_{ij} are known, the density matrix is reconstructed via Equation 3.3. This matrix is Hermitian and has unit trace. In practice, due to noise in the data, sometimes the estimated matrix may not be physical (i.e., non trace preserving or positive semi-definite), so statistical estimation techniques like maximum likelihood estimation (MLE) are generally applied to obtain a valid density matrix.

3.4.2 Purity

In quantum mechanics, purity is a metric that quantifies how "mixed" a quantum state is. A pure state can be described by a single vector in the Hilbert space, while a mixed state is in a statistical combination of different possible pure states. Mathematically, the purity γ of a density matrix ρ is defined as,

$$\gamma = \mathrm{tr}[\rho^2],$$

where tr is the trace of the matrix. The more mixed the state is, the smaller the purity is. For a pure state, γ equals 1, while for mixed states it is less than 1, and in general it is bounded as $\frac{1}{d} \leq \gamma \leq 1$, where d is the dimension of the Hilbert space of the system.

The purity of the reduced density matrix of a composite system, also gives an idea about the correlations in the composite system. The more entangled the composite system, the less pure is the reduced state of the subsystems.

3.5 Qubit Noises and Kraus Operators

One of the challenges in quantum circuits is that qubits are inherently fragile and susceptible to noise and decoherence due to interactions with their environment. The Kraus operator formalism provides a general framework for describing noisy quantum operations. Suppose a quantum system is described by a density matrix ρ. A noisy evolution of this system under the influence of its environment can be represented as [87],

$$\rho' = \mathcal{E}(\rho) = \sum_k E_k \rho E_k^\dagger,$$

where $\{E_k\}$ are the Kraus operators associated with the quantum channel $\mathcal{E}$. These operators satisfy the completeness condition,

$$\sum_k E_k^\dagger E_k = I,$$

which ensures that the channel is trace-preserving. This operator-sum representation stems from a unitary evolution on a joint system-environment Hilbert space followed by a partial trace over the environment. That is, if the system and environment undergo a joint unitary evolution U_{SE}, with the environment starting in the pure state $|0\rangle_{env}$, then,

$$\mathcal{E}(\rho) = \mathrm{Tr}_E \left[U_{SE}(\rho \otimes |0\rangle_{env} \langle 0|) U_{SE}^\dagger \right],$$

and this map is always expressible in terms of Kraus operators.

There are several common noises that affect single qubits, each corresponding to a different physical process. One of the simplest is the bit flip channel, which mimics a classical bit flip between $|0\rangle$ and $|1\rangle$. Its Kraus operators are given by:

$$E_0 = \sqrt{1-p}\, I, \quad E_1 = \sqrt{p}\, X,$$

where X is the Pauli-X matrix. The action of this channel is,

$$\mathcal{E}(\rho) = (1-p)\rho + pX\rho X.$$

This process randomly flips the qubit with probability p.

The phase flip channel alters the relative phase between $|0\rangle$ and $|1\rangle$, using the Pauli-Z operator,

$$E_0 = \sqrt{1-p}\, I, \quad E_1 = \sqrt{p} Z.$$

This results in,

$$\mathcal{E}(\rho) = (1-p)\rho + pZ\rho Z.$$

This channel is particularly relevant in systems experiencing dephasing due to environmental interactions.

The bit-phase flip channel, which applies the Pauli-Y operator, represents a simultaneous bit and phase error,

$$E_0 = \sqrt{1-p}\, I, \quad E_1 = \sqrt{p}\, Y,$$

with,

$$Y = \begin{bmatrix} 0 & -i \\ i & 0 \end{bmatrix}.$$

resulting in,

$$\mathcal{E}(\rho) = (1-p)\rho + pY\rho Y.$$

The depolarizing channel models isotropic noise where the qubit is replaced by a completely mixed state with probability p. After passing through a depolarizing channel, the quantum state of a qubit becomes,

$$\mathcal{E} = \frac{pI}{2} + (1-p)\rho. \tag{3.4}$$

. Its Kraus operators are,

$$E_0 = \sqrt{1-p}\, I, \quad E_1 = \sqrt{\frac{p}{3}}\, X, \quad E_2 = \sqrt{\frac{p}{3}}\, Y, \quad E_3 = \sqrt{\frac{p}{3}}\, Z.$$

This yields,

$$\mathcal{E}(\rho) = (1-p)\rho + \frac{p}{3}(X\rho X + Y\rho Y + Z\rho Z).$$

One can see the equivalence of this form from the fact that for arbitrary ρ,

$$\frac{I}{2} = \frac{\rho + X\rho X + Y\rho Y + Z\rho Z}{4}. \tag{3.5}$$

Similarly, there are the other two noises, i.e. amplitude damping, which can represent energy relaxation processes such as spontaneous emission, and phase damping, which models loss of coherence without energy dissipation. The Kraus operators for the amplitude damping channel are,

$$E_0 = \begin{bmatrix} 1 & 0 \\ 0 & \sqrt{1-\gamma} \end{bmatrix}, \quad E_1 = \begin{bmatrix} 0 & \sqrt{\gamma} \\ 0 & 0 \end{bmatrix},$$

which transform the density matrix as,

$$\mathcal{E}(\rho) = E_0 \rho E_0^\dagger + E_1 \rho E_1^\dagger.$$

This models a decay from the excited state $|1\rangle$ to the ground state $|0\rangle$ with probability γ.

Similarly, the Kraus operators for the phase damping channel are,

$$E_0 = \begin{bmatrix} 1 & 0 \\ 0 & \sqrt{1-\lambda} \end{bmatrix}, \quad E_1 = \begin{bmatrix} 0 & 0 \\ 0 & \sqrt{\lambda} \end{bmatrix}.$$

Phase damping destroys the off-diagonal terms (or the coherence) without altering the populations.

3.6 Research Summary

The rest of the chapter presents three research articles in the areas of quantum Information. The first work [88] presents a protocol for transferring high-dimensional unitary operators between two photons using spatial correlations. This work can potentially find applications in a quantum computing network where resource sharing in the form of computational access to a high-dimensional photonic quantum computer is desired. The second work [86] is on the generation of spatially structured Bell states by using Hong-Ou-Mandel interference on the structured photons. As we discussed, the integral role Bell states play in quantum information has potential applicability in works where spatially structured generation of Bell states is desired. In the last article [89], we present the work on simulation of arbitrary noise operations using patterned liquid crystal meta-surfaces. We also experimentally implement the method for phase errors and depolarization.

Nonlocal transfer of high-dimensional unitary operations

Dilip Paneru,[1] Francesco Di Colandrea,[1,2,*] Alessio D'Errico,[1,3] and Ebrahim Karimi[1,3,4]

[1] *Nexus for Quantum Technologies, University of Ottawa, K1N 5N6, Ottawa, ON, Canada*
[2] *Dipartimento di Fisica, Università degli Studi di Napoli Federico II, Complesso Universitario di Monte Sant'Angelo, Via Cintia, 80126 Napoli, Italy*
[3] *National Research Council of Canada, 100 Sussex Drive, Ottawa ON Canada, K1A 0R6*
[4] *Institute for Quantum Studies, Chapman University, Orange, California 92866, USA*

Highly correlated biphoton states are powerful resources in quantum optics, both for fundamental tests of the theory and practical applications. In particular, high-dimensional spatial correlation has been used in several quantum information processing and sensing tasks, for instance, in ghost imaging experiments along with several quantum key distribution protocols. Here, we introduce a technique that exploits spatial correlations, whereby one can nonlocally access the result of an arbitrary unitary operator on an arbitrary input state without the need to perform any operation themselves. The method is experimentally validated on a set of spatially periodic unitary operations in one-dimensional and two-dimensional spaces. Our findings pave the way for efficiently distributing quantum simulations and computations in future instances of quantum networks where users with limited resources can nonlocally access the results of complex unitary transformations via a centrally located quantum processor.

INTRODUCTION

Quantum entanglement [1, 2], one of the central concepts of quantum mechanics, has led to fundamental modifications to our understanding of the physical world [3, 4], along with exciting technological developments in computation [5], metrology [6, 7], and communication [8, 9]. One of the most widely used techniques to generate entangled photon pairs exploits a nonlinear process known as spontaneous parametric down-conversion (SPDC) [10], whereby the emitted photons can be highly correlated in polarization, frequency, and spatial degrees of freedom [11]. Down-converted photon pairs have been employed as a source of polarization entanglement for fundamental tests of nonlocality [12], in quantum teleportation [13], and communication protocols [9]. The high-dimensional correlation in the position degree of freedom (and the corresponding anti-correlation in the momentum space) can be exploited in several quantum imaging experiments [14], such as quantum ghost imaging [15] and biphoton holography [16, 17].

When two parties share entangled particles, either can exploit the quantum correlations to nonlocally affect the quantum state of the other—for instance, through local measurements—a technique also referred to as quantum steering [18–20]. This concept was originally proposed and demonstrated for two photons entangled in the polarization degree of freedom, i.e., two photonic qubits [21]. However, the extension to high-dimensional entangled states unlocks remarkable advantages for quantum information protocols, in particular a higher information capacity and increased noise tolerance [22]. The first experimental demonstration of high-dimensional steering was reported in Ref. [23] with photons entangled in the discretized position-momentum degree of freedom [24], up to 31 dimensions.

Entanglement also enables the implementation of teleportation-based quantum computation, also known as gate teleportation [25], consisting of applying a quantum gate to an entangled state and then teleporting the target state through it [26]. This concept has been thoroughly investigated theoretically [27, 28] and demonstrated experimentally for qubit systems [29–32]. Recently, schemes to extend the technique to higher-dimensional (qudit) systems have also been proposed [33].

In this paper, we show how the inherent high degree of spatial correlations between photon pairs can be exploited to also obtain a protocol for transferring the output of a unitary operation performed on one of the photons (signal) to the second (idler). Experimentally, the optical transformation is implemented via a Spatial Light Modulator (SLM) encoding several phase masks. In combination with a multimode fiber, a similar setup has recently been adopted as a programmable photonic circuit processing spatial modes [34], with the outcome of the transformed photon revealed via projective measurements performed on the correlated one. In our experiment, the masks are generated as superpositions of sinusoidal gratings that mimic the result of lattice dynamics on optical modes that carry a quantized amount of transverse momentum, recently introduced for the simulation of discrete-time quantum walk dynamics [35, 36]. Our method is validated on a set of unitary operations coupling single input modes into multiple output modes, in both one-dimensional (1D) and two-dimensional (2D) configurations. In the 1D realization, a practical method for engineering the simulation transfer for different state preparations is also illustrated.

The versatility and robustness of the protocol suggest its employment in a photonic quantum network where computational capabilities are centralized. In such a framework, we envision a party with access to a quantum simulator that can perform the required operations, while remote clients without direct access to the platform can securely retrieve the simulation output. This approach paves the way for alternative implementations of blind quantum computation [37], as well as for distributing quantum simulations across different nodes of quantum networks [38], ultimately enabling resource-efficient and scalable quantum computing solutions.

THEORY

The biphoton wavefunction generated from Type-I degenerate SPDC from thin crystals can be expressed as

$$|\psi\rangle = \mathcal{C}\int \mathrm{d}\mathbf{k}\ |\mathbf{k}\rangle_s\,|-\mathbf{k}\rangle_i\,, \tag{1}$$

where $\mathbf{k}$ is the transverse momentum, C a normalization factor, and s and i refer to signal and idler photon, respectively. Equation (1) expresses the momentum conservation for the SPDC process and assumes a plane-wave pump.

We aim to define a scheme to transfer the result of a unitary transformation $\hat{U}$, acting only on the signal photon, to the idler photon. In the following, we show that this can be achieved by successive application of a different unitary operation and a projective measurement on the signal. The action of $\hat{U}$ on a momentum state $|\mathbf{k}\rangle$ is defined as

$$\hat{U}\,|\mathbf{k}\rangle = \int \mathrm{d}\mathbf{k}'\,U(\mathbf{k}',\mathbf{k})\,|\mathbf{k}'\rangle\,. \tag{2}$$

Our protocol for successfully transferring this operation from the *signal* to the *idler* photons relies on applying a different unitary $\hat{U}'_s$ to the signal photon, followed by a suitable projection. This allows us to access the result of the unitary operator on any input state on the idler side, without performing any operation on the idler photons. The construction of $\hat{U}'_s$ and the required projective measurement are explained in further detail below. Assume we want to transfer the result of $\hat{U}$ on a single input mode $|\phi_0\rangle = |\mathbf{k}_0\rangle$. Upon applying the unitary $\hat{U}'_s$ to the signal photon, the biphoton state is transformed to

$$\begin{aligned}|\psi'\rangle &= \hat{U}'_s\otimes\hat{I}\,|\psi\rangle \\ &= \iint \mathrm{d}\mathbf{k}'\mathrm{d}\mathbf{k}\,U'_s(\mathbf{k}',\mathbf{k})\,|-\mathbf{k}\rangle_i\,|\mathbf{k}'\rangle_s\,,\end{aligned} \tag{3}$$

where $\hat{I}$ is the identity operator in the idler basis. If a projection $\Pi_{\mathbf{k}'_0}$ on $|\mathbf{k}'_0\rangle_s$ is performed, the state of the idler photon is transformed according to

$$\begin{aligned}|\phi\rangle_i &= \int \mathrm{d}\mathbf{k}'\left(\int \mathrm{d}\mathbf{k}\,U'_s(\mathbf{k}',\mathbf{k})\,|-\mathbf{k}\rangle_i\right)\langle\mathbf{k}'_0|\,\mathbf{k}'\rangle_s \\ &= \int \mathrm{d}\mathbf{k}\,U'_s(\mathbf{k}'_0,-\mathbf{k})\,|\mathbf{k}\rangle_i\,,\end{aligned} \tag{4}$$

where we used $\langle\mathbf{k}'_0|\,\mathbf{k}'\rangle = \delta(\mathbf{k}'_0-\mathbf{k}')$, with $\delta(\mathbf{x})$ the Dirac delta function. By comparing the final result with Eq. (2), one obtains that the target unitary operator $\hat{U}'_s$ can be constructed as

$$U'_s(\mathbf{k}',\mathbf{k}) = U(-\mathbf{k},\mathbf{k}'), \tag{5}$$

and the result for a localized input state $|\mathbf{k}_0\rangle$ can be accessed simply by projecting on $|\mathbf{k}'_0\rangle = |\mathbf{k}_0\rangle$.

For the more general case of transferring the result of a unitary operation on an arbitrary initial state, which generally includes a superposition of modes, one can still apply a carefully chosen unitary operator $\hat{U}'$ to the signal photon, followed by a projection on a suitable state $|\chi\rangle_s$. The generalization is demonstrated in the following. A general input state can be written as

$$|\phi_0\rangle_i = \int \mathrm{d}\mathbf{k}'\,C(\mathbf{k}')\,|\mathbf{k}'\rangle_i\,, \tag{6}$$

where $C(\mathbf{k}')$ is the coefficient of the momentum mode $|\mathbf{k}'\rangle_i$. The result of the unitary operator on such an initial state can be written as

$$\hat{U}\,|\phi_0\rangle = \int d\mathbf{k}\left(\int d\mathbf{k}'C(\mathbf{k}')U(\mathbf{k},\mathbf{k}')\right)|\mathbf{k}\rangle\,. \tag{7}$$

Let us also define the general state for projection $|\chi\rangle_s$ as

$$|\chi\rangle_s = \int d\mathbf{k}'\,A(\mathbf{k}')\,|\mathbf{k}'\rangle_s\,. \tag{8}$$

As in Eqs. (3) and (4), upon the application of the unitary $\hat{U}'_s$ to the signal photon and a projection on $|\chi\rangle$, the idler state transforms as

$$\begin{aligned}|\phi\rangle_i &= \int \mathrm{d}\mathbf{k}'\left(\int \mathrm{d}\mathbf{k}\,U'_s(\mathbf{k}',\mathbf{k})\,|-\mathbf{k}\rangle_i\right)\langle\chi|\,\mathbf{k}'\rangle_s \\ &= \int \mathrm{d}\mathbf{k}\left(\int \mathrm{d}\mathbf{k}'\,A^*(\mathbf{k}')U'_s(\mathbf{k}',-\mathbf{k})\right)|\mathbf{k}\rangle_i\,.\end{aligned}$$

By comparing the final result with Eq. (7), and fixing $\hat{U}'_s$ as in Eq. (5), we obtain the coefficients $A(\mathbf{k}')$ for the required projection:

$$\begin{aligned}A(\mathbf{k}') &= \left(\frac{C(\mathbf{k}')U(\mathbf{k},\mathbf{k}')}{U'_s(\mathbf{k}',-\mathbf{k})}\right)^* \\ &= C(\mathbf{k}')^*.\end{aligned} \tag{9}$$

Thus, if the idler party needs to simulate the action of $\hat{U}$ on an arbitrary input state $|\phi_0\rangle$ but has no access to any computational resource, the signal party can perform $\hat{U}'_s$, as prescribed by Eq. (5), followed by a projection on

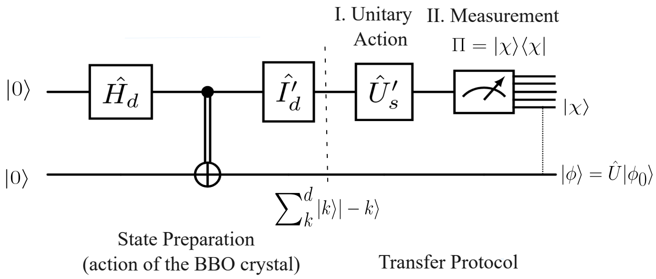

FIG. 1. **Quantum circuit of the nonlocal transfer.** The first part of the circuit represents the state preparation, which involves the application of a d-dimensional Hadamard operator, followed by a d-dimensional control X gate with an action $|j\rangle\,|k\rangle \rightarrow |k\rangle\,|(j+k)\,\mathrm{Mod}\ d\rangle$ followed by the d-dimensional Anti-Identity operator which creates the state $\sum_k |k\rangle\,|-k\rangle$. In our experiment, the action of the pump on the BBO crystal already prepares the desired state. The second part consists of the unitary action $\hat{U}_s$ on the signal photon, followed by a projective measurement Π. Upon successful projection, the desired unitary action $\hat{U}$ on the desired state $|\phi_0\rangle$ is obtained on the idler photon.

the state $|\chi\rangle_s$, whose coefficients are given by Eq. (9). In this way, the resource for the unitary operation remains centralized, but the results can be distributed across multiple parties in a network, effectively trading off high-dimensional correlations. We show the conceptual picture of the protocol in the form of a quantum circuit in Fig. 1.

For the purpose of experimental demonstration, we implement unitary transformations in the form of phase masks with an SLM. The chosen unitaries correspond to the simulation of lattice dynamics on optical modes carrying a quantized amount of transverse momentum, generated from the superpositions of sinusoidal gratings. Such operators act on the transverse momentum degree of freedom of the signal photon, adding quantized amounts of transverse momentum, $\Delta k_\perp = 2\pi/\Lambda$, where Λ is a characteristic distance. The action of $\hat{U}$ on a momentum state can therefore be expressed as

$$\hat{U}\,|k\rangle_s = \sum_m u_{m,k}\,|m_k\rangle_s\,, \tag{10}$$

where $|m_k\rangle = |k + k_m\rangle$, with $k_m = m\Delta k_\perp$ and m an integer number. If translation invariance is assumed, then $u_{m,k} = u_m$. The resulting biphoton state can be written as

$$|\psi'\rangle = \sum_m \int \mathrm{d}k\, u_m\,|m_k\rangle_s\,|{-k}\rangle_i\,. \tag{11}$$

If a projection is performed onto a specific signal state, say $|k_0\rangle_s$, the obtained state on the idler side is

$$|\psi\rangle_i = \sum_m u_m\,|k_m - k_0\rangle_i\,. \tag{12}$$

RESULTS

The experimental setup is sketched in Fig. 2. It consists of a 1-mm thick Type-I BBO (β-Barium Borate) crystal pumped by a 405 nm pulsed laser. Down-converted signal and idler photons are generated and then probabilistically separated into two paths through a beamsplitter (BS). Two lenses in a $4f$ configuration are used to image the crystal plane onto the SLM plane on the signal side. A half-wave plate (not shown in the figure) is used to rotate the signal input polarization in order to maximize the conversion efficiency from the SLM. A phase hologram $\phi(x)$ corresponding to a particular unitary process is displayed on the SLM. The action of such a hologram on the signal photon can be expressed in the position basis as

$$|k\rangle_s \rightarrow \int \mathrm{d}x\, e^{i(\phi(x)+kx)}\,|x\rangle_s\,. \tag{13}$$

Equation (13) corresponds to the unitary action of the operator $\hat{U}$ visualized in the position space (cf. Eq. (10)). The holograms are generated as superpositions of sinusoidal gratings featuring spatial frequencies that are multiples of the transverse momentum unit $2\pi/\Lambda$. In our experiment, we set $\Lambda = 1\,\mathrm{mm}/7 \simeq 0.15\,\mathrm{mm}$. Afterward, both the signal and idler photons are redirected to two different regions of a time-stamping camera (TPX3CAM) [39, 40]. The camera is placed in the far field of the nonlinear crystal, which allows us to access the transverse momentum space of the signal and the idler photons. This allows us to experimentally verify the plane-wave pump approximation assumed in Eq. (1) by recording the momentum correlations of the photon pairs. These show very sharp, 1-pixel-wide anti-correlations, which validates the approximation.

The camera allows us to observe space-resolved coincidence images between the signal and the idler photons. In this way, upon postselection of a specific signal state, $|k_0\rangle_s$, the excited spectrum of momentum modes can be revealed in the far field of the idler photon,

$$|\psi\rangle_i = \sum_{k_m} u_m\,|k_m - k_0\rangle_i\,, \tag{14}$$

where each coefficient u_m corresponds to the m-th element of the phase function in the Fourier basis:

$$u_m = \int \mathrm{d}x\, e^{i\phi(x)} e^{-ik_m x}. \tag{15}$$

With the imaging system used in our setup, each momentum mode covers an area of approximately five pixels at the imaging plane. This scheme is used to implement a nonlocal transfer of the output of different unitary operations in both 1D and 2D configurations.

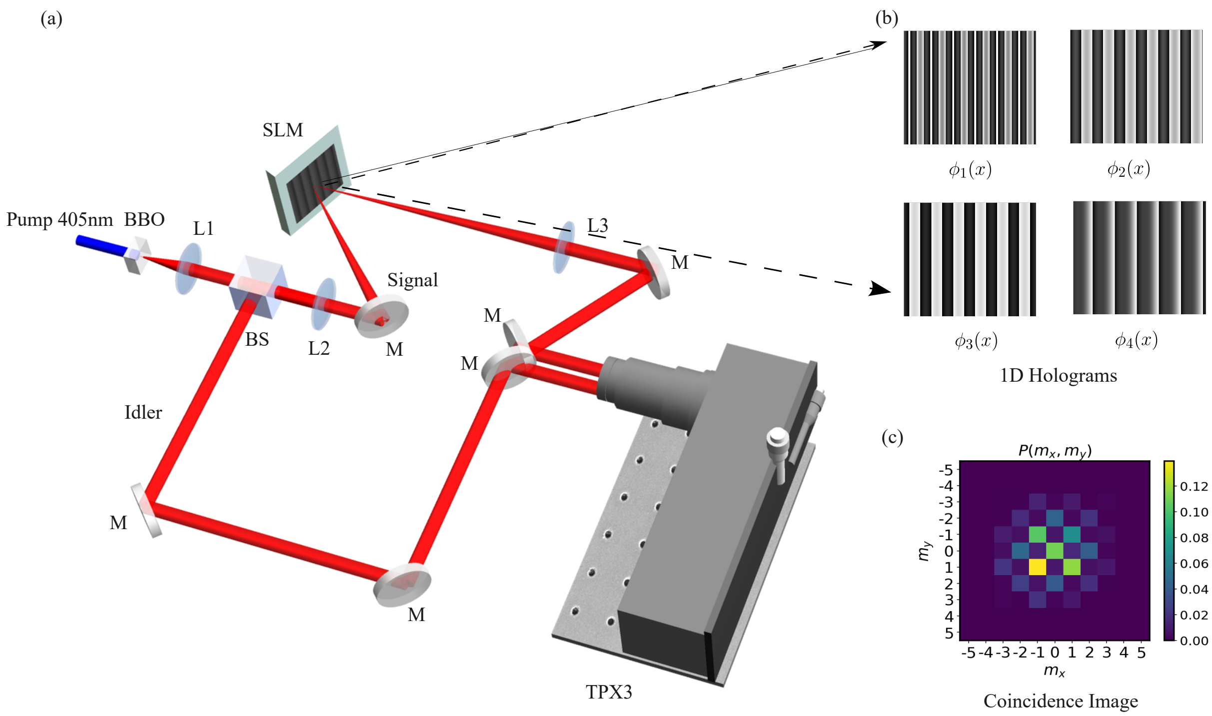

FIG. 2. **Experimental setup.** (a) A 405 nm laser illuminates a 1-mm type-I BBO crystal generating degenerate down-converted photon pairs. The idler and signal photons are probabilistically separated by a 50:50 beamsplitter (BS). The phase profile of the signal photon is modified by a Spatial Light Modulator (SLM), placed in the image plane of the crystal. The signal and idler photons are imaged onto different regions of a time-tagging TPX3CAM camera (TPX3), placed in the far field of the holograms. By performing a suitable postselection of the events in the signal image, the result of the unitary operation can be transferred to the idler photons. (b) Holograms for phases, $\phi_1(x) = 1.3\sin(\Delta k_\perp x) + 1.5\cos(2\Delta k_\perp x)$, $\phi_2(x) = 1.9\sin(\Delta k_\perp x)$, $\phi_3(x) = \cos(\Delta k_\perp x)$, and $\phi_4(x) = \cos(\Delta k_\perp x) + \Delta k_\perp x$, shown in grayscale color, corresponding to 1D unitary operations. The transferred far-field distribution recorded on the idler photon is shown in panel (c) for a 2D unitary as an example. BBO: Beta Barium Borate crystal; BS: Beamsplitter; SLM: Spatial Light Modulator; L1, L2, and L3: Lenses; M:Mirror.

A. One-dimensional simulation

The experimental results obtained for different 1D unitary operators are shown in Fig. 3(a). The projection on the signal state $|k_0 = 0\rangle_s$ is chosen for reference. As discussed above, upon suitable postselection of the signal events, the idler far-field distribution is discretized, and a normalized spectrum of momentum modes $P(m)$ is extracted. The latter can be interpreted as the probability of occupation of the lattice sites spanned by the optical modes introduced in Eq. (10). A comparison with the theoretical predictions, extracted from Eq. (15), is also provided. The agreement with the experimental observations is quantified by the similarity estimator $s = (\sum_m \sqrt{P_{\mathrm{exp}}(m) P_{\mathrm{th}}(m)})^2$, where $P_{\mathrm{exp}}(m)$ and $P_{\mathrm{th}}(m)$ are the experimental and theoretical far-field distributions, respectively. For all realizations, the similarity value exceeds 90%, which showcases the accuracy of our method and its robustness to experimental imperfections, such as a residual misalignment of the input polarization state with respect to the SLM optic axis, which results in higher contributions from the zeroth diffraction order. Another issue limiting the performance of our apparatus is the low resolution of the SLM employed in the experiment, (600×792) pixels. Poissonian statistics is assumed for computing error bars, which are always smaller than data points. Specifically, the holograms prepared in the 1D experiment are $\phi_1(x) = 1.3\sin(\Delta k_\perp x) + 1.5\cos(2\Delta k_\perp x)$, $\phi_2(x) = 1.9\sin(\Delta k_\perp x)$, $\phi_3(x) = \cos(\Delta k_\perp x)$, and $\phi_4(x) = \cos(\Delta k_\perp x) + \Delta k_\perp x$. Note that the transformation induced by $\phi_4(x)$ is equivalent to $\phi_3(x)$ with an additional initial one-site displacement. The corresponding similarities are $s = 95.7\%, 93.9\%, 90.6\%$, and 91.2%.

The 1D implementation also allows us to implement the transfer of a unitary action on an arbitrary input state. Assume that the idler party requests computing the output of the unitary $\hat{U}$ on a general input state

$$|\psi_0\rangle = \sum_\ell d_\ell |k_\ell\rangle, \tag{16}$$

where d_ℓ are complex coefficients obeying the normalization condition $\sum_\ell |d_\ell|^2 = 1$. Accordingly,

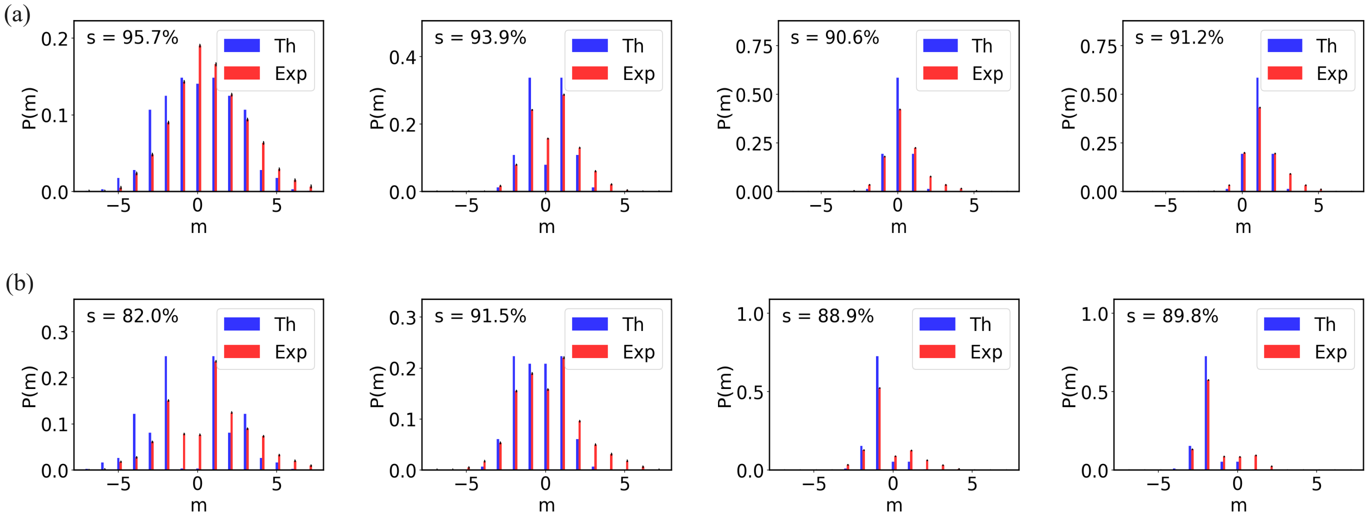

FIG. 3. **One-dimensional nonlocal transfer.** (a) Experimental probabilities for the momentum modes of the idler photon upon nonlocal transfer of different 1D lattice unitary operations, compared with theoretical predictions. From left to right: $\phi_1(x) = 1.3\sin(\Delta k_\perp x) + 1.5\cos(2\Delta k_\perp x)$, $\phi_2(x) = 1.9\sin(\Delta k_\perp x)$, $\phi_3(x) = \cos(\Delta k_\perp x)$, and $\phi_4(x) = \cos(\Delta k_\perp x) + \Delta k_\perp x$. (b) One-dimensional nonlocal transfer with arbitrary input states. Theoretical and experimental probabilities for the momentum modes of the idler photon upon nonlocal transfer of the same unitaries acting on the initial state $|\psi_0\rangle = (|0\rangle + i\,|1\rangle)/\sqrt{2}$.

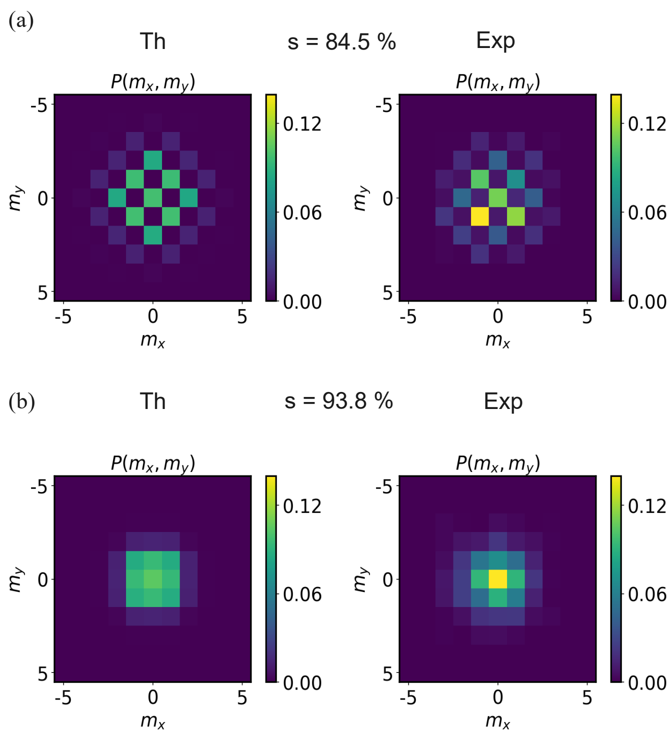

FIG. 4. **Two-dimensional nonlocal transfer.** Theoretical and experimental probabilities for the momentum modes of the idler photon upon nonlocal transfer of different 2D lattice unitaries. (a) $\phi_1(x, y) = 2.8\sin(\Delta k_\perp x)\cos(\Delta k_\perp y)$ and (b) $\phi_2(x, y) = 1.4\sin(\Delta k_\perp x) + 1.4\sin(\Delta k_\perp y)$.

the target state

$$|\psi\rangle_i = \sum_n \sum_\ell u_n d_\ell\, |k_\ell + k_n\rangle_i \tag{17}$$

is expected to be transferred from the signal end. To accomplish this, the signal photon is sent through a different operator $\hat{\mathcal{V}}$:

$$|\psi\rangle = \sum_m \int \mathrm{d}k\, v_m\, |k + k_m\rangle_s\, |{-k}\rangle_i\,, \tag{18}$$

where v_m are the elements of the spatial transformation associated with $\hat{\mathcal{V}}$ in the Fourier basis. Upon projection on a signal state, say $|k_0 = 0\rangle_s$, the resulting idler state reads

$$|\psi\rangle_i = \sum_m v_m\, |k_m\rangle_i\,. \tag{19}$$

Therefore, the specific operator $\hat{\mathcal{V}}$ to apply on the signal photon can be determined by equating Eq. (17) and Eq. (19), which yields

$$v_m = \sum_\ell d_\ell u_{m-\ell}. \tag{20}$$

The last equation reveals that the required operation is not a mere phase transformation. To effectively realize this transformation with a phase-only SLM, we employ the technique introduced in Ref. [41], which enables the manipulation of both phase and amplitude of the field with a single phase-only hologram at the cost of introducing additional losses. In particular, the Fourier transform of the desired field is found in correspondence with the first diffraction order. For this reason, the required phase-amplitude transformation, extracted from Eq. (20), is applied along x, and a blazing function $\mathrm{Mod}(2\pi/\Lambda_y, 2\pi)$ is added along the y direction, with $\Lambda_y = \Lambda/50 = 0.02\,\mathrm{mm}$. The spatial period Λ_y is chosen to be small enough to ensure a clear separation between the first diffraction order and the unmodulated light in the Fourier plane.

As a representative example, we apply this technique to transfer the outcomes of the same transformations considered before when applied to the delocalized input state $|\psi_0\rangle = (|0\rangle + i\,|1\rangle)/\sqrt{2}$. The experimental results are shown in Fig. 3(b). Good agreement with the theoretical distribution is observed, with an average similarity of 88.1%. This demonstrates the possibility of transferring also unitary operations that, in our optical encoding, do not correspond to simple phase transformations.

B. Two-dimensional simulation

The same concept is also tested in a 2D setting, where Eqs. (14) and (15) are generalized as follows:

$$|\psi\rangle_i = \sum_{k_{mx}} \sum_{k_{my}} u_{m_x,m_y} \,|k_{mx} - k_{0x}, k_{my} - k_{0y}\rangle_i\ ; \quad (21a)$$

$$u_{m_x,m_y} = \iint \mathrm{d}x\,\mathrm{d}y\, e^{i\phi(x,y)} e^{-ik_{mx}x} e^{-ik_{my}y}. \quad (21b)$$

The experimental results obtained for the 2D implementation are shown in Fig. 4, obtained upon postselection of the signal state $|k_{0x}, k_{0y}\rangle_s = |0,0\rangle_s$. In particular, two different simulations are considered, $\phi_1(x,y) = 2.8\sin(\Delta k_\perp x)\cos(\Delta k_\perp y)$ and $\phi_2(x,y) = 1.4\sin(\Delta k_\perp x) + 1.4\sin(\Delta k_\perp y)$. The recorded similarities are $s = 84.5\%$, and 93.8%, respectively. Notably, in the 2D case, the number of active modes grows faster than in the 1D implementation, thus allowing us to access large-scale simulations with fewer computational resources. Specifically, while in the 1D case the number of accessible modes scales linearly with the number of spatial frequencies encoded in the phase masks, in the 2D case this scaling becomes quadratic. In other words, by increasing the number of spatial frequencies in the holograms, the 2D configuration can support a significantly larger Hilbert space, enhancing the system's capability to simulate more complex quantum dynamics or encode high-dimensional quantum information.

C. Phase retrieval

Since we use a phase device to implement our scheme, the unitaries we consider experimentally are of the form $U(x,y) = e^{i\phi(x,y)}$. As an additional check of the quality of the transferred results, the phase transformations implementing the unitary action can be experimentally retrieved from two intensity distributions recorded in conjugate planes. In our case, we employ a hybrid Gerchberg-Saxton (GS) algorithm [42], which uses the near-field signal and far-field idler images (see Eq. (13) and Eq. (14), respectively), assuming perfect uniformity of the signal transverse profile. The GS

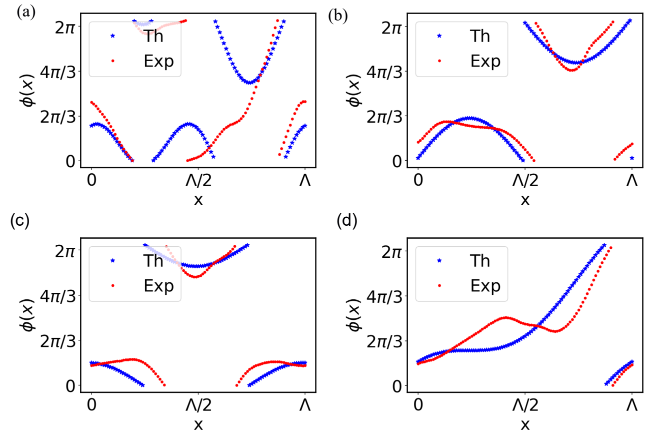

FIG. 5. **Phase reconstruction of one-dimensional unitary operations.** Experimental phase reconstructions of the 1D lattice unitaries. (a) $\phi_1(x) = 1.3\sin(\Delta k_\perp x) + 1.5\cos(2\Delta k_\perp x)$, (b) $\phi_2(x) = 1.9\sin(\Delta k_\perp x)$, (c) $\phi_3(x) = \cos(\Delta k_\perp x)$, and (d) $\phi_4(x) = \cos(\Delta k_\perp x) + \Delta k_\perp x$.

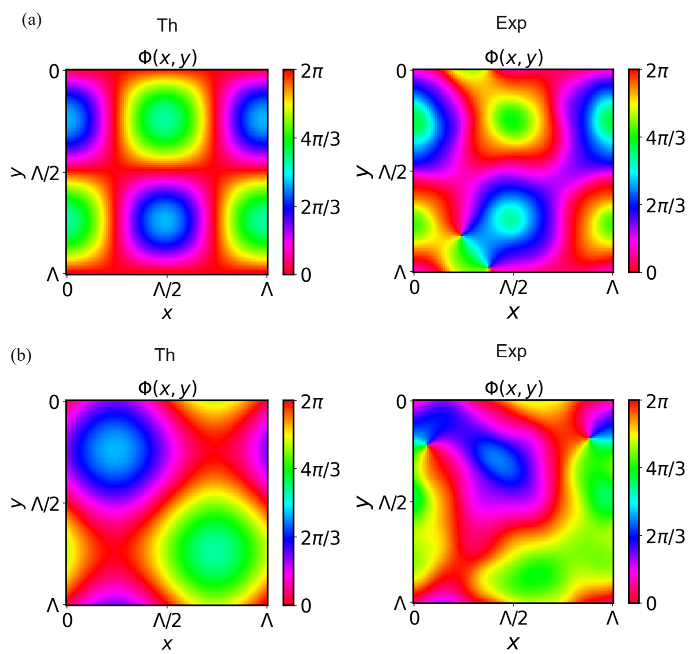

FIG. 6. **Phase reconstruction of two-dimensional unitary operations.** Experimental phase reconstructions of the 2D lattice unitaries. (a) $\phi_1(x,y) = 2.8\sin(\Delta k_\perp x)\cos(\Delta k_\perp y)$ and (b) $\phi_2(x,y) = 1.4\sin(\Delta k_\perp x) + 1.4\sin(\Delta k_\perp y)$.

algorithm is an iterative phase-retrieval method that reconstructs the phase of a complex wavefront from intensity measurements in two conjugate planes, typically the image and Fourier planes. Starting from a random input guess, it numerically propagates the beam back and forth between the two planes using the measured amplitudes as constraints, updating the phase at each iteration. This provides a non-interferometric approach to phase reconstructions. One of its strengths is that the error can only decrease (or stay the same) at each iteration [43]. However, this strategy presents intrinsic limitations. In particular, the convergence speed is sensitive to the initial phase guess, and the convergence to a global minimum is not guaranteed. For these reasons, multiple runs of the algorithm are typically needed for optimal convergence, with the input phase guess randomized at each trial. This allows us to identify the optimal phase reconstruction (up to global shifts) as the one that minimizes the total distance (summed over all the pixels) between the reconstructed and measured near-field amplitude profiles. The number of repetitions is chosen to ensure the stability of the final reconstruction. Alternatively, the routine can be stopped when the algorithm has converged below a tolerance threshold. In our experiment, we set $N_{\mathrm{R}} = 200$ and $N_{\mathrm{I}} = 200$ for the 1D case, where N_{R} is the number of independent runs and N_{I} the number of iterations within each run, while for the 2D case we set $N_{\mathrm{R}} = 100$ and $N_{\mathrm{I}} = 100$. The total computation time is less than 5 s and about 80 s for the 1D and 2D implementations, respectively.

The reconstructed phase modulations are plotted in Fig. 5 and Fig. 6 for the 1D and 2D implementations, respectively, where the comparison with the expected profile is also provided. For all reconstructions, a qualitatively good agreement is observed with the theoretical predictions, with some larger deviations in the 2D case that can be mainly ascribed to the low spatial resolution of the SLM and the camera, as well as aberrations in phase and amplitude of the pump beam, in addition to the intrinsic limitations of the GS algorithm.

DISCUSSION AND CONCLUSION

We demonstrated the nonlocal transfer of unitary operations between correlated photons in high dimensions. In our scheme, the party with access to the computational resource can transfer the desired output to remote clients upon a suitable projective measurement. This operation is accomplished at the expense of high-dimensional spatial correlations. The technique has been experimentally validated in both 1D and 2D configurations in the case of phase transformations.

Our setup efficiently processes a large number of co-propagating optical modes, which suggests potential use in future entanglement-based quantum key distribution [44] and quantum simulation protocols [45].

The implementation of the proposed protocol with transverse momentum modes in real-world scenarios would certainly suffer from the typical challenges of free-space optical communications, namely, the presence of atmospheric turbulence. Adaptive optics systems offer an effective solution for mitigating the effects of intermediate-scale turbulence or for operation over moderate propagation distances [46, 47]. Conversely, one could design multi-plane light converters to compensate for aberrations induced by turbulence [48]. Another approach could be to predict the turbulence strength in advance to find the best time to establish a secure connection [49]. Opposite to free-space solutions, multimode fibers could also be employed, but in that case, the distortion induced by the fiber itself must be taken into account and compensated for [50, 51]. Alternatively, since the biphoton state is also correlated in other degrees of freedom, such as frequency, one could adapt the protocol in such Hilbert spaces.

With high-dimensional correlations being the only physical requirement, the same scheme can also be applied to transfer operations in the orbital angular momentum space [52]. By replacing the phase holograms with birefringent patterned optical elements, such as liquid-crystal [36] or dielectric metasurfaces [53], our technique could be refined to transfer more complex operations coupling polarization and spatial degrees of freedom. Moreover, by adding a controlled amount of losses on a subset of modes, the extension to non-unitary transformations could also be explored [54]. Further exciting prospects involve the generalization of similar concepts to a larger number of input photons, typical in Boson sampling implementations [55, 56]. This will require further theoretical investigations.

Acknowledgement. This work was supported by the Canada Research Chair (CRC) Program, NRC-uOttawa Joint Centre for Extreme Quantum Photonics (JCEP) via the Quantum Sensors Challenge Program at the National Research Council of Canada, and Quantum Enhanced Sensing and Imaging (QuEnSI) Alliance Consortia Quantum grant. FDC acknowledges support from the PNRR MUR project PE0000023-NQSTI.

Disclosures. The authors declare no conflicts of interest.

Data availability. The source code and data underlying the results presented in this paper can be obtained from the corresponding author upon reasonable request.

Author Contributions. DP and FDC conceived the idea. DP developed the theory for general unitary operators. FDC developed the theory adapted to translation-invariant operators and designed the holograms. DP and FDC performed the experiment and data analysis. DP and FDC prepared the first draft of the manuscript. ADE and EK supervised the project. All authors discussed the results and contributed to the final version of the manuscript.

[1] R. Horodecki, P. Horodecki, M. Horodecki, and K. Horodecki, Quantum entanglement, Rev. Mod. Phys. **81**, 865 (2009).
[2] D. Paneru, E. Cohen, R. Fickler, R. W. Boyd, and E. Karimi, Entanglement: quantum or classical?, Rep. Progr. Phys. **83**, 064001 (2020).
[3] A. Einstein, B. Podolsky, and N. Rosen, Can quantum-mechanical description of physical reality be considered complete?, Phys. Rev. **47**, 777 (1935).
[4] J. S. Bell, On the einstein podolsky rosen paradox, Physics Physique Fizika **1**, 195 (1964).
[5] R. Jozsa and N. Linden, On the role of entanglement in quantum-computational speed-up, Proc. R. Soc. Lond. A **459**, 2011 (2003).
[6] V. Giovannetti, S. Lloyd, and L. Maccone, Advances in quantum metrology, Nat. Photonics **5**, 222 (2011).
[7] R. Demkowicz-Dobrzański and L. Maccone, Using entanglement against noise in quantum metrology, Phys. Rev. Lett. **113**, 250801 (2014).
[8] C. H. Bennett and G. Brassard, Quantum cryptography: Public key distribution and coin tossing, Theor. Comput. Sci. **560**, 7 (2014).
[9] R. Ursin, F. Tiefenbacher, T. Schmitt-Manderbach, H. Weier, T. Scheidl, M. Lindenthal, B. Blauensteiner, T. Jennewein, J. Perdigues, P. Trojek, *et al.*, Entanglement-based quantum communication over 144 km, Nat. Phys. **3**, 481 (2007).
[10] C. K. Hong and L. Mandel, Theory of parametric frequency down conversion of light, Phys. Rev. A **31**, 2409 (1985).
[11] S. P. Walborn, C. Monken, S. Pádua, and P. S. Ribeiro, Spatial correlations in parametric down-conversion, Phys. Rep. **495**, 87 (2010).
[12] A. Aspect, J. Dalibard, and G. Roger, Experimental test of bell's inequalities using time-varying analyzers, Phys. Rev. Lett. **49**, 1804 (1982).
[13] D. Bouwmeester, J.-W. Pan, K. Mattle, M. Eibl, H. Weinfurter, and A. Zeilinger, Experimental quantum teleportation, Nature **390**, 575 (1997).
[14] P.-A. Moreau, E. Toninelli, T. Gregory, and M. J. Padgett, Imaging with quantum states of light, Nat. Rev. Phys. **1**, 367 (2019).
[15] J. H. Shapiro and R. W. Boyd, The physics of ghost imaging, Quantum Inf. Process. **11**, 949 (2012).
[16] F. Devaux, A. Mosset, F. Bassignot, and E. Lantz, Quantum holography with biphotons of high schmidt number, Phys. Rev. A **99**, 033854 (2019).
[17] D. Zia, N. Dehghan, A. D'Errico, F. Sciarrino, and E. Karimi, Interferometric imaging of amplitude and phase of spatial biphoton states, Nat. Photonics **17**, 1009 (2023).
[18] E. Schrödinger, Discussion of probability relations between separated systems, Mathematical Proceedings of the Cambridge Philosophical Society **31**, 555–563 (1935).
[19] E. Schrödinger, Probability relations between separated systems, Mathematical Proceedings of the Cambridge Philosophical Society **32**, 446–452 (1936).
[20] H. M. Wiseman, S. J. Jones, and A. C. Doherty, Steering, entanglement, nonlocality, and the einstein-podolsky-rosen paradox, Phys. Rev. Lett. **98**, 140402 (2007).
[21] S. F. Huelga, M. B. Plenio, G.-Y. Xiang, J. Li, and G.-C. Guo, Remote implementation of quantum operations, J. Opt. B: Quantum Semiclass. Opt. **7**, S384 (2005).
[22] H. Bechmann-Pasquinucci and W. Tittel, Quantum cryptography using larger alphabets, Phys. Rev. A **61**, 062308 (2000).
[23] S. Designolle, V. Srivastav, R. Uola, N. H. Valencia, W. McCutcheon, M. Malik, and N. Brunner, Genuine high-dimensional quantum steering, Phys. Rev. Lett. **126**, 200404 (2021).
[24] N. Herrera Valencia, V. Srivastav, M. Pivoluska, M. Huber, N. Friis, W. McCutcheon, and M. Malik, High-Dimensional Pixel Entanglement: Efficient Generation and Certification, Quantum **4**, 376 (2020).
[25] D. Gottesman and I. L. Chuang, Demonstrating the viability of universal quantum computation using teleportation and single-qubit operations, Nature **402**, 390 (1999).
[26] D. Bouwmeester, J.-W. Pan, K. Mattle, M. Eibl, H. Weinfurter, and A. Zeilinger, Experimental quantum teleportation, Nature **390**, 575 (1997).
[27] L. Caha, X. Coiteux-Roy, and R. Koenig, Single-qubit gate teleportation provides a quantum advantage, Quantum **8**, 1548 (2024).
[28] W.-Q. Liu and H.-R. Wei, Quantum gate teleportation with the superposition of causal order, Phys. Rev. Appl. **23**, 014064 (2025).
[29] Y.-F. Huang, X.-F. Ren, Y.-S. Zhang, L.-M. Duan, and G.-C. Guo, Experimental teleportation of a quantum controlled-not gate, Phys. Rev. Lett. **93**, 240501 (2004).
[30] W.-B. Gao, A. M. Goebel, C.-Y. Lu, H.-N. Dai, C. Wagenknecht, Q. Zhang, B. Zhao, C.-Z. Peng, Z.-B. Chen, Y.-A. Chen, and J.-W. Pan, Teleportation-based realization of an optical quantum two-qubit entangling gate, Proc. Natl. Acad. Sci. **107**, 20869 (2010).
[31] K. S. Chou, J. Z. Blumoff, C. S. Wang, P. C. Reinhold, C. J. Axline, Y. Y. Gao, L. Frunzio, M. H. Devoret, L. Jiang, and R. J. Schoelkopf, Deterministic teleportation of a quantum gate between two logical qubits, Nature **561**, 368 (2018).
[32] Y. Wan, D. Kienzler, S. D. Erickson, K. H. Mayer, T. R. Tan, J. J. Wu, H. M. Vasconcelos, S. Glancy, E. Knill, D. J. Wineland, A. C. Wilson, and D. Leibfried, Quantum gate teleportation between separated qubits in a trapped-ion processor, Science **364**, 875 (2019).
[33] N. de Silva, Efficient quantum gate teleportation in higher dimensions, Proc. R. Soc. A: Math. Phys. Eng. Sci. **477**, 20200865 (2021).
[34] S. Goel, S. Leedumrongwatthanakun, N. H. Valencia, W. McCutcheon, A. Tavakoli, C. Conti, P. W. Pinkse, and M. Malik, Inverse design of high-dimensional quantum optical circuits in a complex medium, Nat.

Phys. **20**, 232 (2024).

[35] A. D'Errico, F. Cardano, M. Maffei, A. Dauphin, R. Barboza, C. Esposito, B. Piccirillo, M. Lewenstein, P. Massignan, and L. Marrucci, Two-dimensional topological quantum walks in the momentum space of structured light, Optica **7**, 108 (2020).

[36] F. Di Colandrea, A. Babazadeh, A. Dauphin, P. Massignan, L. Marrucci, and F. Cardano, Ultra-long quantum walks via spin–orbit photonics, Optica **10**, 324 (2023).

[37] J. F. Fitzsimons, Private quantum computation: an introduction to blind quantum computing and related protocols, Npj Quantum Inf. **3**, 23 (2017).

[38] S.-H. Wei, B. Jing, X.-Y. Zhang, J.-Y. Liao, C.-Z. Yuan, B.-Y. Fan, C. Lyu, D.-L. Zhou, Y. Wang, G.-W. Deng, *et al.*, Towards real-world quantum networks: A review, Laser Photonics Rev. **16**, 2100219 (2022).

[39] A. Nomerotski, Imaging and time stamping of photons with nanosecond resolution in timepix based optical cameras, Nucl. Instrum. Methods Phys. Res. A **937**, 26 (2019).

[40] A. Nomerotski, M. Chekhlov, D. Dolzhenko, R. Glazenborg, B. Farella, M. Keach, R. Mahon, D. Orlov, and P. Svihra, Intensified tpx3cam, a fast data-driven optical camera with nanosecond timing resolution for single photon detection in quantum applications, J. Instrum. **18** (01), C01023.

[41] E. Bolduc, N. Bent, E. Santamato, E. Karimi, and R. W. Boyd, Exact solution to simultaneous intensity and phase encryption with a single phase-only hologram, Opt. Lett. **38**, 3546 (2013).

[42] R. Gerhberg and W. Saxton, A practical algorithm for the determination of phase from image and diffraction plane picture, Optik **35**, 237 (1972).

[43] J. R. Fienup, Phase retrieval algorithms: a comparison, Appl. Opt. **21**, 2758 (1982).

[44] A. K. Ekert, Quantum cryptography based on bell's theorem, Phys. Rev. Lett. **67**, 661 (1991).

[45] M. K. Joshi, C. Kokail, R. van Bijnen, F. Kranzl, T. V. Zache, R. Blatt, C. F. Roos, and P. Zoller, Exploring large-scale entanglement in quantum simulation, Nature **624**, 539 (2023).

[46] P. Hickson, Atmospheric and adaptive optics, Astron. Astrophys. Rev. **22**, 76 (2014).

[47] L. Scarfe, F. Hufnagel, M. F. Ferrer-Garcia, A. D'Errico, K. Heshami, and E. Karimi, Fast adaptive optics for high-dimensional quantum communications in turbulent channels, Commun. Phys. **8**, 79 (2025).

[48] P. Cho, P. M. Pellegrino, J. Bickford, and A. Bontzos, Investigation of turbulence-tolerant free-space optical communications via multiplane light conversion, Opt. Eng. **61**, 116104 (2022).

[49] T. Jaouni, L. Scarfe, F. Bouchard, M. Krenn, K. Heshami, F. Di Colandrea, and E. Karimi, Predicting atmospheric turbulence for secure quantum communications in free space, Opt. Express **33**, 10759 (2025).

[50] X. Shen, J. M. Kahn, and M. A. Horowitz, Compensation for multimode fiber dispersion by adaptive optics, Opt. Lett. **30**, 2985 (2005).

[51] N. H. Valencia, S. Goel, W. McCutcheon, H. Defienne, and M. Malik, Unscrambling entanglement through a complex medium, Nat. Phys. **16**, 1112 (2020).

[52] A. Mair, A. Vaziri, G. Weihs, and A. Zeilinger, Entanglement of the orbital angular momentum states of photons, Nature **412**, 313 (2001).

[53] R. C. Devlin, A. Ambrosio, D. Wintz, S. L. Oscurato, A. Y. Zhu, M. Khorasaninejad, J. Oh, P. Maddalena, and F. Capasso, Spin-to-orbital angular momentum conversion in dielectric metasurfaces, Opt. Express **25**, 377 (2017).

[54] C. Wang, Z. Fu, W. Mao, J. Qie, A. D. Stone, and L. Yang, Non-hermitian optics and photonics: from classical to quantum, Adv. Opt. Photon. **15**, 442 (2023).

[55] H.-S. Zhong, H. Wang, Y.-H. Deng, M.-C. Chen, L.-C. Peng, Y.-H. Luo, J. Qin, D. Wu, X. Ding, Y. Hu, *et al.*, Quantum computational advantage using photons, Science **370**, 1460 (2020).

[56] J. M. Arrazola, V. Bergholm, K. Brádler, T. R. Bromley, M. J. Collins, I. Dhand, A. Fumagalli, T. Gerrits, A. Goussev, L. G. Helt, *et al.*, Quantum circuits with many photons on a programmable nanophotonic chip, Nature **591**, 54 (2021).

Generation of the complete Bell basis via Hong-Ou-Mandel interference of vector modes

Xiaoqin Gao,[1,*] Dilip Paneru,[1] Francesco Di Colandrea,[1,2,†] Yingwen Zhang,[1,3,‡] and Ebrahim Karimi[1,3,4]

[1]*Nexus for Quantum Technologies, University of Ottawa, Ottawa, Ontario, Canada K1N 5N6*
[2]*Dipartimento di Fisica, Università degli Studi di Napoli Federico II, Complesso Universitario di Monte Sant'Angelo, Via Cintia, 80126 Napoli, Italy*
[3]*National Research Council of Canada, 100 Sussex Drive, Ottawa, Ontario, Canada K1A 0R6*
[4]*Institute for Quantum Studies, Chapman University, Orange, California 92866, USA*

(Received 21 December 2024; accepted 16 June 2025; published 17 July 2025)

Optical vector modes (VMs), characterized by spatially varying polarization distributions, have become essential tools across microscopy, metrology, optical trapping, nanophotonics, and optical communications. Here, we investigate the Hong-Ou-Mandel (HOM) interference of VMs providing a full spatial characterization of the output state. We find that, by carefully selecting the input VMs, it is possible to simultaneously observe all four polarization Bell states and their superpositions in the spatially varying polarization pattern of the two photons. These results represent a significant step in advancing our understanding of HOM interference within structured photons, offering promising avenues for high-dimensional quantum information processing and, in particular, high-dimensional quantum communication, quantum sensing, and advanced photonic technologies reliant on tailored quantum states of light.

DOI: 10.1103/dcxb-ql1r

I. INTRODUCTION

Hong-Ou-Mandel (HOM) interference is a two-particle quantum interference effect and plays a central role in many quantum technologies that require interaction between two particles [1,2]. When two indistinguishable photons enter a 50:50 beam splitter from different input ports, the photons destructively interfere and experience "bunching," in which they exit through the same output port of the beam splitter, resulting in the well-known dip in coincidence counts. If the two input photons are entangled, then a HOM dip in the coincidences will be observed if the two photons' entangled state is symmetric, and a HOM peak will be observed if the entangled state is antisymmetric. HOM interference is widely used in photonic quantum experiments, such as the implementation of quantum logic gates [3], quantum imaging [4,5], quantum communication [6], and optimal quantum cloning [7–9]. The effect is also used to characterize photon-pair sources [10], optimize quantum teleportation [11], and enable Boson sampling experiments [12,13].

Vector modes (VMs), also known as vector vortex modes, possess a distinctive spatially varying polarization structure that differentiates them from homogeneously polarized light beams [14]. This characteristic has allowed its application in various fields, including nonlinear optics [15], high-resolution imaging [16], and optical trapping [17,18]. VMs also offer enhanced capabilities, such as sharper focus spots [19,20], and improved performance in quantum key distribution [21,22]. Two primary methods for generating VMs are the intracavity method, which incorporates mode-selection optical elements within a laser resonator [23–25], and the extracavity method, which employs specialized optical components, such as q-plates [26–28] or spatial light modulators within Sagnac interferometers, to convert Gaussian beams into VMs [29]. The entanglement of VMs has also been explored, where polarization-entangled photon pairs are converted into VMs, creating a complex, spatially varying entanglement structure [30–34].

Recent studies on HOM interference with VMs have revealed spatially distributed HOM dips and peaks [35]. However, these studies are restricted to two spatial dimensions, focusing on the spatially dependent polarization structure of photons from only one of the interferometer's output ports, captured with an event camera, while photons in the other port are detected with a bucket detector. By correlating time-stamped events between the camera and the bucket detector, a two-dimensional map of the final-state structure was constructed. Nevertheless, the complete structure of the VMs after HOM interference is inherently four-dimensional as it depends on the spatial coordinates of photons from both output ports.

Here, we demonstrate a full spatial characterization of HOM interference with VMs, revealing the complete four-dimensional state structure. Remarkably, unlike previous studies suggesting that only the antisymmetric Bell state ψ^- can emerge from HOM interference when postselecting on

*Present address: National Laboratory of Solid State Microstructures and School of Physics, Collaborative Innovation Center of Advanced Microstructures, Jiangsu Physical Science Research Center, Nanjing University, Nanjing, Jiangsu 210093, China.
†Contact author:
‡Contact author:

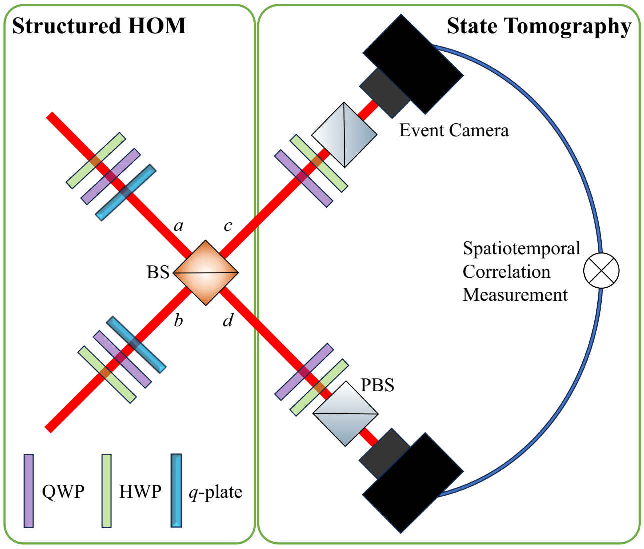

FIG. 1. Space-resolved HOM interference of VMs. Single Gaussian modes are sent to two q-plates to create VMs. These overlap at a 50:50 beam splitter (BS), where HOM interference occurs. Space-resolved polarization state tomography is performed by recording the outputs of two projection stages, consisting of a QWP, a HWP, and a polarizing beam splitter (PBS), onto two event cameras (in the actual experiment, two different regions of a single camera were used instead). By extracting temporal-spatial correlated events between all pixels of the two cameras, a spatially varying density matrix can be retrieved, from which the distribution of the Bell states is obtained.

coincidence events between the two output ports, we find that interference between specific VM combinations can simultaneously yield all four polarization Bell states and their superpositions, depending on the relative transverse spatial locations of detected photons in the two output ports. We believe that this finding has significant implications for quantum technologies that leverage HOM interference.

II. RESULTS

A simplified experimental scheme for realizing HOM interference of VMs is shown in Fig. 1; the detailed experimental setup can be found in the Supplemental Material [36]. Photon pairs are generated from spontaneous parametric down-conversion (SPDC) in a type-II 5-mm-long periodically poled potassium titanyl phosphate (ppKTP) crystal and coupled to single-mode fibers (not shown in the figure) to select only the Gaussian mode. Two sets of quarter-wave plates (QWPs) and half-wave plates (HWPs) are used to prepare the input polarization states:

$$|\psi_0\rangle = a^\dagger_{\pi_1} b^\dagger_{\pi_2} |0\rangle , \tag{1}$$

where $a^\dagger_{\pi_1}$ ($b^\dagger_{\pi_2}$) is the creation operator for a photon in input port a (b) with polarization $|\pi_1\rangle$ ($|\pi_2\rangle$). The two photons are then sent to two q-plates. In the circular polarization basis, where $|L\rangle$ and $|R\rangle$ are left-handed and right-handed circular polarization states, the action of a q-plate with topological charge q and birefringence δ on an input Gaussian mode is [37,38]

$$\hat{U}^\delta_q \begin{bmatrix} |L\rangle \\ |R\rangle \end{bmatrix} = F_0(r)\cos\left(\frac{\delta}{2}\right)\begin{bmatrix} |L\rangle \\ |R\rangle \end{bmatrix} + i\sin\left(\frac{\delta}{2}\right)F_q(r)\begin{bmatrix} e^{-i2q\theta}\,|R\rangle \\ e^{i2q\theta}\,|L\rangle \end{bmatrix}, \tag{2}$$

where r and θ are the radial and azimuthal coordinate in the transverse plane, respectively, and $F_0(r)$ and $F_q(r)$ are hypergeometric-Gauss functions [39], which can be approximated as the Laguerre-Gauss mode with the orbital angular

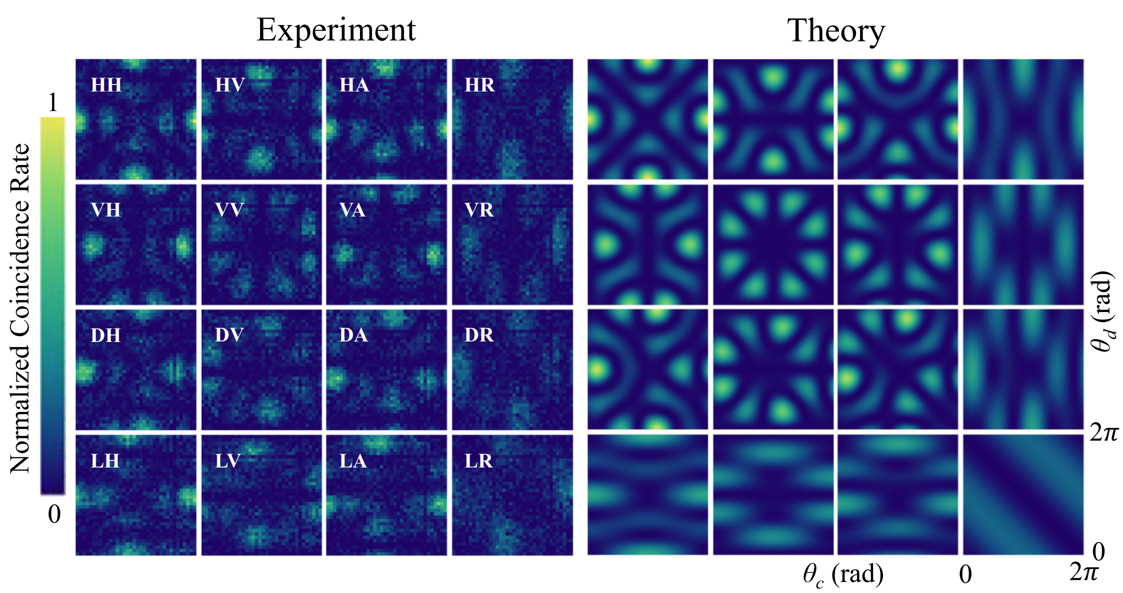

FIG. 2. Space-resolved polarimetry of HOM interference of VMs. Experimental (left panels) and theoretical (right panels) azimuthal correlations of the two-photon state for the 16 projections required for the complete state tomography. The topological charges of the two q-plates are $q_a = 1$ and $q_b = 1/2$. The initial state is $\hat{a}^\dagger_H \hat{b}^\dagger_H |0\rangle$.

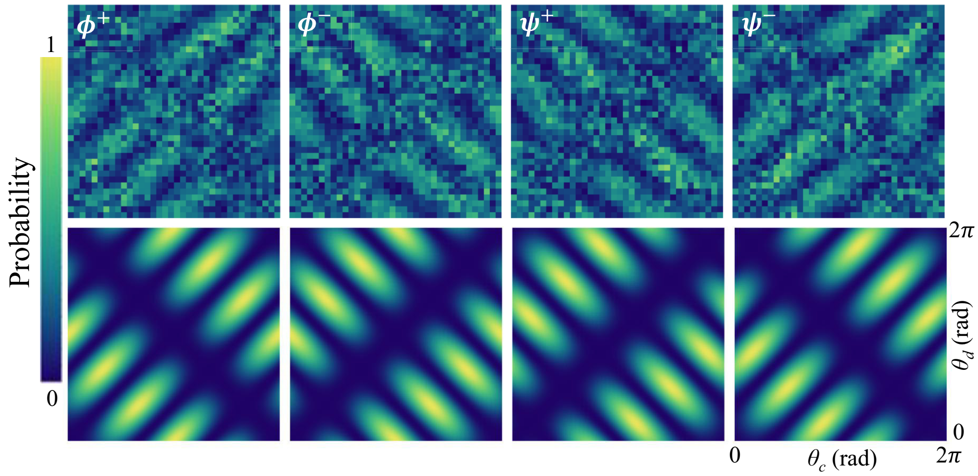

FIG. 3. Probability distributions of the four Bell states. Experimental (top row) and theoretical (bottom row) spatial patterns of the four Bell states obtained via HOM interference of VMs for the case study $q_a = 1$ and $q_b = 1/2$ and the initial state $\hat{a}_H^\dagger \hat{b}_H^\dagger |0\rangle$.

momentum index $\ell = 2q$ and a radial index equal to 0: $F_q(r)e^{\pm i2q\theta} \equiv \mathrm{LG}_{\pm 2q,0}(r,\theta)$.

The birefringence parameter δ is uniform across the plate and can be electrically controlled [40]. In this experiment, we set $\delta = \pi$, which corresponds to a fully tuned q-plate. Interference between VMs takes place within a 50:50 beam splitter (BS), whose action, neglecting a global phase, reads

$$\begin{aligned} |\psi\rangle_a &\xrightarrow{\text{BS}} \frac{1}{\sqrt{2}}(|\psi\rangle_c + |\psi\rangle_d), \\ |\psi\rangle_b &\xrightarrow{\text{BS}} \frac{1}{\sqrt{2}}(|\psi\rangle_c - |\psi\rangle_d), \end{aligned} \tag{3}$$

where c and d are the output ports, and the transformation applies to all degrees of freedom. Assuming two horizontally polarized input photons, $|\psi_0\rangle = a_H^\dagger b_H^\dagger |0\rangle$, with $|H\rangle = (|L\rangle + |R\rangle)/\sqrt{2}$, and after postselecting only on coincidence events between output ports c and d, the resulting state after the BS can be written as (see the Supplemental Material for the detailed derivation [36])

$$|\psi_f\rangle = \mathcal{N}(s_{\phi^+}|\phi^+\rangle + s_{\phi^-}|\phi^-\rangle + s_{\psi^+}|\psi^+\rangle + s_{\psi^-}|\psi^-\rangle), \tag{4}$$

where $\mathcal{N}$ is a normalization constant; $|\phi^\pm\rangle = (|HH\rangle \pm |VV\rangle)/\sqrt{2}$ and $|\psi^\pm\rangle = (|HV\rangle \pm |VH\rangle)/\sqrt{2}$ are the four polarization Bell states; and $s_{\phi^\pm}$ and $s_{\psi^\pm}$ are given by

$$\begin{aligned} s_{\phi^+} &= F_{q_a}(r_d)F_{q_b}(r_c)\cos(2q_a\theta_d - 2q_b\theta_c) \\ &\quad - F_{q_a}(r_c)F_{q_b}(r_d)\cos(2q_a\theta_c - 2q_b\theta_d), \\ s_{\phi^-} &= F_{q_a}(r_d)F_{q_b}(r_c)\cos(2q_a\theta_d + 2q_b\theta_c) \\ &\quad - F_{q_a}(r_c)F_{q_b}(r_d)\cos(2q_a\theta_c + 2q_b\theta_d), \\ s_{\psi^+} &= F_{q_a}(r_d)F_{q_b}(r_c)\sin(2q_a\theta_d + 2q_b\theta_c) \\ &\quad - F_{q_a}(r_c)F_{q_b}(r_d)\sin(2q_a\theta_c + 2q_b\theta_d), \\ s_{\psi^-} &= F_{q_a}(r_d)F_{q_b}(r_c)\sin(2q_a\theta_d - 2q_b\theta_c) \\ &\quad + F_{q_a}(r_c)F_{q_b}(r_d)\sin(2q_a\theta_c - 2q_b\theta_d), \end{aligned} \tag{5}$$

with q_a (q_b) being the topological charge of the q-plate in input port a (b).

To experimentally characterize this state, the output photons are sent to a polarization tomography apparatus consisting of a QWP, a HWP, and a polarizing beam splitter (PBS) in each output arm, and they are then directed to two different regions of an event camera (TPX3CAM) [41,42]. The size of the beam spot on the camera covers approximately 30×30 pixels. Photon pairs are identified using time-correlation measurements between the camera pixels. The space-resolved outcomes of 16 polarimetric measurements are processed with a maximum-likelihood method to retrieve a density matrix, $\rho(r_c,\theta_c,r_d,\theta_d)$, at each pixel [43], from which the probability distributions of the four Bell states are extracted:

$$\begin{aligned} P_{\phi^\pm}(r_c,\theta_c,r_d,\theta_d) &= \langle\phi^\pm|\rho(r_c,\theta_c,r_d,\theta_d)|\phi^\pm\rangle, \\ P_{\psi^\pm}(r_c,\theta_c,r_d,\theta_d) &= \langle\psi^\pm|\rho(r_c,\theta_c,r_d,\theta_d)|\psi^\pm\rangle. \end{aligned} \tag{6}$$

Figure 2 shows the complete set of 16 polarization measurements from the two output ports with the two q-plates having topological charges $q_a = 1$ and $q_b = 1/2$. Due to the cylindrical symmetry of the Laguerre-Gauss modes in which the final state showed minimal variations with respect to the radial coordinates, we only plotted the azimuthal correlations for each polarization projection, obtained as the marginal distributions $P(\theta_c,\theta_d) = \sum_{r_c,r_d} P(r_c,\theta_c,r_d,\theta_d)$. The comparison with theoretical predictions (gray scale), calculated from Eq. (4), shows good agreement in all polarization projections.

From the reconstructed marginal density matrix $\rho(\theta_c,\theta_d)$, we extracted the corresponding space-dependent Bell state decomposition, as shown in Fig. 3. Contrary to the typical HOM effect, where only the ψ^- state is expected to be observed when conditioned on coincidence events between the two output ports, the output states of VM HOM feature contributions from all Bell states, depending on the specific location in the coordinate space. The locations where each Bell state can be uniquely found require the following conditions be met:

$$\begin{aligned}
\text{only } P_{\phi^+} > 0 \text{ iff } \quad & (q_a + q_b)(\theta_c - \theta_d) = \frac{(2n+1)\pi}{2} \\
& \text{and} \quad (q_a - q_b)(\theta_c - \theta_d) = m\pi; \\
\text{only } P_{\phi^-} > 0 \text{ iff } \quad & (q_a + q_b)(\theta_c + \theta_d) = \frac{(2n+1)\pi}{2} \\
& \text{and} \quad (q_a - q_b)(\theta_c + \theta_d) = m\pi; \\
\text{only } P_{\psi^+} > 0 \text{ iff } \quad & (q_a + q_b)(\theta_c + \theta_d) = n\pi \\
& \text{and} \quad (q_a - q_b)(\theta_c + \theta_d) = m\pi; \\
\text{only } P_{\psi^-} > 0 \text{ iff } \quad & (q_a + q_b)(\theta_c - \theta_d) = n\pi \\
& \text{and} \quad (q_a - q_b)(\theta_c - \theta_d) = m\pi,
\end{aligned} \tag{7}$$

with n and m being integers. From this, we also obtain the following conditions on q_a and q_b:

$$\begin{aligned}
\text{only } P_{\phi^+} > 0 \text{ iff } \quad & q_a = \frac{(2n+2m+1)}{(2n-2m+1)} q_b; \\
\text{only } P_{\phi^-} > 0 \text{ iff } \quad & q_a = \frac{(2n+2m+1)}{(2n-2m+1)} q_b; \\
\text{only } P_{\psi^+} > 0 \text{ iff } \quad & q_a = \frac{(n+m)}{(n-m)} q_b; \\
\text{only } P_{\psi^-} > 0 \text{ iff } \quad & q_a = \frac{(n+m)}{(n-m)} q_b; \\
\text{for all cases } \quad & |q_a| \neq |q_b|.
\end{aligned} \tag{8}$$

In the case where $q_a = 1$ and $q_b = 1/2$, the conditions are satisfied for only $P_{\psi^+} > 0$ if and only if $\theta_c = -\theta_d$ and for only $P_{\psi^-} > 0$ where $\theta_c = \theta_d$; however, the conditions cannot be satisfied for only $P_{\phi^+} > 0$ or only $P_{\phi^-} > 0$. Along the directions $\theta_c = -\theta_d$ and $\theta_c = \theta_d$, average purities of 0.76 ± 0.15 and 0.74 ± 0.14 were recorded, respectively, where the error is given by the standard deviation over all the pixels. The smallest q_a and q_b values where all four Bell states can be uniquely found are $q_a = \pm 3/2$ and $q_b = \mp 1/2$. For more details on the derivation of the conditions in Eq. (7), see the Supplemental Material [36]. Polarization measurements and Bell state decomposition for different q-plate settings and input polarization states can also be found in the Supplemental Material [36].

III. CONCLUSIONS

In conclusion, we investigated the HOM interference of VMs and, by performing a full spatial characterization of the spatially varying polarization structure of the two photons, we found that the resulting spatial distribution is composed of a superposition of all four Bell states and, under certain conditions, all four Bell states can be uniquely found simultaneously within this spatial distribution. We provided theoretical and experimental evidence of this effect in the case of VMs generated by q-plates, which naturally induce an azimuthal structure on the final distribution. However, this functionality can be easily generalized to arbitrary spatial patterns [44], allowing the distribution of Bell states of the output to be tailored to specific demands. For instance, liquid-crystal polarization gratings (g-plates) [45] could be used to map each Bell state onto a two-dimensional Cartesian grid.

Compared to the conventional approach based on applying local operations to convert each Bell state into any other [46], our method offers the remarkable advantage of multiplexing this operation with the only need of a single event camera, thus avoiding bulky setups requiring multiple beam splitters, wave plates, and single-photon detectors. At the same time, our setup can also address superpositions of Bell states instead of pure Bell states, to be used in entanglement-based communication [47,48], computation [49], and error-correction protocols [50,51]. In the near future, it would be interesting to extend similar concepts to a higher number of input photons, where the controlled generation of multiparticle maximally entangled states remains extremely challenging [52–54].

A major limiting factor in the accuracy of the results, which we estimate to have a 10–30% uncertainty on the number of coincidences detected between the camera pixels for our dataset, is the detection efficiency of the experimental setup, which is only $\sim$1%. This low efficiency is mainly due to the quantum efficiency of the event camera, which is around 8% [55], combined with spatially filtering the SPDC using single-mode fibers, and losses in the optical elements. To reduce data-acquisition time and improve photon statistics, we limited the beam size to a resolution of 30×30 pixels on the camera. Although we could use a higher resolution, achieving the same number of coincidences per pixel would require a much longer data-acquisition time. However, these are only technical limitations of the detection system. With more efficient event-based cameras [56], we expect that the accuracy and detection time of our detection method can be significantly improved.

ACKNOWLEDGMENTS

The authors thank Ryan Hogan for valuable discussions. This work was supported by the Canada Research Chairs (CRC) and the NRC-uOttawa Joint Centre for Extreme Quantum Photonics (JCEP) via the Quantum Sensors Challenge Program at the National Research Council of Canada. X.G. is grateful for the support of the Natural Science Foundation of Jiangsu Province (Grant No. BK20233001). F.D.C. acknowledges support from the PNRR MUR under Project No. PE0000023-NQSTI.

DATA AVAILABILITY

The data that support the findings of this article are not publicly available upon publication because it is not technically feasible and/or the cost of preparing, depositing, and hosting the data would be prohibitive within the terms of this research project. The data are available from the authors upon reasonable request.

[1] C. K. Hong, Z. Y. Ou, and L. Mandel, Measurement of subpicosecond time intervals between two photons by interference, Phys. Rev. Lett. **59**, 2044 (1987).
[2] F. Bouchard, A. Sit, Y. Zhang, R. Fickler, F. M. Miatto, Y. Yao, F. Sciarrino, and E. Karimi, Two-photon interference: The Hong–Ou–Mandel effect, Rep. Prog. Phys. **84**, 012402 (2021).
[3] P. Kok, W. J. Munro, K. Nemoto, T. C. Ralph, J. P. Dowling, and G. J. Milburn, Linear optical quantum computing with photonic qubits, Rev. Mod. Phys. **79**, 135 (2007).
[4] M. B. Nasr, B. E. A. Saleh, A. V. Sergienko, and M. C. Teich, Demonstration of dispersion-canceled quantum-optical coherence tomography, Phys. Rev. Lett. **91**, 083601 (2003).
[5] B. Ndagano, H. Defienne, D. Branford, Y. D. Shah, A. Lyons, N. Westerberg, E. M. Gauger, and D. Faccio, Quantum microscopy based on Hong–Ou–Mandel interference, Nat. Photon. **16**, 384 (2022).
[6] X.-M. Hu, Y. Guo, B.-H. Liu, C.-F. Li, and G.-C. Guo, Progress in quantum teleportation, Nat. Rev. Phys. **5**, 339 (2023).
[7] W. T. M. Irvine, A. L. Linares, M. J. A. de Dood, and D. Bouwmeester, Optimal quantum cloning on a beam splitter, Phys. Rev. Lett. **92**, 047902 (2004).
[8] E. Nagali, L. Sansoni, F. Sciarrino, F. De Martini, L. Marrucci, B. Piccirillo, E. Karimi, and E. Santamato, Optimal quantum cloning of orbital angular momentum photon qubits through Hong–Ou–Mandel coalescence, Nat. Photon. **3**, 720 (2009).
[9] F. Bouchard, R. Fickler, R. W. Boyd, and E. Karimi, High-dimensional quantum cloning and applications to quantum hacking, Sci. Adv. **3**, e1601915 (2017).
[10] F. Graffitti, J. Kelly-Massicotte, A. Fedrizzi, and A. M. Brańczyk, Design considerations for high-purity heralded single-photon sources, Phys. Rev. A **98**, 053811 (2018).
[11] C. H. Bennett, G. Brassard, C. Crépeau, R. Jozsa, A. Peres, and W. K. Wootters, Teleporting an unknown quantum state via dual classical and Einstein-Podolsky-Rosen channels, Phys. Rev. Lett. **70**, 1895 (1993).
[12] H.-S. Zhong, H. Wang, Y.-H. Deng, M.-C. Chen, L.-C. Peng, Y.-H. Luo, J. Qin, D. Wu, X. Ding, Y. Hu *et al.*, Quantum computational advantage using photons, Science **370**, 1460 (2020).
[13] H.-S. Zhong, Y.-H. Deng, J. Qin, H. Wang, M.-C. Chen, L.-C. Peng, Y.-H. Luo, D. Wu, S.-Q. Gong, H. Su *et al.*, Phase-programmable Gaussian boson sampling using stimulated squeezed light, Phys. Rev. Lett. **127**, 180502 (2021).
[14] Q. Zhan, Cylindrical vector beams: From mathematical concepts to applications, Adv. Opt. Photon. **1**, 1 (2009).
[15] A. Bouhelier, M. Beversluis, A. Hartschuh, and L. Novotny, Near-field second-harmonic generation induced by local field enhancement, Phys. Rev. Lett. **90**, 013903 (2003).
[16] W. Chen and Q. Zhan, Numerical study of an apertureless near field scanning optical microscope probe under radial polarization illumination, Opt. Express **15**, 4106 (2007).
[17] Y. Kozawa and S. Sato, Optical trapping of micrometer-sized dielectric particles by cylindrical vector beams, Opt. Express **18**, 10828 (2010).
[18] H. Moradi, V. Shahabadi, E. Madadi, E. Karimi, and F. Hajizadeh, Efficient optical trapping with cylindrical vector beams, Opt. Express **27**, 7266 (2019).
[19] R. Dorn, S. Quabis, and G. Leuchs, Sharper focus for a radially polarized light beam, Phys. Rev. Lett. **91**, 233901 (2003).
[20] H. Wang, L. Shi, B. Lukyanchuk, C. Sheppard, and C. T. Chong, Creation of a needle of longitudinally polarized light in vacuum using binary optics, Nat. Photon. **2**, 501 (2008).
[21] C. E. R. Souza, C. V. S. Borges, A. Z. Khoury, J. A. O. Huguenin, L. Aolita, and S. P. Walborn, Quantum key distribution without a shared reference frame, Phys. Rev. A **77**, 032345 (2008).
[22] G. Vallone, V. D'Ambrosio, A. Sponselli, S. Slussarenko, L. Marrucci, F. Sciarrino, and P. Villoresi, Free-space quantum key distribution by rotation-invariant twisted photons, Phys. Rev. Lett. **113**, 060503 (2014).
[23] K. Sakai and S. Noda, Optical trapping of metal particles in doughnut-shaped beam emitted by photonic-crystal laser, Electron. Lett. **43**, 107 (2007).
[24] E. Miyai, K. Sakai, T. Okano, W. Kunishi, D. Ohnishi, and S. Noda, Lasers producing tailored beams, Nature (London) **441**, 946 (2006).
[25] S. Iwahashi, Y. Kurosaka, K. Sakai, K. Kitamura, N. Takayama, and S. Noda, Higher-order vector beams produced by photonic-crystal lasers, Opt. Express **19**, 11963 (2011).
[26] L. Marrucci, C. Manzo, and D. Paparo, Optical spin-to-orbital angular momentum conversion in inhomogeneous anisotropic media, Phys. Rev. Lett. **96**, 163905 (2006).
[27] F. Cardano, E. Karimi, S. Slussarenko, L. Marrucci, C. de Lisio, and E. Santamato, Polarization pattern of vector vortex beams generated by q-plates with different topological charges, Appl. Opt. **51**, C1 (2012).
[28] F. Cardano, E. Karimi, L. Marrucci, C. de Lisio, and E. Santamato, Generation and dynamics of optical beams with polarization singularities, Opt. Express **21**, 8815 (2013).
[29] C. Maurer, A. Jesacher, S. Fürhapter, S. Bernet, and M. Ritsch-Marte, Tailoring of arbitrary optical vector beams, New J. Phys. **9**, 78 (2007).
[30] E. Karimi, J. Leach, S. Slussarenko, B. Piccirillo, L. Marrucci, L. Chen, W. She, S. Franke-Arnold, M. J. Padgett, and E. Santamato, Spin-orbit hybrid entanglement of photons and quantum contextuality, Phys. Rev. A **82**, 022115 (2010).
[31] R. Fickler, M. Krenn, R. Lapkiewicz, S. Ramelow, and A. Zeilinger, Real-time imaging of quantum entanglement, Sci. Rep. **3**, 1914 (2013).
[32] V. D'Ambrosio, G. Carvacho, F. Graffitti, C. Vitelli, B. Piccirillo, L. Marrucci, and F. Sciarrino, Entangled vector vortex beams, Phys. Rev. A **94**, 030304(R) (2016).
[33] F. Graffitti, V. D'Ambrosio, M. Proietti, J. Ho, B. Piccirillo, C. de Lisio, L. Marrucci, and A. Fedrizzi, Hyperentanglement in structured quantum light, Phys. Rev. Res. **2**, 043350 (2020).
[34] X. Gao, Y. Zhang, A. D'Errico, A. Sit, K. Heshami, and E. Karimi, Full spatial characterization of entangled structured photons, Phys. Rev. Lett. **132**, 063802 (2024).
[35] C. Schiano, B. Sephton, R. Aiello, F. Graffitti, N. Lal, A. Chiuri, S. Santoro, L. S. Amato, L. Marrucci, C. de Lisio *et al.*, Engineering quantum states from a spatially structured quantum eraser, Sci. Adv. **10**, eadm9278 (2024).
[36] See Supplemental Material at http://link.aps.org/supplemental/10.1103/dcxb-ql1r for details on the experimental setup, complete derivation of the output state, and additional experimental results obtained for different input settings.
[37] E. Karimi, B. Piccirillo, L. Marrucci, and E. Santamato, Light propagation in a birefringent plate with topological charge, Opt. Lett. **34**, 1225 (2009).

[38] S. Slussarenko, A. Murauski, T. Du, V. Chigrinov, L. Marrucci, and E. Santamato, Tunable liquid crystal q-plates with arbitrary topological charge, Opt. Express **19**, 4085 (2011).

[39] E. Karimi, B. Piccirillo, L. Marrucci, and E. Santamato, Light propagation in a birefringent plate with topological charge, Opt. Lett. **32**, 3053 (2007).

[40] B. Piccirillo, V. D'Ambrosio, S. Slussarenko, L. Marrucci, and E. Santamato, Photon spin-to-orbital angular momentum conversion via an electrically tunable q-plate, Appl. Phys. Lett. **97**, 241104 (2010).

[41] A. Nomerotski, Imaging and time stamping of photons with nanosecond resolution in Timepix based optical cameras, Nucl. Instrum. Methods Phys. Res. Sect. A **937**, 26 (2019).

[42] A. Nomerotski, M. Chekhlov, D. Dolzhenko, R. Glazenborg, B. Farella, M. Keach, R. Mahon, D. Orlov, and P. Svihra, Intensified Tpx3Cam, a fast data-driven optical camera with nanosecond timing resolution for single photon detection in quantum applications, J. Instrum. **18**, C01023 (2023).

[43] D. F. V. James, P. G. Kwiat, W. J. Munro, and A. G. White, Measurement of qubits, Phys. Rev. A **64**, 052312 (2001).

[44] H. Larocque, J. Gagnon-Bischoff, F. Bouchard, R. Fickler, J. Upham, R. W. Boyd, and E. Karimi, Arbitrary optical wavefront shaping via spin-to-orbit coupling, J. Opt. **18**, 124002 (2016).

[45] A. D'Errico, F. Cardano, M. Maffei, A. Dauphin, R. Barboza, C. Esposito, B. Piccirillo, M. Lewenstein, P. Massignan, and L. Marrucci, Two-dimensional topological quantum walks in the momentum space of structured light, Optica **7**, 108 (2020).

[46] P. G. Kwiat, E. Waks, A. G. White, I. Appelbaum, and P. H. Eberhard, Ultrabright source of polarization-entangled photons, Phys. Rev. A **60**, R773 (1999).

[47] A. K. Ekert, Quantum cryptography based on Bell's theorem, Phys. Rev. Lett. **67**, 661 (1991).

[48] Y.-B. Sheng, F.-G. Deng, and G. L. Long, Complete hyperentangled-Bell-state analysis for quantum communication, Phys. Rev. A **82**, 032318 (2010).

[49] N. Hauser, M. J. Bayerbach, S. E. D'Aurelio, R. Weber, M. Santandrea, S. P. Kumar, I. Dhand, and S. Barz, Boosted Bell-state measurements for photonic quantum computation, npj Quantum Inf. **11**, 41 (2025).

[50] C. H. Bennett, D. P. DiVincenzo, J. A. Smolin, and W. K. Wootters, Mixed-state entanglement and quantum error correction, Phys. Rev. A **54**, 3824 (1996).

[51] P. Mazurek, M. Farkas, A. Grudka, M. Horodecki, and M. Studziński, Quantum error-correction codes and absolutely maximally entangled states, Phys. Rev. A **101**, 042305 (2020).

[52] H.-S. Zhong, Y. Li, W. Li, L.-C. Peng, Z.-E. Su, Y. Hu, Y.-M. He, X. Ding, W. Zhang, H. Li, L. Zhang *et al.*, 12-photon entanglement and scalable scattershot boson sampling with optimal entangled-photon pairs from parametric downconversion, Phys. Rev. Lett. **121**, 250505 (2018).

[53] D. Cogan, Z.-E. Su, O. Kenneth, and D. Gershoni, Deterministic generation of indistinguishable photons in a cluster state, Nat. Photon. **17**, 324 (2023).

[54] J. O'Sullivan, K. Reuer, A. Grigorev, X. Dai, A. Hernández-Antón, M. H. Muñoz-Arias, C. Hellings, A. Flasby, D. C. Zanuz, J.-C. Besse *et al.*, Deterministic generation of a 20-qubit two-dimensional photonic cluster state, Nature Commun. **16**, 5505 (2025).

[55] V. Vidyapin, Y. Zhang, D. England, and B. Sussman, Characterisation of a single photon event camera for quantum imaging, Sci. Rep. **13**, 1009 (2023).

[56] B. G. Oripov, D. S. Rampini, J. Allmaras, M. D. Shaw, S. W. Nam, B. Korzh, and A. N. McCaughan, A superconducting nanowire single-photon camera with 400,000 pixels, Nature (London) **622**, 730 (2023).

Engineering qubit dynamics in open systems with photonic synthetic lattices

Francesco Di Colandrea,[1,2,*] Tareq Jaouni,[1] John Grace,[1,3] Dilip Paneru,[1] Mirko Arienzo,[4]
Alessio D'Errico,[1,5] and Ebrahim Karimi[1,5,6]
[1]*Nexus for Quantum Technologies, University of Ottawa, Ottawa, Ontario K1N 5N6, Canada*
[2]*Dipartimento di Fisica "Ettore Pancini", Università degli Studi di Napoli Federico II,*
Complesso Universitario di Monte Sant'Angelo, Via Cintia, 80126 Napoli, Italy
[3]*Department of Physics, McGill University, Montreal, Quebec H3A 0G4, Canada*
[4]*Institute for Quantum Inspired and Quantum Optimization, Hamburg University of Technology, Hamburg 21079, Germany*
[5]*National Research Council of Canada, 100 Sussex Drive, Ottawa, Ontario K1A 0R6, Canada*
[6]*Institute for Quantum Studies, Chapman University, Orange, California 92866, USA*

(Received 18 December 2024; accepted 11 May 2025; published 6 June 2025)

The evolution of a quantum system interacting with an environment can be described as a unitary process acting on both the system and the environment. In this framework, the system's evolution can be predicted by tracing out the environmental degrees of freedom. Here, we establish a precise mapping between the global unitary dynamics and the quantum operation involving the system, wherein the system is a single qubit, and the environment is modeled as a discrete lattice space. This approach enables the implementation of arbitrary noise operations on single-polarization qubits using a minimal set of three liquid-crystal metasurfaces, whose transverse distribution of the optic axes can be patterned to reproduce the target process. We experimentally validate this method by simulating common noise processes, such as phase errors and depolarization. Besides providing a practical solution for quantum state purification, this work demonstrates a versatile approach for the simulation of open qubit dynamics, with potential implications for quantum error correction and environment-induced quantum phase transitions.

DOI: 10.1103/PhysRevResearch.7.023236

I. INTRODUCTION

The majority of experiments in quantum mechanics require, to some extent, accounting for the influence of external effects over which the experimenter has limited knowledge or control. In this sense, any realistic quantum system should be regarded as an open system. Exposing a quantum system to an environment causes decoherence and dissipation, the main obstacle for hardware implementations of quantum computation protocols in the noisy intermediate-scale quantum (NISQ) era [1,2]. Surprisingly, decoherence can also represent a powerful resource in dissipation-driven quantum computation and state-engineering protocols [3,4].

From a quantum thermodynamics perspective, the interaction of one or few quantum bits with an environment involves exchanges of energy, work, and information [5–7]. Engineering qubit-environment interactions is thus a pivotal task for devising energy transfer processes, such as quantum heat engines [8–12], quantum batteries [13–16], and quantum refrigerators [17–20].

The capability of simulating these interactions also allows for addressing fundamental questions, for instance, in the context of emerging developments in understanding the interplay between geometric phases and quantum back action [21], wherein the variation of the geometrical phase has been demonstrated to be connected with the system-environment coupling strength in a topological fashion [22].

In recent years, it has also become common to describe open systems in terms of non-Hermitian processes, wherein the system evolution is dictated by a Hamiltonian operator that admits a complex spectrum, accounting for the possibility of gains and losses in subsets of modes [23–25]. Non-Hermitian dynamics have demonstrated a wide variety of applications in quantum physics [26–30] and photonics [31–33], in particular when exploiting phenomena related to the topological properties of the Hamiltonian [34–36]. The connection between the description of open systems as non-Hermitian processes and via master equations has been established [37], proving that it is generally possible to reduce the problem to a set of Kraus operators acting on the principal system [38].

Experimental setups where open dynamics can be simulated have recently been demonstrated. For example, the optical simulator presented in Ref. [39] uses a spatial light modulator to alter the polarization qubit of single photons in a programmable way, leveraging spatial multiplexing of the spectral degree of freedom to average over multiple realizations of the noisy channel in a single shot. On the other hand, the experiment reported in Ref. [40] demonstrates the first simulation of open dynamics with continuous variables, assessed by measuring the spectral density [41] of the environmental coupling and the quantum non-Markovianity [42] of the process, with reconfigurability given by the possibility of rearranging complex networks of harmonic oscillators in various tailored structures [43]. However, these studies only focused on the reduced dynamics of the system, without establishing a clear connection with the global (system-environment) unitary. In this work, we demonstrate a step forward in this direction. We realize a platform where arbitrary sets of Kraus operators acting on a single qubit can be implemented, thus allowing for the simulation of any noise operator. Our strategy is based on coupling the qubit with an environment modeled as an infinite, discrete set of modes, visualized as a one-dimensional (1D) lattice space. By leveraging translational invariance, we derive an effective relation between the global unitary and the target set of Kraus operators. Once such a unitary is identified, it can be implemented in a compact photonic circuit consisting of a stack of three patterned wave plates [44]. In so doing, we can implement arbitrary operations on light polarization, encoding the qubit, by coupling it with the transverse spatial degree of freedom. This method is validated in a proof-of-principle experiment where we simulate common noise processes with different strengths.

Our results demonstrate that this approach could also be employed to benchmark quantum thermal machines' functionality and test the fundamental properties of open quantum systems.

II. RESULTS

The dynamics of a quantum system (here, a single qubit) is most generally described by a quantum channel $\mathcal{N}$, describing the noisy evolution of the system, that maps an input state ρ_{in} into the final state $\rho_{\text{f}} = \mathcal{N}(\rho_{\text{in}})$. Mathematically, $\mathcal{N}$ corresponds to a completely positive, trace-preserving map, which can be specified by a set of Kraus operators $\{A_k\}$ such that

$$\rho_{\text{f}} = \sum_k A_k \rho_{\text{in}} A_k^{\dagger}, \tag{1}$$

under the trace-preserving condition $\sum_k A_k A_k^{\dagger} = \sigma_0$, where σ_0 is the 2×2 identity operator [38]. An equivalent description is to consider the qubit as a system S interacting with an environment E. The qubit and environment define a closed system $\Omega = S + E$, described by a pure state undergoing a unitary evolution [see Fig. 1(a)]. This corresponds to choosing a *purification* of the system S. The choice of purification (or, equivalently, of the environment E) is not unique [38]. We will show in the following that it is always possible to model the environment as an infinite-dimensional Hilbert space $\mathcal{H}_E$ spanned by a discrete set of states $\{|m\rangle\}$, with $m \in \mathbb{Z}$. These states can be interpreted as the eigenstates of the position operator on an infinite 1D lattice. This suggests that the system-environment interaction occurs in the form of a translation-invariant unitary operator U. Accordingly, the latter can be block-diagonalized in the reciprocal space

$$U = \int_0^{2\pi} \mathrm{d}q\, \mathcal{U}(q) |q\rangle\langle q|, \tag{2}$$

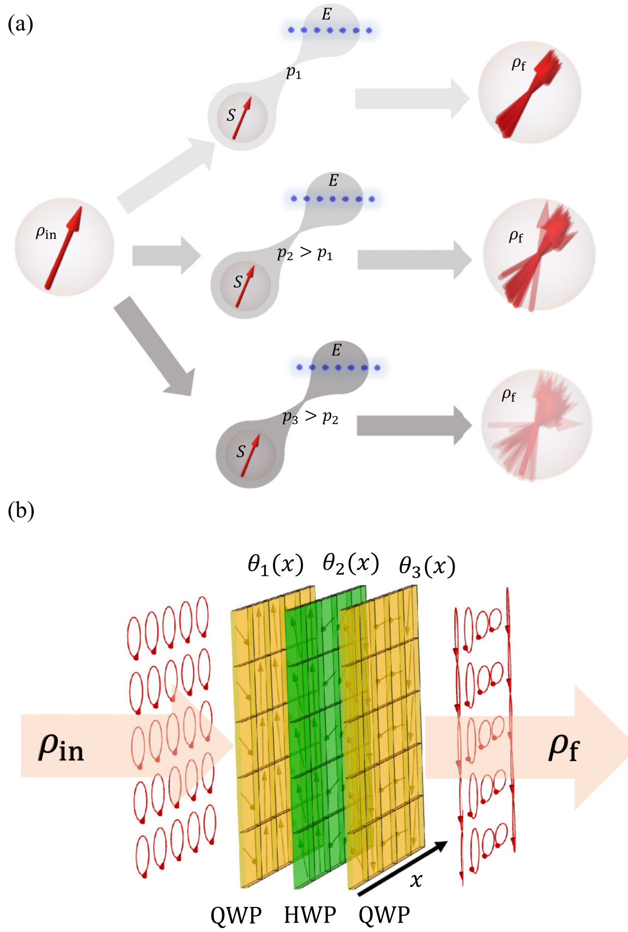

FIG. 1. Concept of the experiment. (a) A qubit initialized in a pure state ρ_{in} interacts with an external environment (E) featuring discrete lattice symmetry. The interaction strength is controlled by the parameter p, which can be tuned to produce different output mixed states ρ_{f}. Larger values of p imply that the final state is delocalized over a larger number of lattice sites, leading to a reduction in the qubit state purity. (b) Our approach relies on the use of three liquid-crystal metasurfaces, each characterized by an optic-axis pattern $\theta_i(x)$, where x encodes the position reciprocal coordinate via the mapping $x = \Lambda q/(2\pi)$, with Λ a characteristic spatial period. In this implementation, the qubit is encoded into light polarization and the metasurfaces implement the system-environment interaction as a polarization-position coupling.

where $|q\rangle := \sum_m \exp(iqm)|m\rangle/\sqrt{2\pi}$ is a quasimomentum eigenstate and $\mathcal{U}(q)$ is an SU(2) operator that acts on the Hilbert space of the qubit $\mathcal{H}_S$.

Without loss of generality, we can assume that the environment is initialized in a pure state $\rho_{E,\text{in}} = |m=0\rangle\langle m=0|$, so that the global initial state is $\rho_{\Omega,\text{in}} = \rho_{S,\text{in}} \otimes \rho_{E,\text{in}}$. This assumption is typically verified in most experimental settings. Applying U to the input state, we obtain the following:

$$\begin{aligned}\rho_{\Omega,\text{f}} &= U \rho_{\Omega,\text{in}} U^{\dagger} \\ &= \frac{1}{2\pi} \iint \mathrm{d}q\, \mathrm{d}q'\, \mathcal{U}(q) \rho_{S,\text{in}} \mathcal{U}^{\dagger}(q') |q\rangle\langle q'|,\end{aligned} \tag{3}$$

where the integrals are taken over the interval $[0, 2\pi]$. After the interaction, the state of the qubit can be retrieved by taking the partial trace of the evolved density operator with respect to the environment in the quasimomentum representation:

$$\begin{aligned}\rho_{\mathrm{f}} = \mathrm{tr}_E(\rho_{\Omega,\mathrm{f}}) &= \int_0^{2\pi} \mathrm{d}q\, \langle q|\rho_{\Omega,\mathrm{f}}|q\rangle \\ &= \frac{1}{2\pi}\int_0^{2\pi} \mathrm{d}q\,\mathcal{U}(q)\rho_{\mathrm{in}}\,\mathcal{U}^\dagger(q),\end{aligned} \tag{4}$$

where the system label S has been omitted. Our goal is to design $\mathcal{U}(q)$ such that the evolved density operator ρ_{f} of the qubit is equivalent to the outcome of a target noise operation $\mathcal{N}$. Mathematically, this corresponds to solving

$$\frac{1}{2\pi}\int_0^{2\pi} \mathrm{d}q\,\mathcal{U}(q)\rho_{\mathrm{in}}\,\mathcal{U}^\dagger(q) = \sum_k A_k\rho_{\mathrm{in}}A_k^\dagger, \tag{5}$$

under the constraint that $\mathcal{U}(q)$ is an SU(2) matrix at each q.

To this aim, we decompose $\mathcal{U}(q)$ and each Kraus operator A_k into linear combinations of the identity and Pauli matrices $(\sigma_1, \sigma_2, \sigma_3)$, a set of complete basis for the 2×2 matrices:

$$\begin{aligned}\mathcal{U}(q) &= u_0(q)\sigma_0 - i(u_1(q)\sigma_1 + u_2(q)\sigma_2 + u_3(q)\sigma_3),\\ A_k &= c_0^{(k)}\sigma_0 - i\big(c_1^{(k)}\sigma_1 + c_2^{(k)}\sigma_2 + c_3^{(k)}\sigma_3\big),\end{aligned} \tag{6}$$

which yields [see Eq. (5)]

$$\sum_{i,j}\frac{1}{2\pi}\int_0^{2\pi} \mathrm{d}q\, u_i(q)u_j(q)\sigma_i\sigma_j = \sum_{i,j}\sum_k c_i^{(k)}c_j^{*(k)}\sigma_i\sigma_j, \tag{7}$$

where $*$ denotes complex conjugation. Equation (7) corresponds to a system of 16 equations of the following form:

$$\frac{1}{2\pi}\int_0^{2\pi} \mathrm{d}q\, u_i(q)u_j(q) = \sum_k c_i^{(k)}c_j^{*(k)}, \tag{8}$$

for $\{i, j\} = 0, 1, 2, 3$, that can be solved numerically for the coefficients $\{u_i(q)\}$ under the unitary constraint

$$u_0^2(q) + u_1^2(q) + u_2^2(q) + u_3^2(q) = 1, \tag{9}$$

for all $q \in [0, 2\pi]$ (see Methods for details). Importantly, the solution holds for any qubit initialization; therefore, we engineer an effective simulation of the target noise.

Once the global unitary has been identified, an experimental setting can be created to implement such an operator. In our photonic setup, the qubit is encoded into light polarization, while the environment state $|m\rangle$ corresponds to an optical mode carrying m units of transverse momentum $\Delta k_\perp = 2\pi/\Lambda$, where Λ is a characteristic length comparable with the beam radius. This corresponds to mapping the quasimomentum coordinate into the photon transverse position: $q = 2\pi x/\Lambda$ [45]. With this encoding scheme, arbitrary unitary operators in the form of Eq. (2) can be simulated using a minimal stack of three patterned wave plates [see Fig. 1(b)]. This technique has been introduced in Ref. [44] as a compact solution to simulate ultralong quantum walks. It is well known that a sequence of a half-wave plate (HWP) sandwiched between two quarter-wave plates (QWPs) can implement an arbitrary polarization transformation by adjusting the orientation of the optic axes θ_i of each wave plate [46]. In the circular polarization basis, where $|L\rangle := (1, 0)^T$ and $|R\rangle := (0, 1)^T$ are the left and right circular polarization states, respectively, and T stands for transpose, the general transformation matrix associated with a wave plate can be written as

$$W_i(\theta_i) = \cos\left(\frac{\delta_i}{2}\right)\sigma_0 + i\sin\left(\frac{\delta_i}{2}\right)(\cos(2\theta_i)\sigma_1 + \sin(2\theta_i)\sigma_2), \tag{10}$$

where the subscript $i = 1, 2, 3$ labels individual wave plates, $\delta_1 = \delta_3 = \pi/2$ are the optical retardations of the QWPs W_1 and W_3, $\delta_2 = \pi$ is the retardation of the HWP W_2, and θ_i are the optic-axis orientation angles. The required patterns $\theta_i(x)$ can be determined by solving $W_3W_2W_1 = \mathcal{U}$ at each q (see Methods). Patterned wave plates are fabricated as electrically tunable nematic liquid-crystal metasurfaces, with the optic axis locally patterned via a well-established photoalignment technique [47].

We demonstrate our approach by fabricating stacks of plates simulating different instances of quantum noise, specifically, phase flip, bit flip, bit-phase flip, and depolarization channels. These are defined by the following sets of Kraus operators. For the first three channels, $A_0 = \sqrt{1-p}\,\sigma_0$ and $A_1 = \sqrt{p}\,\sigma_i$, with $i = 1, 2, 3$ for bit flip, bit-phase flip, and phase flip, respectively. The depolarization channel is instead characterized by the Kraus operators $\{A_0, A_1, A_2, A_3\}$, where $A_0 = \sqrt{1-p}\,\sigma_0$ and $A_i = \sqrt{p/3}\,\sigma_i$ [38]. Each channel has been implemented for three values of the system-environment coupling parameter, $p = 1/8,\ 1/4,\ 1/2$, corresponding to the weak, intermediate, and strong interaction regimes, respectively [48]. The coupling parameter physically represents the probability that a certain Pauli gate is applied to the qubit system. Intuitively, higher values of p are associated with processes in which a larger number of lattice sites are occupied, each with a different polarization. This results in greater uncertainty in the definition of the final qubit state, thereby leading to a reduction in its purity.

The experimental setup is outlined in Fig. 2(a). An 810 nm laser beam crosses a state-preparation stage consisting of a polarizer (P), a half-wave plate (H), and a quarter-wave plate (Q). For each noise realization, we choose as input states $|L\rangle$, $|H\rangle$, and $|D\rangle$, where $|H\rangle = (|L\rangle + |R\rangle)/\sqrt{2}$ and $|D\rangle = (|L\rangle + i|R\rangle)/\sqrt{2}$ are the horizontal and diagonal polarization states, respectively. The noise $\mathcal{N}$ is implemented by three liquid-crystal metasurfaces $W_1 - W_2 - W_3$. The output qubit-polarization state is analyzed with a sequence Q–H–P, measuring the transmitted intensity with a power-meter detector (D). This allows us to retrieve the three Stokes parameters providing the representation of the qubit state on the Bloch sphere [49]. The optic-axis patterns of the metasurfaces used to simulate phase flip, bit flip, and bit-phase flip are plotted in Fig. 2(b). These channels feature the same Kraus operators decomposition up to a basis rotation that can be implemented with uniform wave plates, and can therefore be simulated with the same sets of plates. The patterns for the depolarization channels are provided in Fig. 2(c). It is evident that the complexity of the patterns increases with the complexity

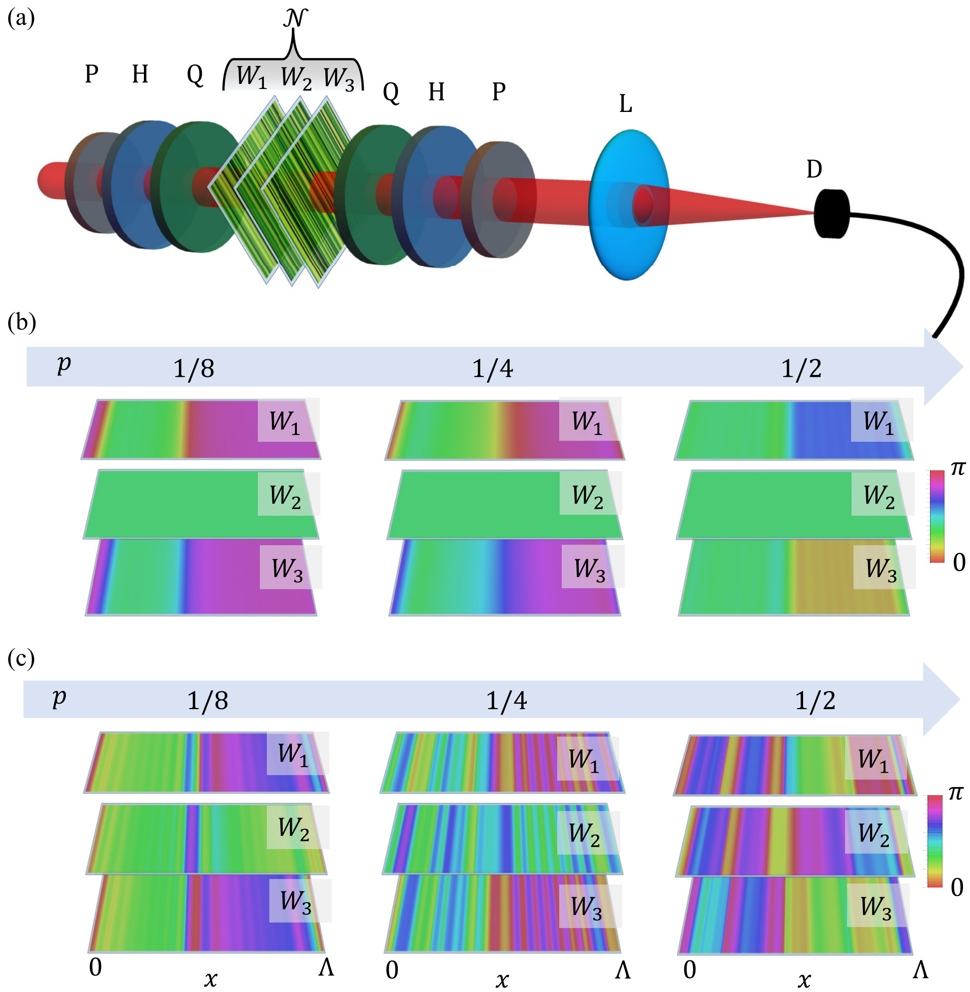

FIG. 2. Experimental setup. (a) Sketch of the experimental setup. P: polarizer, H: half-wave plate, Q: quarter-wave plate, L: lens, D: detector. The noise $\mathcal{N}$ is implemented by a sequence of three liquid-crystal metasurfaces $W_1 - W_2 - W_3$. In our experiment, we set $\Lambda = 2.5$ mm. The input beam waist was $w_0 \simeq \Lambda$, corresponding to a pure localized environment. (b) Optic-axis patterns of the plates used for phase flip, bit flip, and bit-phase flip, for different values of the coupling parameter p. (c) Patterns for the depolarization channel. The hue color coding indicates the orientation $\theta(x)$ of the liquid-crystal optic axis on the metasurfaces plane.

of the simulated interaction. This is due to higher-frequency modulations required to couple the qubit to a larger number of lattice sites.

The experimental results are illustrated in Fig. 3, where we plot the measured Stokes parameters [see Fig. 3(a)] and the corresponding trajectories [see Fig. 3(b)] of the qubit states on the Bloch sphere as a function of the noise level p. Deviations from the theory are systematic errors due to imperfect alignment of the plates and fabrication defects, in agreement with Monte Carlo simulations whose results are reported as error bands around the theoretical lines in Fig. 3(a). Overall, the average fidelity $\mathcal{F} = \mathrm{Tr}(\sqrt{\sqrt{\rho_{\mathrm{th}}}\rho_{\mathrm{exp}}\sqrt{\rho_{\mathrm{th}}}})^2$ between the measured states ρ_{exp} and the expected ones ρ_{th} is always above 98%, proving that our devices reproduce the target channels with high accuracy. The results for phase flip, bit flip, and bit-phase flip show that the action of the noise keeps unaltered the qubit states initialized in the eigenstate of A_1, while it pushes other inputs toward the origin of the Bloch sphere. The depolarization channel displays similar behavior for all pure input states [38].

III. CONCLUSIONS

In this work, we demonstrated a general approach for engineering noise operations on a qubit system, based on suitably coupling the qubit with a lattice-like environment. We provided a systematic procedure for constructing a global unitary operator corresponding to the desired process on the qubit state. In our photonic demonstration, light polarization played the role of a qubit, and the environment was encoded into a set of transverse modes, with the interaction occurring in the form of a space-dependent polarization transformation, engineered via liquid-crystal metasurfaces. The patterns of the metasurfaces have been inverse-designed to simulate typical noise operations in different interaction regimes.

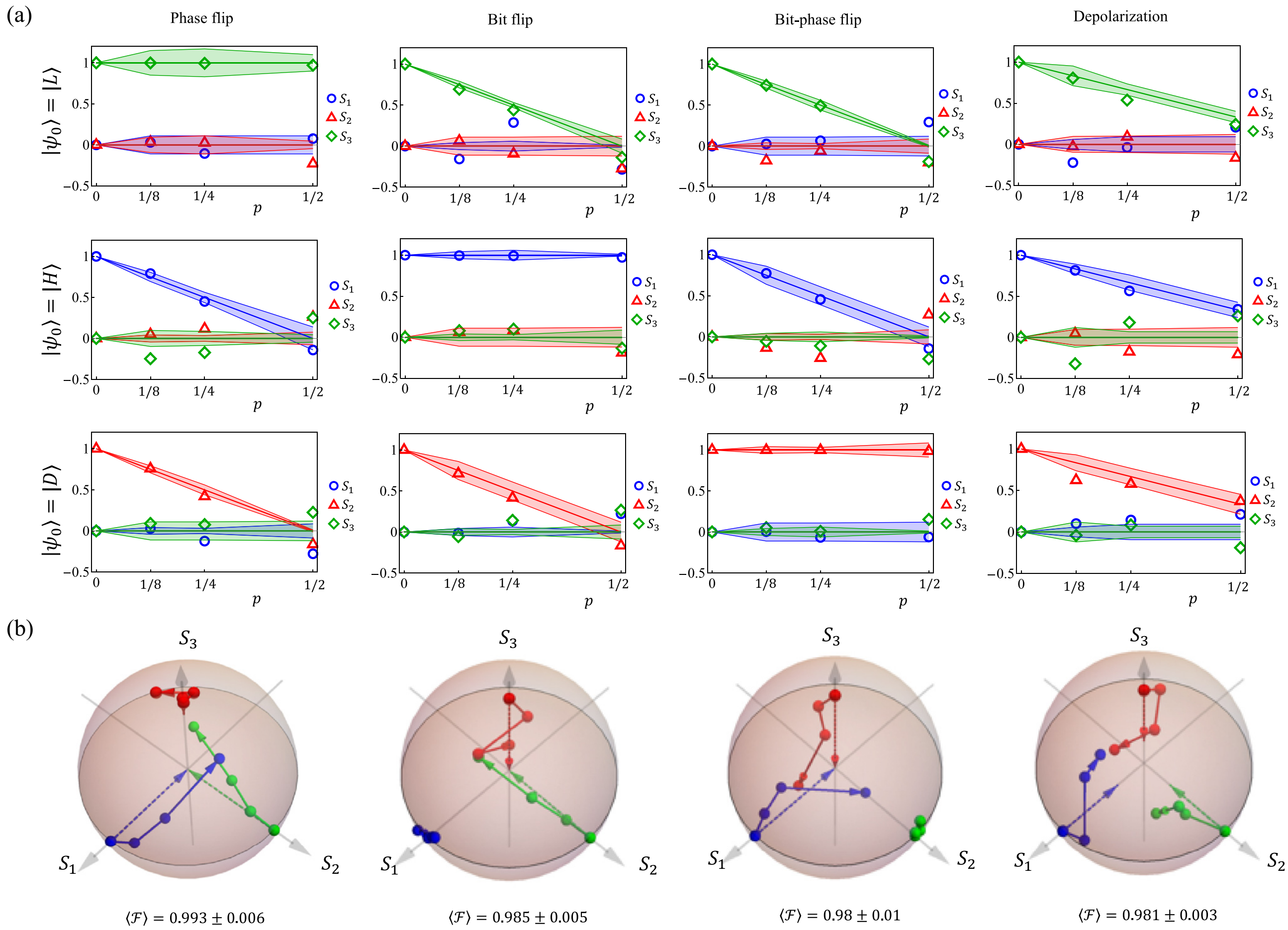

FIG. 3. Experimental results. (a) Output qubit states in terms of the measured Stokes parameters S_1, S_2, S_3 (empty markers), with varying coupling strength p. The $p = 0$ case is included as a guide and corresponds to the nominal input state. Continuous lines show the theoretical trends, with error bands representing confidence intervals accounting for experimental imperfections. The latter have been evaluated with Monte Carlo simulations, where the relative alignment of the plates and their optical retardation have been considered as Gaussian random variables with a 5% standard deviation, estimated through direct measurements on fabricated samples. The bands are the standard deviations on the Stokes parameters extracted from 100 realizations of simulated experiments. Results are shown for the processes of phase flip, bit flip, bit-phase flip, and depolarization, with three different pure input states, $|H\rangle$, $|D\rangle$, and $|L\rangle$, respectively oriented along the S_1, S_2, and S_3 axis of the Bloch sphere. (b) Qubit trajectories (as function of p) on the Bloch sphere. Dashed arrows are the theoretical predictions, while joined spheres are the experimental results. Different colors correspond to different input states: $|H\rangle$ (blue), $|D\rangle$ (green), and $|L\rangle$ (red). In the insets, we report the average fidelities between the reconstructed and expected states.

Our findings pave the way for innovative solutions for studying open quantum systems. While in this work we focused on standard, well-known examples of quantum noise, our platform can readily be adapted to simulate arbitrary qubit-environment interactions. Potential applications involve the simulations of quantum machines, such as quantum refrigerators, protocols of quantum thermodynamics, chiral dynamics in open systems, as well as geometric-phase and topological effects in non-Hermitian evolutions. Furthermore, such controlled and high-fidelity simulations of common forms of noise could foster the development of effective strategies for quantum error correction [50] or alternative protocols of dissipation-driven quantum computation [3]. In the future, the trace-preserving assumption could be relaxed by post-selecting only a subset of lattice sites following the qubit-environment interaction. Another interesting prospect concerns the generalization of our scheme to a larger number of qubits, where the emerging concepts of local passivity [51] and ergotropy [52,53] could be experimentally observed. Nevertheless, the same setup could still be used to investigate the effects of known single-qubit noises on single- and multi-mode entangled states, monitoring how different noises degrade nonlocal correlations [54]. Conversely, this work could also stimulate theoretical research on environment-assisted quantum process tomography of nonunitary channels [55,56], where one probes the environment to gain information on the (unknown) system dynamics. Finally, by replacing liquid-crystal metasurfaces with spatial light modulators, our setup could be made reconfigurable in real-time, which is an ideal feature for experimentally investigating dynamical phenomena such as environment-induced quantum phase transitions [57,58].

IV. METHODS

A. Numerical optimization

To solve the system of equations given by Eq. (8), we expand each coefficient $\{u_i(q)\}$ in the Fourier basis:

$$u_i(q) = u_i^{(0)} + \sum_{n=1}^{N} \left(u_{ic}^{(n)} \cos(nq) + u_{is}^{(n)} \sin(nq)\right), \quad (11)$$

where N is the maximum number of spatial frequencies which can be tuned. By substituting the decomposition of Eq. (11) into Eq. (8), and performing the corresponding integrals, we obtain a simple relation for the Fourier coefficients:

$$2u_i^{(0)}u_j^{(0)} + \sum_{n=1}^{N} \left(u_{ic}^{(n)}u_{jc}^{(n)} + u_{is}^{(n)}u_{js}^{(n)}\right) = 2\sum_k c_i^{(k)}c_j^{*(k)}, \quad (12)$$

for $\{i, j\} = 0, 1, 2, 3$. The system of equations given by Eq. (12) can be solved numerically, under the unitary constraint $u_0^2(q) + u_1^2(q) + u_2^2(q) + u_3^2(q) = 1$ at each quasi-momentum value. To accomplish this, an iterative solution is adopted. First, we discretize the interval $[0, 2\pi]$ in $Q = 125$ points. This value is chosen to ensure a dense sampling of the spatial period. Then, we numerically minimize the following cost function for the Fourier coefficients:

$$f_1 = \sum_{i,j} \left[2u_i^{(0)}u_j^{(0)} + \sum_{n=1}^{N} \left(u_{ic}^{(n)}u_{jc}^{(n)} + u_{is}^{(n)}u_{js}^{(n)}\right) - 2\sum_k c_i^{(k)}c_j^{*(k)}\right]^2. \quad (13)$$

The solutions of the first minimization routine are used as input guesses for the minimization of a second cost function, expressing the unitary constraint at each (discretized) quasi-momentum value:

$$f_2 = \sum_{i=1}^{Q} \left(u_0^2(q_i) + u_1^2(q_i) + u_2^2(q_i) + u_3^2(q_i) - 1\right)^2. \quad (14)$$

The second minimization output feeds the previous minimization routine for the cost function f_1, and so forth, until the total difference between the optimized coefficients from the two routines is less than 10^{-12} or when the number of iterations reaches $T = 200$, whichever occurs first. This systematically allowed us to minimize both cost functions to values of order $\approx 10^{-12}$, by enforcing only $N = 20$ frequencies. As detailed in the next section, the maximum number of spatial frequencies determines the complexity of the plates to be fabricated, therefore, it is desirable to achieve a solution with a reasonably small number of frequencies.

B. Extracting the metasurfaces' patterns

The nested minimization routines described above output an optimal set of Fourier coefficients for a given noise, which in turn determines the space-dependent unitary operator U in the form of Eq. (2). After the identification $q \leftrightarrow x$, at each transverse position, the operator U implements a polarization rotation $\mathcal{U}(x)$ of an angle χ around the axis $\mathbf{n} = (n_1, n_2, n_3)$:

$$\mathcal{U}(x) = \cos\left(\frac{\chi(x)}{2}\right)\sigma_0 - i\sin\left(\frac{\chi(x)}{2}\right)\mathbf{n}(x)\cdot\boldsymbol{\sigma}, \quad (15)$$

where $\boldsymbol{\sigma} = \{\sigma_1, \sigma_2, \sigma_3\}$, and

$$\chi = 2\arccos u_0; \qquad n_i = \frac{u_i}{\sin\left(\frac{\chi}{2}\right)}, \quad (16)$$

for $i = 1, 2, 3$ [cf. Eq. (6)].

The optical sequence of three liquid-crystal metasurfaces $\mathcal{L} = W_3(\theta_3)W_2(\theta_2)W_1(\theta_1)$ can be analogously decomposed as

$$\mathcal{L}(x) = \ell_0(x)\sigma_0 - i(\ell_1(x)\sigma_1 + \ell_2(x)\sigma_2 + \ell_3(x)\sigma_3), \quad (17)$$

where

$$\begin{aligned} \ell_0 &= -\cos\alpha\cos\beta, \\ \ell_1 &= -\sin\beta\sin\gamma, \\ \ell_2 &= \sin\beta\cos\gamma, \\ \ell_3 &= \sin\alpha\cos\beta, \end{aligned} \quad (18)$$

with $\alpha = \theta_1 - \theta_3$, $\beta = \theta_1 - 2\theta_2 + \theta_3$, and $\gamma = \theta_1 + \theta_3$. The dependence on the transverse coordinate x is omitted for ease of notation. Imposing $\mathcal{U} = \mathcal{L}$ at each transverse position yields

$$\cos\alpha\cos\beta = -\cos\frac{\chi}{2}, \quad (19a)$$

$$\sin\beta\sin\gamma = -\sin\frac{\chi}{2}\sin\vartheta\cos\varphi, \quad (19b)$$

$$\sin\beta\cos\gamma = \sin\frac{\chi}{2}\sin\vartheta\sin\varphi, \quad (19c)$$

$$\sin\alpha\cos\beta = \sin\frac{\chi}{2}\cos\vartheta, \quad (19d)$$

where we used the spherical parametrization of the vector $\mathbf{n}$: $n_1 = \sin\vartheta\cos\varphi$, $n_2 = \sin\vartheta\sin\varphi$, and $n_3 = \cos\vartheta$.

From Eqs. (19b) and (19c), it follows

$$\gamma = \varphi - \frac{\pi}{2}. \quad (20)$$

Two sets of solutions are found from Eqs. (19a) and (19d):

$$\begin{aligned} \alpha_1 &= \mathrm{atan2}\left(-\sin\frac{\chi}{2}\cos\vartheta, \cos\frac{\chi}{2}\right) \\ \beta_1 &= \mathrm{atan2}\left(\sin\frac{\chi}{2}\sin\vartheta, -\sqrt{1 - \sin^2\frac{\chi}{2}\sin^2\vartheta}\right) \\ \gamma_1 &= \varphi - \pi/2 \end{aligned} \quad (21)$$

$$\begin{aligned} \alpha_2 &= \pi + \alpha_1 \\ \beta_2 &= \pi - \beta_1 \\ \gamma_2 &= \gamma_1 \end{aligned} \quad (22)$$

where $\mathrm{atan2}(x, y)$ is the two-argument arctangent function, which distinguishes between diametrically opposite directions. From the expressions for α, β, and γ, the modulations for the metasurfaces' optic-axis patterns θ_1, θ_2, and θ_3 can be finally extracted. A modulation obtained from a single set of solutions may exhibit discontinuities. To avoid this issue, a dedicated routine automatically switches the solution to be picked whenever the values of the angles feature a sudden jump [44].

ACKNOWLEDGMENTS

This work was supported by Canada Research Chairs (CRC) and Quantum Enhanced Sensing and Imaging (QuEnSI) Alliance Consortia Quantum grant. F.D.C. further acknowledges support from the PNRR MUR Project (No. PE0000023-NQSTI).

F.D.C. conceived the idea and developed the theory, with contributions from A.D.E. and M.A. F.D.C., T.J., and J.G. fabricated the metasurfaces. F.D.C., J.G., and D.P. performed the experiment. F.D.C., T.J., and J.G. analyzed the data. F.D.C. and A.D.E. prepared the first version of the manuscript. A.D.E. and E.K. supervised the project.

The authors declare no conflicts of interest.

DATA AVAILABILITY

The data that support the findings of this article are not publicly available. The data are available from the authors upon reasonable request.

[1] J. Preskill, Quantum Computing in the NISQ era and beyond, Quantum **2**, 79 (2018).

[2] E. Campbell, A series of fast-paced advances in quantum error correction, Nat. Rev. Phys. **6**, 160 (2024).

[3] F. Verstraete, M. M. Wolf, and J. I. Cirac, Quantum computation and quantum-state engineering driven by dissipation, Nat. Phys. **5**, 633 (2009).

[4] P. M. Harrington, E. J. Mueller, and K. W. Murch, Engineered dissipation for quantum information science, Nat. Rev. Phys. **4**, 660 (2022).

[5] R. Kosloff, Quantum thermodynamics: A dynamical viewpoint, Entropy **15**, 2100 (2013).

[6] S. Vinjanampathy and J. Anders, Quantum thermodynamics, Contemp. Phys. **57**, 545 (2016).

[7] S. Deffner and S. Campbell, *Quantum Thermodynamics*, 2053-2571 (Morgan & Claypool Publishers, San Rafael, CA, 2019).

[8] M. O. Scully, Extracting work from a single thermal bath via quantum negentropy, Phys. Rev. Lett. **87**, 220601 (2001).

[9] H.-T. Quan, Y.-X. Liu, C.-P. Sun, and F. Nori, Quantum thermodynamic cycles and quantum heat engines, Phys. Rev. E **76**, 031105 (2007).

[10] M. O. Scully, K. R. Chapin, K. E. Dorfman, M. B. Kim, and A. Svidzinsky, Quantum heat engine power can be increased by noise-induced coherence, Proc. Natl. Acad. Sci. USA **108**, 15097 (2011).

[11] O. Fialko and D. W. Hallwood, Isolated quantum heat engine, Phys. Rev. Lett. **108**, 085303 (2012).

[12] J. P. S. Peterson, T. B. Batalhao, M. Herrera, A. M. Souza, R. S. Sarthour, I. S. Oliveira, and R. M. Serra, Experimental characterization of a spin quantum heat engine, Phys. Rev. Lett. **123**, 240601 (2019).

[13] R. Alicki and M. Fannes, Entanglement boost for extractable work from ensembles of quantum batteries, Phys. Rev. E **87**, 042123 (2013).

[14] F. C. Binder, S. Vinjanampathy, K. Modi, and J. Goold, Quantacell: powerful charging of quantum batteries, New J. Phys. **17**, 075015 (2015).

[15] F. Campaioli, S. Gherardini, J. Q. Quach, M. Polini, and G. M. Andolina, Colloquium: quantum batteries, Rev. Mod. Phys. **96**, 031001 (2024).

[16] A. G. Catalano, S. M. Giampaolo, O. Morsch, V. Giovannetti, and F. Franchini, Frustrating quantum batteries, PRX Quantum **5**, 030319 (2024).

[17] R. Kosloff, E. Geva, and J. M. Gordon, Quantum refrigerators in quest of the absolute zero, J. Appl. Phys. **87**, 8093 (2000).

[18] A. Levy, R. Alicki, and R. Kosloff, Quantum refrigerators and the third law of thermodynamics, Phys. Rev. E **85**, 061126 (2012).

[19] N. Brunner, M. Huber, N. Linden, S. Popescu, R. Silva, and P. Skrzypczyk, Entanglement enhances cooling in microscopic quantum refrigerators, Phys. Rev. E **89**, 032115 (2014).

[20] L. A. Correa, J. P. Palao, D. Alonso, and G. Adesso, Quantum-enhanced absorption refrigerators, Sci. Rep. **4**, 3949 (2014).

[21] Y.-W. Cho, Y. Kim, Y.-H. Choi, Y.-S. Kim, S.-W. Han, S.-Y. Lee, S. Moon, and Y.-H. Kim, Emergence of the geometric phase from quantum measurement back-action, Nat. Phys. **15**, 665 (2019).

[22] M. F. Ferrer-Garcia, K. Snizhko, A. D'Errico, A. Romito, Y. Gefen, and E. Karimi, Topological transitions of the generalized pancharatnam-berry phase, Sci. Adv. **9**, eadg6810 (2023).

[23] N. Moiseyev, *Non-Hermitian Quantum Mechanics* (Cambridge University Press, 2011).

[24] Y. Ashida, Z. Gong, and M. Ueda, Non-Hermitian physics, Adv. Phys. **69**, 249 (2020).

[25] N. Hatano and D. R. Nelson, Vortex pinning and non-Hermitian quantum mechanics, Phys. Rev. B **56**, 8651 (1997).

[26] N. Hatano and D. R. Nelson, Localization transitions in non-Hermitian quantum mechanics, Phys. Rev. Lett. **77**, 570 (1996).

[27] R. Hamazaki, K. Kawabata, and M. Ueda, Non-Hermitian many-body localization, Phys. Rev. Lett. **123**, 090603 (2019).

[28] E. Lee, H. Lee, and B.-J. Yang, Many-body approach to non-Hermitian physics in fermionic systems, Phys. Rev. B **101**, 121109(R) (2020).

[29] K. Kawabata, K. Shiozaki, and S. Ryu, Many-body topology of non-Hermitian systems, Phys. Rev. B **105**, 165137 (2022).

[30] J.-T. Bu, J.-Q. Zhang, G.-Y. Ding, J.-C. Li, J.-W. Zhang, B. Wang, W.-Q. Ding, W.-F. Yuan, L. Chen, Q. Zhong *et al.*, Chiral quantum heating and cooling with an optically controlled ion, Light Sci. Appl. **13**, 143 (2024).

[31] L. Feng, R. El-Ganainy, and L. Ge, Non-Hermitian photonics based on parity–time symmetry, Nature Photon **11**, 752 (2017).
[32] A. Li, H. Wei, M. Cotrufo, W. Chen, S. Mann, X. Ni, B. Xu, J. Chen, J. Wang, S. Fan *et al.*, Exceptional points and non-Hermitian photonics at the nanoscale, Nat. Nanotechnol. **18**, 706 (2023).
[33] G. Harari, M. A. Bandres, Y. Lumer, M. C. Rechtsman, Y. D. Chong, M. Khajavikhan, D. N. Christodoulides, and M. Segev, Topological insulator laser: theory, Science **359**, eaar4003 (2018).
[34] Z. Gong, Y. Ashida, K. Kawabata, K. Takasan, S. Higashikawa, and M. Ueda, Topological phases of non-Hermitian systems, Phys. Rev. X **8**, 031079 (2018).
[35] E. J. Bergholtz, J. C. Budich, and F. K. Kunst, Exceptional topology of non-Hermitian systems, Rev. Mod. Phys. **93**, 015005 (2021).
[36] N. Okuma and M. Sato, Non-Hermitian topological phenomena: A review, Annu. Rev. Condens. Matter Phys. **14**, 83 (2023).
[37] F. Minganti, A. Miranowicz, R. W. Chhajlany, and F. Nori, Quantum exceptional points of non-Hermitian hamiltonians and liouvillians: The effects of quantum jumps, Phys. Rev. A **100**, 062131 (2019).
[38] M. A. Nielsen and I. L. Chuang, *Quantum Computation and Quantum Information* (Cambridge University Press, 2010).
[39] S. Cialdi, M. A. C. Rossi, C. Benedetti, B. Vacchini, D. Tamascelli, S. Olivares, and M. G. A. Paris, All-optical quantum simulator of qubit noisy channels, Appl. Phys. Lett. **110**, 081107 (2017).
[40] P. Renault, J. Nokkala, G. Roeland, N. Y. Joly, R. Zambrini, S. Maniscalco, J. Piilo, N. Treps, and V. Parigi, Experimental optical simulator of reconfigurable and complex quantum environment, PRX Quantum **4**, 040310 (2023).
[41] R. Vasile, F. Galve, and R. Zambrini, Spectral origin of non-markovian open-system dynamics: A finite harmonic model without approximations, Phys. Rev. A **89**, 022109 (2014).
[42] H.-P. Breuer, E.-M. Laine, and J. Piilo, Measure for the degree of non-markovian behavior of quantum processes in open systems, Phys. Rev. Lett. **103**, 210401 (2009).
[43] J. Nokkala, F. Arzani, F. Galve, R. Zambrini, S. Maniscalco, J. Piilo, N. Treps, and V. Parigi, Reconfigurable optical implementation of quantum complex networks, New J. Phys. **20**, 053024 (2018).
[44] F. Di Colandrea, A. Babazadeh, A. Dauphin, P. Massignan, L. Marrucci, and F. Cardano, Ultra-long quantum walks via spin–orbit photonics, Optica **10**, 324 (2023).
[45] A. D'Errico, F. Cardano, M. Maffei, A. Dauphin, R. Barboza, C. Esposito, B. Piccirillo, M. Lewenstein, P. Massignan, and L. Marrucci, Two-dimensional topological quantum walks in the momentum space of structured light, Optica **7**, 108 (2020).
[46] R. Simon and N. Mukunda, Minimal three-component SU(2) gadget for polarization optics, Phys. Lett. A **143**, 165 (1990).
[47] A. Rubano, F. Cardano, B. Piccirillo, and L. Marrucci, Q-plate technology: a progress review [Invited], J. Opt. Soc. Am. B **36**, D70 (2019).
[48] Notice that setting $p = 1$ does not correspond to a noisy interaction, as in this case, the channel would deterministically act on the qubit state.
[49] D. F. V. James, P. G. Kwiat, W. J. Munro, and A. G. White, Measurement of qubits, Phys. Rev. A **64**, 052312 (2001).
[50] E. T. Campbell, B. M. Terhal, and C. Vuillot, Roads towards fault-tolerant universal quantum computation, Nature (London) **549**, 172 (2017).
[51] M. Frey, K. Funo, and M. Hotta, Strong local passivity in finite quantum systems, Phys. Rev. E **90**, 012127 (2014).
[52] R. Salvia, G. De Palma, and V. Giovannetti, Optimal local work extraction from bipartite quantum systems in the presence of Hamiltonian couplings, Phys. Rev. A **107**, 012405 (2023).
[53] R. Castellano, D. Farina, V. Giovannetti, and A. Acin, Extended local ergotropy, Phys. Rev. Lett. **133**, 150402 (2024).
[54] T. Yu and J. H. Eberly, Sudden death of entanglement, Science **323**, 598 (2009).
[55] G. Torlai, C. J. Wood, A. Acharya, G. Carleo, J. Carrasquilla, and L. Aolita, Quantum process tomography with unsupervised learning and tensor networks, Nat. Commun. **14**, 2858 (2023).
[56] F. Di Colandrea, N. Dehghan, A. D'Errico, and E. Karimi, Fourier quantum process tomography, npj Quantum Inf. **10**, 49 (2024).
[57] G. De Filippis, A. de Candia, G. Di Bello, C. A. Perroni, L. M. Cangemi, A. Nocera, M. Sassetti, R. Fazio, and V. Cataudella, Signatures of dissipation driven quantum phase transition in rabi model, Phys. Rev. Lett. **130**, 210404 (2023).
[58] G. Di Bello, A. Ponticelli, F. Pavan, V. Cataudella, G. De Filippis, A. de Candia, and C. A. Perroni, Environment induced dynamical quantum phase transitions in two-qubit rabi model, Commun. Phys. **7**, 364 (2024).

Chapter 4

Quantum Pattern Recognition in Ghost Imaging

This chapter is based on the following articles:

1. Salari, V., **Paneru, D.**, Saglamyurek, E., Ghadimi, M., Abdar, M., Rezaee, M., & Karimi, E. (2023). Quantum face recognition protocol with ghost imaging. *Scientific Reports*, 13(1), 2401.

   DOI: https://www.nature.com/articles/s41598-022-25280-5

4.1 Quantum Imaging

Quantum imaging refers to a class of techniques that exploit quantum mechanical properties of light—such as entanglement and non-classical correlations—to enhance image resolution, sensitivity, and noise tolerance beyond classical limits [90, 91]. Quantum imaging leverages non-classical light sources like entangled photon pairs, squeezed light, and single photons to enable capabilities such as sub-Rayleigh resolution and noise-resilient image reconstruction. For instance, in quantum lithography [92], using non-classical multi-photon states, one can write nanoscale level features beyond the classical diffraction limit, or in quantum-enhanced microscopy where squeezed states of light can be used for highly sensitive measurements with minimal photon flux [93], particularly beneficial in biological imaging. Another variant, quantum illumination [22], uses entangled or correlated light beams to detect low-reflectivity objects in noisy environments.

Quantum imaging experiments typically involve SPDC-based photon pair sources, and much has been discussed about the spatial correlations of the biphotons in the previous section 2.5, and chapter 3. One of the most widely studied approaches using correlated photon pairs is the so-called "ghost imaging", where the image is formed by using photons that never interacted with the object/sample. Typically, it requires some form of correlations between photons, which can be exploited by some form of triggering in the camera to create an image. Correlated bi-photons generated via a nonlinear process naturally provide such a mechanism where signal photons pass undisturbed through an optical path to a camera, and idler photons interact with the object and are detected by a bucket detector that is unable to distinguish any spatial features. By coinciding the time of arrival of such photons with the opening of the shutter of the camera, only the correlated partner of the idler photon is collected in the image plane. Since the photons are strongly correlated in position and momentum degrees of freedom, one can form an image of the object [21, 94, 95]. Ghost imaging has been demonstrated at visible and infrared wavelengths [96], including implementations with compressive sensing algorithms that reduce the number of required measurements while preserving image fidelity [97].

Quantum imaging techniques have the potential to transform biological imaging by enabling non-invasive imaging of delicate biological samples, remote sensing by enhanced detection in cluttered environments, and astronomy, where quantum-enhanced interferometry can increase resolution in distant images. Key challenges include maintaining high entanglement fidelity, achieving high detection efficiencies, and managing losses. Recent advances in integrated photonics and superconducting detectors have improved experimental viability.

4.2 Quantum Algorithms

The computational complexity of any kind of computation can be quantified by the space and time resources required. A lot of useful problems, like path finding or factorization, for example, require exponential resources in classical computation. The promise of quantum computing is to develop and implement new algorithms which provide a resource-efficient solution to these problems. For instance, algorithms like Shor's factoring algorithm [35], based on the quantum Fourier transform, which provide exponential speedup or algorithms based on Grover's search algorithm [98], which provide quadratic speedup compared to the classical ones, are some of the currently known quantum algorithms that provide efficient solutions to useful problems. While searching is an almost ubiquitously applied algorithm, Shor's factoring algorithm is also quite integral because of its implications in breaking common cryptographic protocols using a quantum computer. Most of the quantum algorithms are based on the Quantum Fourier Transform, which we describe in detail below.

4.2.1 Quantum Fourier transform

The Quantum Fourier Transform (QFT) [99] is the quantum analogue of the Discrete Fourier Transform (DFT), and is an integral component in several quantum algorithms, such as Shor's algorithm, discrete logarithm, and quantum phase estimation for estimating eigenvalues of a unitary operator. The quantum Fourier transform notably only requires $O(n^2)$ number of basic gates for a n qubit Hilbert space with 2^n amplitudes, which is an exponential improvement compared with the gate complexity of the classical discrete Fourier transform, $O(n\,2^n)$.

In the computational basis $\{|0\rangle, |1\rangle, \ldots, |N-1\rangle\}$, of an n-qubit quantum system, where $N = 2^n$. The QFT maps a basis state $|x\rangle$ to a superposition state as follows: $\text{QFT}\,|j\rangle = \frac{1}{\sqrt{N}} \sum_{y=0}^{N-1} \omega_N^{jk} |k\rangle$, where $\omega_N = e^{2\pi i/N}$ is the Nth root of unity. More generally, a superposition state $|x\rangle = \sum_{j=0}^{N-1} x_j |j\rangle$ is mapped to $\sum_{j=0}^{N-1} y_j |j\rangle$ with

$$y_k = \frac{1}{\sqrt{N}} \sum_{j=0}^{N-1} x_j \omega_N^{jk}, \quad k = 0, 1, 2, \ldots, N-1. \tag{4.1}$$

The inverse QFT is defined similarly as,

$$x_j = \frac{1}{\sqrt{N}} \sum_{k=0}^{N-1} y_k \omega_N^{-jk}, \quad j = 0, 1, 2, \ldots, N-1. \tag{4.2}$$

The general unitary matrix for the Quantum Fourier transform in N-dimensional Hilbert space can be written as,

$$F_N = \frac{1}{\sqrt{N}} \begin{bmatrix} 1 & 1 & 1 & \cdots & 1 \\ 1 & \omega & \omega^2 & \cdots & \omega^{N-1} \\ 1 & \omega^2 & \omega^4 & \cdots & \omega^{2(N-1)} \\ 1 & \omega^3 & \omega^6 & \cdots & \omega^{3(N-1)} \\ \vdots & \vdots & \vdots & \ddots & \vdots \\ 1 & \omega^{N-1} & \omega^{2(N-1)} & \cdots & \omega^{(N-1)(N-1)} \end{bmatrix} \tag{4.3}$$

where $\omega = e^{2\pi i/N}$.

4.3 Research Summary

In the second part of the chapter, we present the work on a conceptual proposal for a fully quantum imaging system that combines a quantum pattern recognition algorithm with quantum imaging [100]. We propose a novel algorithm for finding a dissimilarity measure between two dimensional images with a complexity of O(N logN). We also present the results of a ghost imaging experiment where the samples are images of human faces. Potential applications of the work could be in future quantum pattern identification systems.

scientific reports

OPEN

Quantum face recognition protocol with ghost imaging

Vahid Salari[1,2], Dilip Paneru[3], Erhan Saglamyurek[1,4], Milad Ghadimi[5], Moloud Abdar[6], Mohammadreza Rezaee[3], Mehdi Aslani[5], Shabir Barzanjeh[1] & Ebrahim Karimi[3,7]✉

Face recognition is one of the most ubiquitous examples of pattern recognition in machine learning, with numerous applications in security, access control, and law enforcement, among many others. Pattern recognition with classical algorithms requires significant computational resources, especially when dealing with high-resolution images in an extensive database. Quantum algorithms have been shown to improve the efficiency and speed of many computational tasks, and as such, they could also potentially improve the complexity of the face recognition process. Here, we propose a quantum machine learning algorithm for pattern recognition based on quantum principal component analysis, and quantum independent component analysis. A novel quantum algorithm for finding dissimilarity in the faces based on the computation of trace and determinant of a matrix (image) is also proposed. The overall complexity of our pattern recognition algorithm is $O(N \log N)$—N is the image dimension. As an input to these pattern recognition algorithms, we consider experimental images obtained from quantum imaging techniques with correlated photons, e.g. "interaction-free" imaging or "ghost" imaging. Interfacing these imaging techniques with our quantum pattern recognition processor provides input images that possess a better signal-to-noise ratio, lower exposures, and higher resolution, thus speeding up the machine learning process further. Our fully quantum pattern recognition system with quantum algorithm and quantum inputs promises a much-improved image acquisition and identification system with potential applications extending beyond face recognition, e.g., in medical imaging for diagnosing sensitive tissues or biology for protein identification.

In any intelligent image processing system, there are essentially two main steps: the acquisition of the image and the recognition of the desired patterns. Image acquisition for any pattern recognition method can be performed in multiple ways. For instance, classical sources (incoherent light from thermal radiation or a coherent beam from a laser) or quantum sources (entangled photons obtained from down conversion or squeezed light) can be used to obtain the images. Classical bright field imaging techniques employing the former sources, have the disadvantage of high probe illumination requirement, especially while imaging sensitive samples. Additionally, they are also plagued by the shot noise inherent in the intensities, and the background noise from the environment. Quantum techniques such as quantum illumination, or ghost imaging or even interaction-free imaging, alleviates the problems of background noise, and the probe illumination by utilizing quantum correlations between photon pairs[1,2]. Furthermore, quantum sub-shot noise imaging[3] and super resolution techniques[4] enhance the noise sensitivity and resolution in any images beyond the classical limits.

As a second important step, pattern recognition in the acquired images is a prominent feature of any intelligent imaging system. Face recognition[5,6] is one of the branches of pattern recognition, with numerous applications such as face ID verification, passport checks, entrance control, computer access control, criminal investigations, crowd surveillance, and witness face reconstruction[7], among several others. For face recognition, several classical machine learning algorithms exist[8], generally requiring huge computational resources especially when faced with the problem of identification from a large database. Quantum machine learning algorithms employing quantum features such as superposition and entanglement[9,9–17] promise enhancements in terms of the computing resources and the speed compared to the classical counterparts. Several experimental researches have been

[1]Department of Physics and Astronomy, Institute for Quantum Science and Technology, University of Calgary, Calgary, AB T2N 1N4, Canada. [2]BCAM - Basque Center for Applied Mathematics, Alameda de Mazarredo 14, 48009 Bilbao, Basque Country, Spain. [3]Nexus for Quantum Technologies, University of Ottawa, 25 Templeton Street, Ottawa, ON K1N 6N5, Canada. [4]Department of Physics, University of Alberta, Edmonton, AB T6G 2E1, Canada. [5]Department of Physics, Isfahan University of Technology, Isfahan 8415683111, Iran. [6]Institute for Intelligent Systems Research and Innovation (IISRI), Deakin University, Geelong, Australia. [7]National Research Council of Canada, 100 Sussex Drive, Ottawa, ON K1A 0R6, Canada.

done to implement these algorithms[18–25]. In this article, we present a quantum algorithm for face recognition as one of the potential applications of quantum algorithms in machine learning.

The problem of identification of faces from any images generally constitutes different steps (shown in Fig. 1): creating a database of faces consisting of training and test images, feature extraction using principal component analysis (PCA), linear discriminant analysis (LDA) or independent component analysis (ICA), feature matching using dissimilarity measures, and recognition[26]. PCA extracts the eigenstates (or eigenfaces) of the covariance matrix of the images in the database, including information like average face, gender (male or female), face direction, brightness, shadows, etc. ICA, however, extracts the independent elements such as eyes, eyebrows, mouth, nose, etc. in a face. Quantum algorithms which provide speedup for PCA and ICA have already been proposed[9,27]. Here, we focus on three main steps: (1) Quantum Principle Component Analysis (QPCA)[9], (2) Quantum Independent Component Analysis (QICA)[27], and (3) Dissimilarity measures (i.e., face matching), to develop a quantum algorithm for face recognition. In what follows, we present a quantum algorithm for dissimilarity measures for face matching with speedup. This is based on a quantum algorithm to compute the log determinant divergence using both the determinant and the trace of a matrix. Our algorithm combined with the inputs obtained from quantum imaging techniques provides a fully intelligent pattern identification system, with the joint benefit of the low-dose and higher resolution of quantum imaging methods, and the speedup and efficiency of the quantum algorithms. Figure 1 shows the flowchart of the quantum algorithm for the pattern identification.

Quantum face recognition

Classical algorithms are unable to process quantum data directly. During the conversion of the quantum states (qubits) to classical data (bits), most of the information is lost in the measurement process, due to the "collapse" of the wavefunction. Although techniques such as quantum state tomography implemented on unlimited ensemble of the states can be used to fully reconstruct the quantum states from classical projections, these processes are generally complex and expensive. Therefore, the optimal input to our quantum algorithms, would be the quantum states directly obtained from quantum processes, for example, quantum imaging methods, or from a quantum memory, without performing a strong measurement on the wavefunction.

Photonic quantum memories[28], allowing storage and on-demand retrieval of quantum states of light, is one of the key components for the realization of quantum optical pattern-recognition technology. Quantum memories essentially form a quantum database for the matching stage in the recognition process. With the state-of-art quantum memories, the possibility of storing hundreds of spatial modes has already been shown in experimental studies using atomic-cold gases[29,30]. Furthermore, using solid-state atomic memories, it is possible to simultaneously store hundreds of photonic quantum states in distinct temporal modes, thus allowing us to store patterns

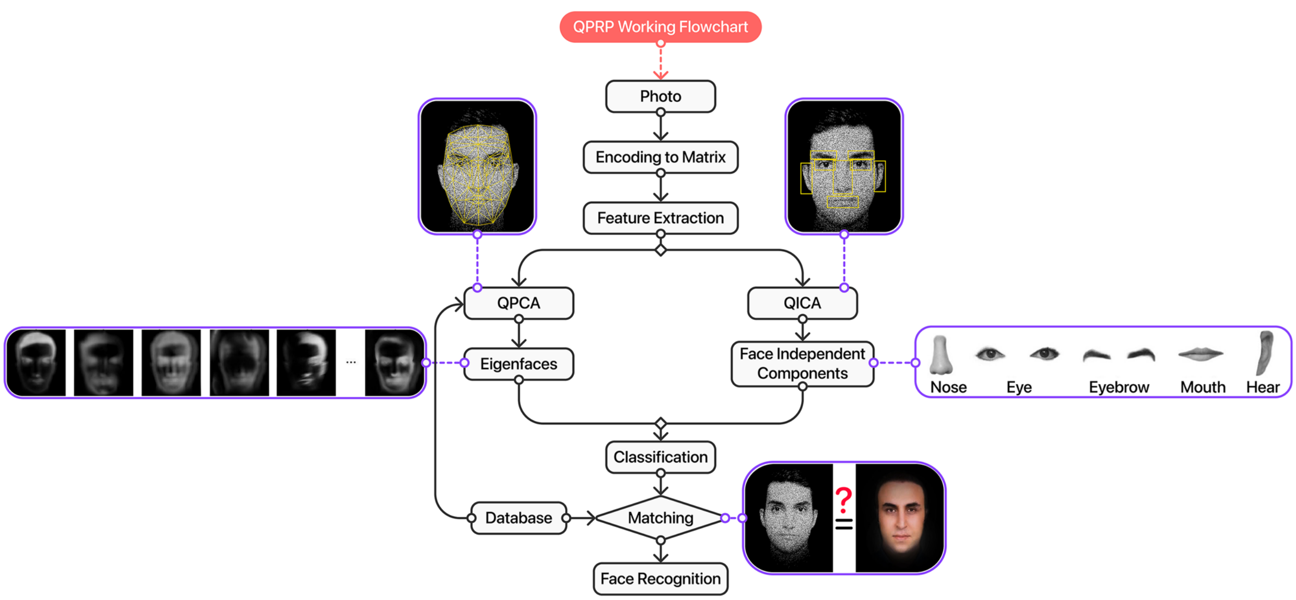

Figure 1. Flowchart of the quantum algorithm for face recognition. The quantum algorithm is proposed to be performed in a quantum processor, which we call it quantum pattern recognition processor (QPRP). First the image is converted into matrix form, on which feature extraction algorithms such as quantum principal component analysis (QPCA) or quantum independent component analysis (QICA) are applied. QPCA extracts the eigenstates (or eigenfaces) of the covariance matrix of the images in the database. The eigenfaces include information like average face, gender (male, female), face direction, brightness, shadows, etc. QICA extracts the independent elements such as eyes, eyebrows, mouth, nose, etc. in a face. The complexity of this stage is O(log N)—N is the dimension of th image. Then, the given faces are compared with the faces in the database by using dissimilarity measure based on the log determinant divergence, and the best match among the faces in the database is identified.

scanned at separate times[31,32]. In addition, optically accessible spin-states of certain atomic systems can reach several hours of coherence time[33]. A very recent experimental demonstration reports one-hour memory lifetime for light storage, showing the feasibility of long-lived photonic quantum memory devices[34]. Atomic memory approaches have also been shown to reach high retrieval efficiencies up to 92%[35] and high fidelities above 99%[36]. However, an implementation with all of the aforementioned properties still remains as a challenge in developing a practical quantum database memory.

Quantum techniques such as quantum ghost imaging[37], quantum lithography[38], or quantum sensing[39], when appropriately interfaced with photonic quantum processors, for example an array of optical fibers connected to an integrated quantum photonic circuit, can also act as inputs to our algorithms (see Fig. 2). Here for the case of our face recognition algorithm, we assume that the input images are acquired by quantum ghost imaging[37]. Ghost imaging exploits the spatial correlations between photon pairs generated through a nonlinear process called spontaneous parametric down-conversion (SPDC). Since the images are obtained by triggering the shutter in order to capture only the "coincident" photon pairs, the level of background noise is significantly reduced, along with a reduction in probe illumination. In a variation of this technique using non degenerate photon pairs, the image detection and sample interaction can happen at different wavelengths, which can be useful when imaging sensitive tissues when limited in detection technologies[40]. Combining quantum detection techniques such as interaction-free measurement with ghost imaging, the illumination level required for the same levels of Signal to Noise ratio (SNR) in images[41] is further reduced significantly. Figure 3 shows some of the images of human faces obtained in a quantum ghost imaging setup, where spatially correlated photon pairs (namely signal and idler), are generated by pumping a BiBO crystal with pump photons. Phase holograms placed in a Spatial Light Modulator, a liquid crystal device, created by superimposing the human faces with a diffraction grating acts as an object for the signal photon, while the idler photon passes to the Intensified Charged Coupled Devices (ICCD) camera via a delaSupplementary Informationy line. The images are obtained by triggering the ICCD shutter with the signal photons detected through a Single Photon Avalanche Diode (SPAD) detector—see (SI) for the detail of the experimental setup.

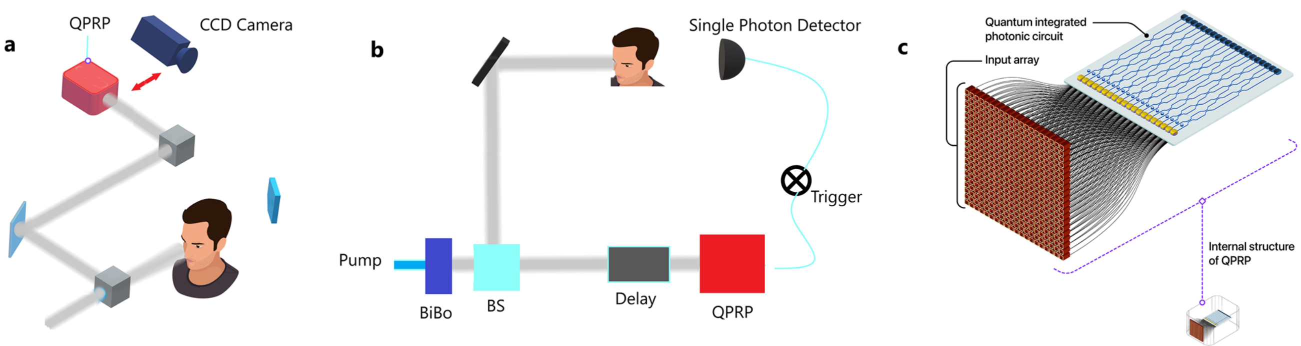

Figure 2. Intelligent pattern recognition in quantum imaging. Data from quantum imaging methods such as (**a**) interaction free imaging and (**b**) ghost imaging act as an input to (**c**) quantum pattern recognition processor (QPRP). The latter, i.e., QPRP, applies quantum machine learning to find the patterns in the database.

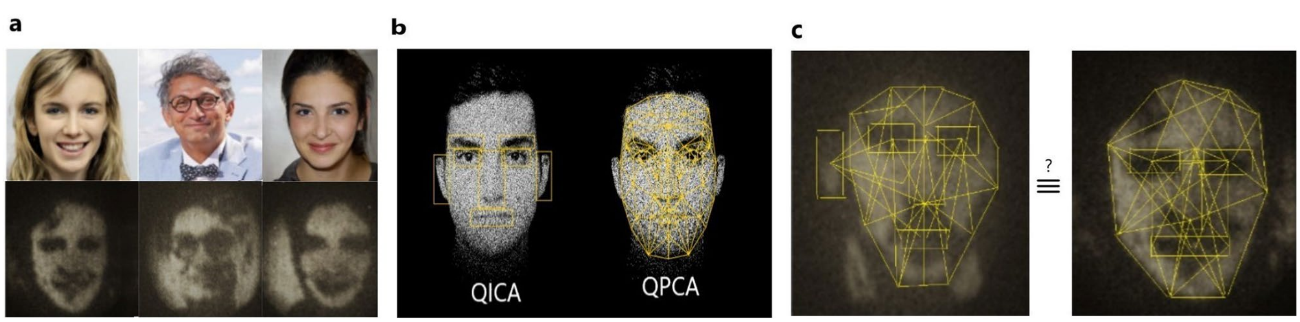

Figure 3. Face recognition in ghost images. (**a**) Images of the original human faces (top) and the corresponding experimental ghost images (bottom) obtained in a ghost imaging setup. A femtosecond laser is used to generate spatially entangled photon pairs. One of the photons illuminates a spatial light modulator, which imprints different images onto the photon, and can act as a trigger for the other photon that was detected by an intensified CCD camera. Each of the images was obtained by the accumulation of 300 frames with an exposure time of 0.5s, which translates to a run time of 150s. (**b**) Quantum Independent Component Analysis (QICA), and Quantum Principal Component Analysis (QPCA), of the faces to detect the independent components, and principal features in the faces. (**c**) Dissimilarity measure between the ghost images with the images in the database for their identification. As per the copyright policies of the journal, in this illustration we use artificially generated faces (the first and the third) from the website https://www.thispersondoesnotexist.com. For the second figure, the coauthor provided the required consent for both the experiment and use in the manuscript.

Quantum principal component analysis (QPCA). We have now the input images either retrieved from a quantum memory or directly as outputs from a quantum imaging setup. The pattern recognition processor applies Quantum Principal Component Analysis (QPCA)[9,42] to extract the principal eigenvectors of the covariance matrix C_X, formed by the set of the training images.

Let us consider a set of N-dimensional training images (or faces), $\{|x^{(1)}\rangle, \ldots, |x^{(M)}\rangle\}$. Here, $|x^{(i)}\rangle$ is the i-th training image, which is given by,

$$|x^{(i)}\rangle = \sum_{q=1}^{N} x_q^{(i)} |\psi_q^{(i)}\rangle, \tag{1}$$

where $x_q^{(i)}$ are the components, and $|\psi_q^{(i)}\rangle$ are the basis kets. The covariance matrix C_X can be formed as a sum over M training faces[42],

$$C_X = \frac{1}{M} \sum_{i=1}^{M} |x^{(i)}\rangle\langle x^{(i)}|. \tag{2}$$

The next step is to exponentiate the covariance matrix C_X, so that we can use the Quantum Phase Estimation (QPE) subroutine for finding the eigenvectors and eigenvalues. It has been shown that the exponentiation of the covariance matrix, i.e., $e^{-iC_X t}$, can be performed in $\mathcal{O}(\log N)$ time[9].

In QPCA algorithm, for the phase estimation subroutine, we apply the operator $U = e^{-iC_X t}$ on C_X[42]. The action of U on one of the states $|x^{(i)}\rangle$ in C_X is:

$$e^{-iC_X t}|x^{(i)}\rangle \rightarrow \sum_{j=1}^{M} c^{(ij)} |\phi^j\rangle, \tag{3}$$

where $|\phi^j\rangle$'s are the eigenvectors of C_X, and $c^{ij} = e^{-i\tilde{\lambda}_c^{(j)} t}\langle\phi^j|x^{(i)}\rangle$ in which $\tilde{\lambda}_c^{(j)} = \left(2\pi\lambda_c^{(j)} t\right)/2^n$ where $\lambda_c^{(j)}$'s are the corresponding estimated eigenvalues of C_X with precision n[9,42].

In order to obtain the principal eigenfaces (the eigenvectors of the covariance matrix with larger eigenvalues), we define a score $s^{(ij)}$, which is the projection of an eigenvector $|\phi^{(j)}\rangle$ on a training vector $|x^{(i)}\rangle$,

$$s^{(ij)} = \langle x^i|\phi^j\rangle = \sum_{q=1}^{N} x_q^{(i)} \phi_q^{(j)}, \tag{4}$$

where $\phi_n^{(j)}$ are the components of the eigenvector $|\phi^j\rangle$. The eigenvectors corresponding to the r highest scores are the principal components (or eigenfaces). Each face can be expanded in terms of the r eigenfaces (principal components) but with different weights ω_j's as follows

$$|\text{Face}^{(i)}\rangle = \sum_{j=1}^{r} \omega_j |\boldsymbol{\phi}^j\rangle. \tag{5}$$

The "mean image" is the eigenface corresponding to the largest eigenvalue of C_X. The QPCA algorithm is efficient for the case $r \ll N$[42].

Quantum independent component analysis (QICA). In classical machine learning, Independent Component Analysis (ICA) is performed to decompose an observed signal into a linear combination of unknown independent signals[26]. Similar to the PCA, the ICA finds a new basis to represent the data, however with a different goal. We assume that there is a data set of faces $s \in R^d$ that is a collection of d independent elements in the face such as nose, eye, eyebrow, mouth, etc. Each image observed through a camera can be expressed as $x = F \cdot s$, where F is a mixing matrix of the independent face elements. Repeated observation gives us a dataset x as $\{x^{(i)}, \ldots, x^{(M)}\}$, and ICA estimates the independent sources $s^{(i)}$ that had generated the face. We let $W = F^{-1}$ which is the unmixing matrix and solve the linear systems of equations $s^{(i)} = W\,x^{(i)}$ for estimating the independent elements of the face. We should note here that $s^{(i)}$ is a d-dimensional vector and $s_j^{(i)}$ is the data of element j. Similarly, $x^{(i)}$ is an d-dimensional vector, and $x_j^{(i)}$ is the observed (or recorded) element j by camera. The ICA can be exponentially speedup via a quantum algorithm for sparse matrices, with the Harrow-Hassidim-Lloyd (HHL) algorithm[27], which is used to solve linear systems of equations optimally with $O(\log N)$. For comparison, classically it takes a time $O(N^3)$ to be solved via the Gauss elimination, and approximately $O(N\sqrt{\kappa})$ via iterative methods[27] for a sparse matrix of size $N \times N$, with κ being the ratio between the greatest and the smallest eigenvalue.

Pattern matching: comparing faces. As important details of a face are obtained either by using QPCA or QICA, each face is represented in the form of a sparse matrix in which non-important elements are set to zero. The last and important step of the algorithm is comparing the face patterns to recognize the target face. Pattern matching algorithms investigate exact matches in the input with pre-existing patterns in the database. In fact, the problem here is comparing matrices with each other. The evaluation of matching between matrices (or face patterns) can be done by using "dissimilarity"[43] measures that calculate the "distance" between the matrices. The lower the values of the dissimilarity/distance measures, more similar the matrices, with the fully matched matrices having a zero distance. One such distance measure used to compare two matrices X and Y is called the "Log-determinant divergence"[43,44] defined as,

$$D(X, Y) = \mathrm{Tr}\big(X \cdot Y^{-1}\big) - \log\det\big(X \cdot Y^{-1}\big) - N, \tag{6}$$

where N is the dimension of the matrices. When $D = 0$, the matrices X and Y are completely matched, and higher the distance value the more different are the matrices. The least value among the all distance values identifies the best match and consequently recognizes the face. As it is seen in the distance formula, it is a benefit to be able to calculate the trace and the determinants of matrices with speedup to expedite the distance calculation. In the following, we propose quantum algorithms for computation of the determinant and the trace of a sparse matrix.

Quantum computation of sparse matrix determinants and trace. To obtain a measure of dissimilarity between two matrices we need to calculate the determinant and the trace of the sparse matrix $A = X \cdot Y^{-1}$. First we calculate Y^{-1} using the HHL algorithm[27] and obtain A by multiplying it with X. We then apply the Quantum Phase Estimation (QPE) subroutine, which consists of a quantum Fourier transform (QFT) followed by a controlled Unitary (CU) operation, with $U = e^{-iAt}$, and a inverse quantum Fourier transform. We then apply a controlled Rotation operation followed by the inverse Quantum Phase Estimation (QPE) subroutine. At the end we have a multiplication operator Π which finally gives us the product of the eigenvalues—the algorithm steps are explained in more detail in the Supplementary Information. The running time of the algorithm up to the third step, i.e. applying the controlled-U operator, is $O(\log N(s^2\kappa^2/\epsilon))$[27], where s is the sparsity, κ is the ratio of largest eigenvalue to the smallest eigenvalue of A, and ϵ is the acceptable error. Additionally, the multiplication operation in the last step can be performed in time $O(\log N)$ and the algorithm should run N times. Therefore, the overall complexity of the algorithm is $O\big(N\log N(1 + s^2\kappa^2/\epsilon)\big)$, which is much faster than the classical ones (see Table 1).

In order to compute the trace of the matrix A, an adder quantum algorithm[48] can speedup the computation. The adder operation between two diagonal elements is mainly based on the quantum Fourier transform (QFT), i.e. $|\Phi(a)\rangle := \mathrm{QFT}\,|a\rangle = \frac{1}{\sqrt{N}}\sum_{k=0}^{N-1} e^{i\frac{2\pi ak}{N}}|k\rangle$ and the inverse QFT, i.e., $\mathrm{QFT}^{-1}|\Phi(a)\rangle = |a\rangle$. By continuation of this method sequentially for the all diagonal elements, one can obtain the trace of the matrix. The detail of the adder algorithm and the quantum circuit for the computation of trace is discussed in the Supplementary Information (Fig. S2 shows the corresponding quantum circuit). The whole process which is based on QFT and QFT^{-1} has a complexity of $O(\log N)$ (Table 2).

QPCA and QICA both have logarithmic complexities, i.e., $O(\log N)$. For the calculation of the log determinant divergence, the computation of trace has a complexity of $O(\log N)$, while the determinant has complexity of $O(N\log N)$). Hence, the overall complexity of the whole algorithm is $O(N\log N)$. Table 2 shows a summary of estimated complexities along with the complexity of the general quantum face recognition algorithm.

Discussion

Here, we have shown that classically the best pattern recognition algorithm based on ICA and PCA would take at least $O(N^2 \mathrm{Log} N)$ steps while our algorithm only takes $O(N \mathrm{Log} N)$ steps, which is an order of magnitude faster—N is the dimension of images (see Table 3 for some estimates). We should note here that our protocol is not compared with neural networks approaches, for instance, we did not compare our quantum protocol with a

Approach	Method	Complexity	References
Classic	Laplace	N^3	[45]
Classic	Gaussian	N^3	[45]
Classic	Coppersmith–Winogard	$N^{2.373}$	[46]
Classic	Wiedemann	$N^2\log N$	[47]
Quantum	Our method	$N\log N$	CW

Table 1. A Comparison of complexities between the classical approaches and our quantum approach, current work (CW), for the computation of determinant.

Method	Output	Complexity	References
QPCA	Eigenfaces	$\log N$	[9]
QICA & HHL	Face components	$\log N$	[27]
HHL	Matrix inversion	$\log N$	[27]
Our method	Determinant calculation	$N\log N$	CW
Our method	Trace calculation	$\log N$	CW
Log-det divergence	Face matching	$N\log N$	CW
Our method (General)	Face recognition	$N\log N$	CW

Table 2. Summary of estimated complexities in quantum face recognition algorithm.

Image dimensions	Encoding qubits	Classical processing time (in a.u.)	Quantum processingtime (in a.u.)
64 × 64	6	7398.1	115.5
128 × 128	7	34524.5	269.7
256 × 256	8	157826.4	616.5
512 × 512	9	710218.8	1387.1
1024 × 1024	10	3156528.2	3082.5
2028 × 2028	11	13888724.4	6781.6

Table 3. Numerical estimates of the time complexities (in arbitrary units) for the classical and the quantum protocol for different input image dimensions along with the corresponding number of qubits required for encoding.

classical deep learning model. In fact, the protocol suggested in our paper is only a comparison with its classical counterparts based on classical PCA, ICA, and Distance. There are other quantum models which are robust versus their classical counterparts, for example, using QPCA and quantum neural networks show advantages over the best classical approaches[49,50], or training deep quantum neural networks give a fast optimization and a striking robustness to noisy training data[51]. It has been shown that a quantum convolutional neural network uses only O(Log*N*) variational parameters for input sizes of *N* qubits, allowing for its efficient training and implementation on realistic, near-term quantum devices[52].

Apart from these, our protocol would also benefit from the quantum nature of the image acquisition, namely lower sample exposure, background acquisition, and resolution enhancement. From the acquisition point of view, to have an image with a desirable resolution the images were accumulated for 300 frames with an exposure time of 0.5 s, hence, to obtain a single image it takes roughly 150 s, i.e. independent from the image processing side (see Table 4). Classical or direct imaging offers much faster image acquisition times, however here we are relying on the entangled photon pairs, the production rate of which is less than 1% of the total power of the pump beam, hence we have much less photons interacting with the sample (or face) and hence the need for longer exposure times. In fact, it is not the speed that is the improvement in the imaging part. With higher pump power and efficient crystals this process can also be improved further however the state of the art on this would not match the acquisition speed of classical methods. The advantage of this is that we achieve a better SNR if we compare the images with classical acquisition with a similar number of photons interacting with the sample.

Depending on the database, compared to the best classical pattern recognition algorithm, the proposed quantum algorithm will be *N* times faster. Both the QPCA and QICA can be used for face recognition in classical images as well, as it can perform the pattern identification on any matrix. Run on a quantum processor, it would provide a speedup in the process compared to the traditional recognition methods. At the moment, due to the image size, no quantum computers are yet available that can successfully implement the quantum protocol. However, this is indeed a possible future step once such devices are available.

Conclusion

In summary, we propose a new concept of a quantum protocol for 2D face recognition, combining the benefits of quantum imaging in image acquisition with the speedup from the quantum machine learning algorithms. In this concept, we consider images to be obtained via a ghost imaging protocol either as inputs to the quantum memories or as a hardware encoding of quantum information for the photonic pattern recognition processor. Feeding the "images" directly from a quantum protocol also eliminates the need for the conversion of classical data to quantum inputs for the processor saving valuable computational resources. The quantum pattern recognition processor then runs an algorithm composed of three main subroutines: (1) quantum principal components analysis (QPCA), (2) quantum independent component analysis (QICA), and (3) quantum dissimilarity measures for comparing faces. For the QPCA and QICA, we propose slight modifications in the existing algorithms, whereas for finding the dissimilarity measure, we propose a novel algorithm for obtaining the distance between two matrices based upon a metric called log-determinant divergence. Our algorithm obtains the determinant and the trace of the two matrices in $O(N \log N)$ time—N is the dimension of the matrix. Complexity analysis shows that all of the three parts have speedup as compared to their classical counterparts, with the overall complexity given by $O(N \log N)$. Our conceptual protocol provides a framework for an intelligent and fully quantum image recognition system with quantum inputs and a quantum machine learning processor. The joint benefits of the quantum image acquisition and quantum machine learning promises exciting technological developments in the field of image recognition systems.

Image dimensions	Total photons = Average photons/pixel × no of pixels	Imaging time (sec)	Signal to noise ratio (SNR)
64×64	$98304 = 12 \times (64)^2$	4	3.46
64×64	$786432 = 96 \times (64)^2$	32	9.80
64×64	$3686400 = 450 \times (64)^2$	150	21.21
128×128	$14745600 = 450 \times (128)^2$	150	21.21
256×256	$58982400 = 450 \times (256)^2$	150	21.21
512×512	$6291456 = 450 \times (512)^2$	150	21.21
1024×1024	$235929600 = 450 \times (1024)^2$	150	21.21
2028×2028	$3774873600 = 450 \times (2028)^2$	150	21.21

Table 4. Numerical estimates of the Signal to Noise ratio (SNR) in the ghost images of different dimensions along with the total number of photons acquired corresponding to different acquisition times.

Data availability

All data needed to evaluate the conclusions in the paper are present in the paper and/or the Supplementary Materials. Additional data related to this paper may be requested from V.S.(vahid.salari1@ucalgary.ca) or E.K. (ekarimi@uottawa.ca).

Received: 2 February 2022; Accepted: 28 November 2022
Published online: 10 February 2023

References

1. Shapiro, Jeffrey H. & Boyd, Robert W. The physics of ghost imaging. *Quant. Inform. Process.* **11**, 949–993 (2012).
2. Moreau, P. A., Toninelli, E., Gregory, T. & Padgett, M. J. Ghost imaging using optical correlations. *Laser Photon. Rev.* **12**, 1700143 (2018).
3. Brida, G., Genovese, M. & Berchera, I. R. Experimental realization of sub-shot-noise quantum imaging. *Nat. Photon.* **4**, 227–230 (2010).
4. Tsang, M., Nair, R. & Xiao-Ming, L. Quantum theory of superresolution for two incoherent optical point sources. *Phys. Rev. X* **6**, 031033 (2016).
5. Kortli, Y., Jridi, M., Al Falou, A. & Atri, M. Face recognition systems: A survey. *Sensors* **20**, 342 (2020).
6. Wright, J. *et al.* Robust face recognition via sparse representation. *IEEE Trans. Patt. Anal. Mach. Intell.* **31**, 210 (2009).
7. Acan, A. & Toygar, O. Face recognition using pca, lda and ica approaches on colored images. *J. Elect. Elect. Eng.* **3**, 735 (2003).
8. Hasan, Md. K. *et al.* Human face detection techniques: A comprehensive review and future research directions. *Electronics* **10**, 2354 (2021).
9. Lloyd, S., Mohseni, M. & Rebentrost, P. Quantum principal component analysis. *Nat. Phys.* **10**, 631–633 (2014).
10. Rebentrost, P., Mohseni, M. & Lloyd, S. Quantum support vector machine for big data classification. *Phys. Rev. Lett.* **113**, 130503 (2014).
11. Lloyd, S., Garnerone, S. & Zanardi, P. Quantum algorithms for topological and geometric analysis of data. *Nat. Commun.* **7**, 1–7 (2016).
12. Biamonte, J. *et al.* Quantum machine learning. *Nature* **549**, 195–202 (2017).
13. Petruccione, F. & Schuld, M. *Supervised Learning with Quantum Computers* 3rd edn. (Springer, 1993).
14. Powell, D. Quantum boost for artificial intelligence. *Nature News*https://doi.org/10.1038/nature.2013.13453 *(2013).*
15. Alvarado Barrios, G., Albarrán-Arriagada, F., Cárdenas- López, F. A., Romero, G. & Retamal, J. C. Role of quantum correlations in light-matter quantum heat engines. *Phys. Rev. A.* **96**, 052119 (2017).
16. Cárdenas-López, F. A., Lamata, L., Retamal, J. C. & Solano, E. Multiqubit and multilevel quantum reinforcement learning with quantum technologies. *PloS One* **13**, e0200455 (2018).
17. Paneru, D., Cohen, E., Fickler, R., Boyd, R. W. & Karimi, E. Entanglement: Quantum or classical? *Rep. Prog. Phys.* **83**, 064001 (2020).
18. Zhang, X. *et al.* Semiconductor quantum computation. *Natl. Sci. Rev.* **6**, 32–54 (2019).
19. Gaita-Ariño, A., Luis, F., Hill, S. & Coronado, E. Molecular spins for quantum computation. *Nat. Chem.* **11**, 301–309 (2019).
20. Collins, D., Kim, K. W., Holton, William C., Sierzputowska-Gracz, H. & Stejskal, E. O. Nmr quantum computation with indirectly coupled gates. *Phys. Rev. A.* **62**, 022304 (2000).
21. Schuch, N. & Siewert, J. Implementation of the four-bit deutsch-jozsa algorithm with josephson charge qubits. *Phys. Status Solidi b* **233**, 482–489 (2002).
22. Zhen, W. *et al.* Experimental demonstration of the deutschjozsa algorithm in homonuclear multispin systems. *Phys. Rev. A* **84**, 042312 (2011).
23. Takeuchi, S. Experimental demonstration of a threequbit quantum computation algorithm using a single photon and linear optics. *Phys. Rev. A* **62**, 032301 (2000).
24. Gulde, S. *et al.* Implementation of the deutsch-jozsa algorithm on an ion-trap quantum computer. *Nature* **421**, 48–50 (2003).
25. Barz, S. *et al.* A two-qubit photonic quantum processor and its application to solving systems of linear equations. *Sci. Rep.* **4**, 1–5 (2014).
26. Draper, B. A., Baek, K., Bartlett, M. S. & Beveridge, J. R. Recognizing faces with pca and ica". *Comput. Vis. Image Underst.* **91**, 115–137 (2003).
27. Harrow, A. W., Hassidim, A. & Lloyd, S. Quantum algorithm for linear systems of equations. *Phys. Rev. Lett.* **103**, 150502 (2009).
28. Lvovsky, A. I., Sanders, B. C. & Tittel, W. Optical quantum memory. *Nat. Photon.* **3**, 706–714 (2009).
29. Parniak, M. *et al.* Wavevector multiplexed atomic quantum memory via spatially-resolved single-photon detection. *Nat. Commun.* **8**, 1–9 (2017).
30. Pu, Y. F. *et al.* Experimental realization of a multiplexed quantum memory with 225 individually accessible memory cells. *Nat. Commun.* **8**, 1–6 (2017).
31. Bonarota, M., Le Gouët, J. L. & Chaneliere, T. Highly multimode storage in a crystal. *New J. Phys.* **13**, 013013 (2011).

32. Tang, J.-S. *et al.* Storage of multiple single-photon pulses emitted from a quantum dot in a solid-state quantum memory. *Nat. Commun.* **6**, 1–7 (2015).
33. Zhong, M. *et al.* Optically addressable nuclear spins in a solid with a six-hour coherence time. *Nature* **517**, 177–180 (2015).
34. Ma, Yu., Ma, Y.-Z., Zhou, Z.-Q., Li, C.-F. & Guo, G.-C. One-hour coherent optical storage in an atomic frequency comb memory. *Nat. Commun.* **12**, 1–6 (2021).
35. Hsiao, Y. F. *et al.* Highly efficient coherent optical memory based on electromagnetically induced transparency. *Phys. Rev. Lett.* **120**, 183602 (2018).
36. Liu, C. *et al.* Reliable coherent optical memory based on a laserwritten waveguide. *Optica* **7**, 192–197 (2020).
37. Morris, P. A., Aspden, R. S., Bell, J. E. C., Boyd, R. W. & Padgett, M. J. Imaging with a small number of photons. *Nat. Commun.* **6**, 1–6 (2015).
38. Boto, A. N. *et al.* Quantum interferometric optical lithography: Exploiting entanglement to beat the diffraction limit. *Phys. Rev. Lett.* **85**, 2733 (2000).
39. Israel, Y., Rosen, S. & Silberberg, Y. Supersensitive polarization microscopy using noon states of light. *Phys. Rev. Lett.* **112**, 103604 (2014).
40. Chan, K. W. C., O'Sullivan, M. N. & Boyd, R. W. Two-color ghost imaging. *Phys. Rev. A* **79**, 033808 (2009).
41. Zhang, Y. *et al.* Interaction-free ghost-imaging of structured objects. *Opt. Exp.* **27**, 2212–2224 (2019).
42. Kopczyk, D. Quantum machine learning for data scientists. arXiv preprint arXiv:1804.10068 (2018).
43. Cichocki, A., Cruces, S. & Amari, S. Logdeterminant divergences revisited: Alpha-beta and gamma logdet divergences. *Entropy* **17**, 2988–3034 (2015).
44. Dhillon, I. S. & Tropp, J. A. Matrix nearness problems with bregman divergences. *SIAM J. Matrix Anal. Appl.* **29**, 1120–1146 (2008).
45. Bunch, J. R. & Hopcroft, J. E. Triangular factorization and inversion by fast matrix multiplication. *Math. Comput.* **28**, 231–236 (1974).
46. Williams, V. V. Multiplying matrices in o (n2. 373) time. preprint (2014).
47. Wiedemann, D. Solving sparse linear equations over finite fields. *IEEE Trans. Inf. Theory* **32**, 54–62 (1986).
48. Ruiz-Perez, L. & Garcia-Escartin, J. C. Quantum arithmetic with the quantum fourier transform. *Quantum Inf. Process.* **16**, 152 (2017).
49. Huang, H. Y. *et al.* Quantum advantage in learning from experiments. *Science* **376**(6598), 1182–1186 (2022).
50. Lídia, H. W., del Iten, R. R., Metger, T. & Renner, R. Discovering physical concepts with neural networks. *Phys. Rev. Lett.* **124**, 010508 (2020).
51. Beer, K. *et al.* Training deep quantum neural networks. *Nat. Commun.* **11**, 808 (2020).
52. Cong, S. C. I. & Lukin, M. D. Quantum convolutional neural networks. *Nat. Phys.* **15**, 1273–1278 (2019).

Acknowledgements
V. S. is very thankful for several helpful discussions with Mikel Sanz and Enrique Solano during his research stay in QUTIS center in Bilbao (Spain) and QuArtist center in Shanghai (China) who encouraged the idea to be developed. Also, V. S. is very grateful for useful discussions with Seth Lloyd and Nathan Wiebe during the Quantum Machin Learning and Biomimetic Quantum Technologies conference held in Bilbao.

Author contributions
V.S. and D.P. contributed equally to this work. V.S. and E.K. developed the idea and consulted it with D.P., S.B., M.R., and E.S. to design the protocol. V.S., M.G., and M.Ab. developed the algorithm, D.P. performed the experiments under the supervision of E.K. All authors contributed to discussions. V.S., D.P., and E.K. wrote the manuscript, and V.S., S.B., and E.K. revised the final version.

Funding
D. P., M. R. and E. K. acknowledge the support of Ontario's Early Researcher Award (ERA), Canada Research Chairs (CRC), and the European Union's Horizon 2020 Research and Innovation Programme (Q-SORT), grant number 766970. V. S. is grateful for the financial support by Alberta Innovates Grant in Canada, and the Spanish State Research Agency through BCAM Severo Ochoa excellence accreditation SEV-2017-0718 and BERC 2018-2021 program. S.B. acknowledges funding by the Natural Sciences and Engineering Research Council of Canada (NSERC) through its Discovery Grant, funding and advisory support provided by Alberta Innovates through the Accelerating Innovations into CarE (AICE)—Concepts Program, and support from Alberta Innovates and NSERC through Advance Grant. This project is funded [in part] by the Government of Canada. / Ce projet est financé [en partie] par le gouvernement du Canada

Competing interests
The authors declare no competing interests.

Additional information
Supplementary Information The online version contains supplementary material available at https://doi.org/10.1038/s41598-022-25280-5.

Correspondence and requests for materials should be addressed to E.K.

Chapter 5

Conclusions

In the preceding chapters, we presented several works on using structured photons in quantum sensing, quantum imaging, and quantum information.

In Chapter 2, we focused on a couple of works on displacement sensing using structured and correlated photons. In the first work, we demonstrated that probing optically induced transverse displacements using higher-order Hermite-Gauss (HG) modes leads to a linearly enhanced sensitivity with respect to the mode order [74], also showing that projective measurements onto neighboring spatial modes are optimal. We presented a proof-of-principle experimental realization, observing an order-of-magnitude improvement in sensitivity from probing the sample with higher-order Hermite-Gaussian modes. We expect the techniques demonstrated in this work, when combined with efficient detection technologies such as using multi-plane light converters [101], to hold strong promise for the development of compact and precise devices capable of detecting small displacements–particularly in applications involving nano-scale systems, and high-resolution imaging of birefringent samples. We also theoretically derived optimal projective measurements for separation estimation using a bi-photon wave function generated via the SPDC process based on its Schmidt decomposition [75]. The precision in the proposed method is limited by the strength of the spatial correlations inherent in the photon pairs, and the total Fisher information of the separation estimation is proportional to the square root of the Schmidt number of the system. The method offers further enhancement that scales with K compared to ordinary SPADE, which corresponds to the trivial case of $K = 1$. We also implemented the technique experimentally, and performed simulations comparing the precision in our estimates with the case of direct imaging, where we indeed observed at least an order-of-magnitude improvement, especially for near-zero separations. Theoretical and experimental results suggest the potential of using high-dimensional entanglement for further enhancing super-resolution measurements.

Photons structured in their transverse degrees of freedom provide a powerful platform for quantum computing and communication due to the high dimensionality of their Hilbert space. In Chapter 3, we presented a method for nonlocal transfer of high-dimensional computational results using spatial correlations in photon pairs. This approach is promising for future photonic quantum networks, allowing users to access complex computation results performed on a centrally located processor. We experimentally implement this protocol using down-converted photon pairs and demonstrate unitary transfers in both one and two-dimensional transverse momentum spaces. This paves the way for advanced applications in quantum networks, simulation, and computation. Since photons in the down conversion process are also entangled in the orbital angular momentum (OAM) degree of freedom, among others, the same apparatus can also be applied to transfer operations in the OAM space. Using liquid-crystal devices or dielectric meta-surfaces even offers the possibility of transferring unitaries in both the polarization and transverse momentum space. Furthermore, by deliberately introducing controlled losses to selected modes, it becomes possible to investigate non-unitary transformations. Additionally, we demonstrated how structured vector modes imprint a spatial distribution of all four Bell states via Hong-Ou-Mandel interference [86]. Using q-plates, we showed the theoretical and experimental mapping of these states to specific spatial regions. This technique can be extended, for instance, to custom liquid-crystal meta-surfaces [102] such that each Bell state can be mapped onto a two-dimensional Cartesian grid or scaled to higher photon numbers, offering new possibilities in quantum communication, sensing, and the generation of multi-particle entangled states. Additionally, we introduced a versatile approach for simulating noise operations on a qubit through its coupling or interaction with a lattice-like environment [89]. We systematically constructed a global unitary operator that acts on the qubit, which is encoded in the polarization of light, and the environment represented by a set of transverse modes. Tracing out the environment then enacts the targeted noise transformation on the qubit state. Our findings have the potential to assist the study of open quantum systems, and could be readily adapted to simulate arbitrary qubit-environment interactions with a potential extension to multi-qubit systems for studying the behavior of entanglement and discord under noise [103].

In Chapter 4, we focused on a work on quantum imaging and a potential framework for an intelligent quantum imaging system with a novel algorithm for pattern recognition [100]. By interfacing quantum image acquisition directly with a quantum processor, we propose the combined benefits of a quantum imaging system, such as sub-shot noise errors and low illumination requirements, with the speedup of a quantum pattern recognition algorithm. This framework enables a fully quantum image recognition system with potential applications in fields such as medical diagnostics and biological imaging.

APPENDICES

Supplementary Information for:
Quantum Face Recognition Protocol with Ghost Imaging

S1. QUANTUM IMAGING

We elaborate on the experimental details of the image acquisition for the quantum pattern recognition protocol. Spatially correlated photon pairs, usually called signal and idler photons, are generated from a Spontaneous Parametric Down Conversion Process (SPDC) by pumping a nonlinear crystal. Utilizing the position and momentum correlations in these down converted photon pairs, one can non-locally obtain an image of an object that interacted only with the idler photons. The experimental setup we use is similar to a conventional ghost-imaging setup, see Fig. **S1**, with our object being a hologram placed in a Spatial Light Modulator (SLM), a liquid crystal device. We use a 1 GHZ, 100 fs pulsed laser to pump a nonlinear crystal, β-Barium Borate (BBO), for generating a second harmonic output. We then use the second harmonic beam to pump a Type-I bismuth triborate (BiBO) crystal for the down conversion of photon pairs. The generated signal and idler pairs are split into two paths, i.e. the object arm (idler) and the camera arm (signal), via a 50:50 Beamsplitter (BS). The idler photon interacts with the SLM, on which we display the holograms created by superimposing the original face image with a diffraction grating. The grating sends only the desired photons from the incident beam to the the first order, which then are coupled to a Single Mode Fibre (SMF) and sent into a Single Photon Avalanche Diode (SPAD) detector which can be used to trigger the collection of the photons in the Intensified CCD (ICCD) camera. The images obtained that are shown in Fig. 2 were taken with 0.5 s exposure accumulated over 300 frames.

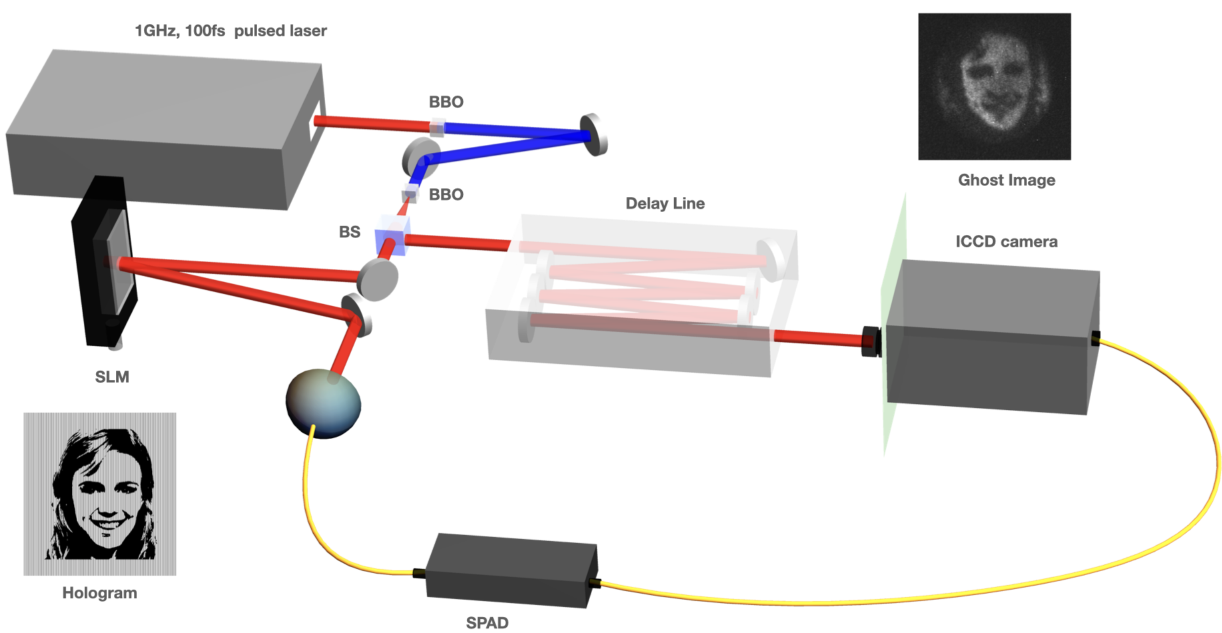

Supplementary Figure S1. Simplified schematic of the experimental setup for Quantum Ghost Imaging. A 1 GHz, 100 fs laser is used to pump a nonlinear crystal (BBO) for second harmonic generation. The second harmonic beam is used to pump a Type-I bismuth triborate (BiBO) crystal for entangled photon pair generation. One of the photons is sent to a Spatial Light Modulator, a liquid crystal device, on which images of human faces are superposed with a diffraction grating. The second photon is sent to a camera through an image preserving delay line where the image of the object is formed. Figure legends: BiBO - 0.5-mm-thick bismuth triborate crystal; BS - Beamsplitter; BS - Beam splitter; SPAD - Single Photon Avalanche Diode; ICCD - Intensified CCD camera.

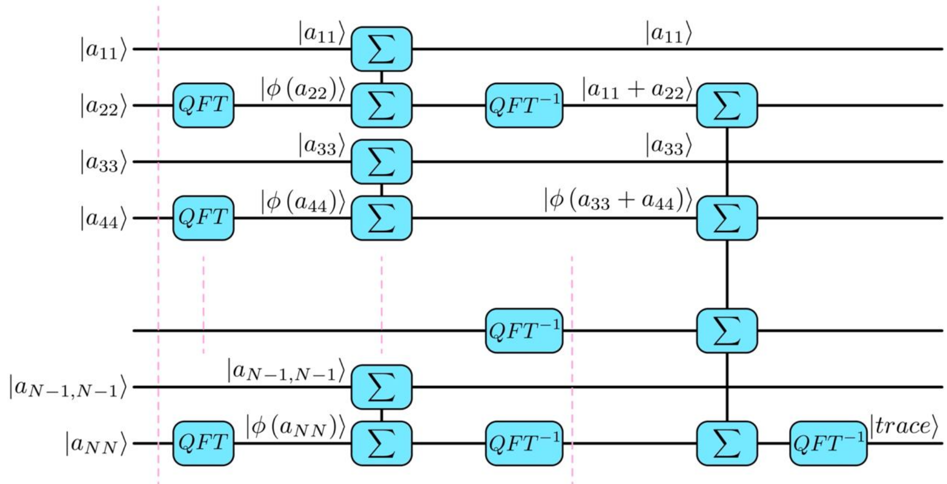

Supplementary Figure S2. Quantum circuit for the trace calculation of sparse matrix.

S2. QUANTUM COMPUTATION OF TRACE

Here, we suggest an adder algorithm [44] to compute the trace of a matrix via adding the diagonal elements of the matrix A. This operator is mainly based on quantum Fourier transform (QFT) and inverse QFT (i.e. QFT^{-1}). The algorithm should process the binary forms of the diagonal. For example, the binary representation of the diagonal elements a_{11} and a_{22} of matrix A are respectively $a_{11} = \alpha_1 2^{n-1} + \alpha_2 2^{n-2} + \ldots + \alpha_n 2^0$ and $a_{22} = \beta_1 2^{n-1} + \beta_2 2^{n-2} + \ldots + \beta_n 2^0$, which are $|a_{11}\rangle = |\alpha_1\rangle \otimes |\alpha_2\rangle \otimes \ldots |\alpha_n\rangle$ and $|a_{22}\rangle = |\beta_1\rangle \otimes |\beta_2\rangle \otimes \ldots |\beta_n\rangle$ in the form of quantum kets. The QFT operation on binary state is $\text{QFT}|a\rangle = \frac{1}{\sqrt{N}} \sum_{k=0}^{N-1} e^{\frac{i2\pi ak}{N}} |k\rangle$ and the operation of QFT^{-1} is $\text{QFT}^{-1}|k\rangle = \frac{1}{\sqrt{N}} \sum_{a=0}^{N-1} e^{\frac{-i2\pi ak}{N}} |a\rangle$[44]. For simplicity, we introduce a representation for QFT as

$$|\Phi(a)\rangle = \text{QFT}|a\rangle = \frac{1}{\sqrt{N}} \sum_{k=0}^{N-1} e^{\frac{i2\pi ak}{N}} |k\rangle,$$

so, we can write

$$\text{QFT}^{-1}|\Phi(a)\rangle = \text{QFT}^{-1}\text{QFT}|a\rangle = |a\rangle.$$

In order to calculate the trace, we need to add all diagonal elements $|a_{11}\rangle + |a_{22}\rangle + \ldots + |a_{NN}\rangle$ to have the ket include the value of trace as $|a_{11} + a_{22} + \ldots + a_{NN}\rangle$. We introduce the operator Σ that adds two elements a_{11} and a_{22} in the form of $|a_{11} + a_{22}\rangle$ as follows:

$$\Sigma(|a_{11}\rangle|\Phi(a_{22})\rangle) = |\Phi(a_{11} + a_{22})\rangle.$$

Then, after the operation of QFT^{-1} we obtain

$$\text{QFT}^{-1}(|\Phi(a_{11} + a_{22})\rangle) = |a_{11} + a_{22}\rangle.$$

By continuation of this method for the all diagonal elements, the trace can be obtained. The quantum protocol for computation of trace is depicted in Fig. S2, in which the input is $|a_{11}\rangle|a_{22}\rangle \ldots |a_{NN}\rangle$ and the output is $|\Phi(a_{11} + a_{22} + \ldots + a_{NN})\rangle = |\Phi(Tr(A))\rangle$. Finally, by an operation of QFT^{-1} we can get $|Tr(A)\rangle$. The whole process based on QFT and QFT^{-1} has a complexity $\log N$.

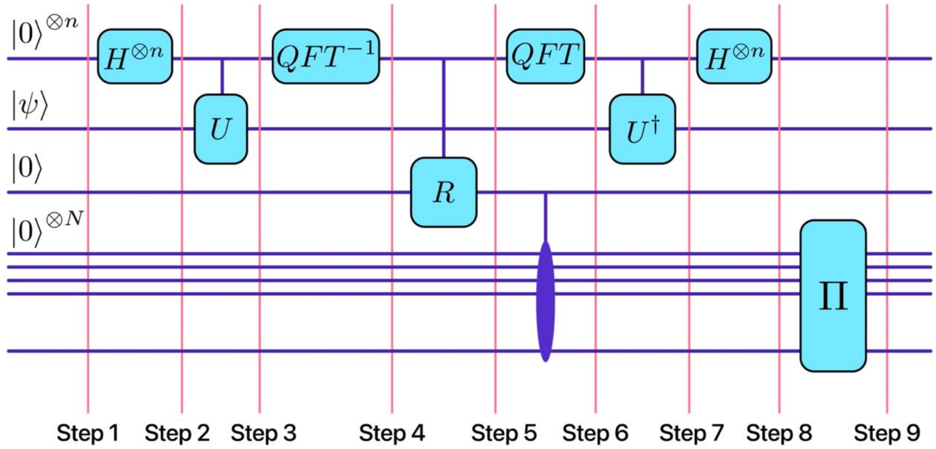

Supplementary Figure S3. Quantum circuit of determinant calculation of sparse matrix

S3. QUANTUM COMPUTATION OF SPARSE MATRIX DETERMINANTS

Our algorithm for computation of determinant is clarified in the following subsections as inputs, algorithm boxes, and algorithm steps:

1. Inputs

- Sparse matrix A
- $|0\rangle^{\otimes n}|\Psi\rangle$ as the input in QPE
- $|0\rangle$ as the ancilla for rotation operator
- $|0\rangle^{\otimes N}$ as the memory register for multiplication operator

2. Algorithm Boxes

- QPE is the quantum phase estimation subroutine composed of $H^{\otimes n}$, CU (i.e. controlled-U) and inverse quantum Fourier transform (QFT^{-1})
- Rotation operation ($\mathbb{R}$)
- (QPE)$^{-1}$ is the inverse operation of QPE, composed of $H^{\otimes n}$, CU† and quantum Fourier transform (QFT)
- Π is a multiplication operation

The matrix A can be exponentiated as the unitary operator $U = e^{\frac{2\pi i A}{2^n}}$ with logarithmic complexity [7] in which n is the precision. This unitary operator is used in the controlled-U (i.e. CU) part of QPE, and $|\Psi\rangle$ is the superposition of the eigenvectors of A in the form of $|\Psi\rangle = \sum \beta_j |u_j\rangle$. Figure S3 is the representation of the quantum protocol for the computation of matrix determinants. The following steps are based on the steps shown in Fig. S3.

STEP 1:
The initial state of the algorithm is:

$$|0\rangle^{\otimes n}|\Psi\rangle|0\rangle|0\rangle^{\otimes N}. \tag{S1}$$

STEP 2:
After the operation of n Hadamard gates, i.e. $H^{\otimes n}$, we have:

$$\frac{1}{2^{\frac{n}{2}}} \sum_{y_1,\ldots,y_n=0}^{1} |y_1 \ldots y_n\rangle|\Psi\rangle|0\rangle|0\rangle^{\otimes N}. \tag{S2}$$

STEP 3:
In this step, let us apply the controlled-U (CU) operation:

$$\frac{1}{2^{\frac{n}{2}}}\sum_{y=0}^{2^n-1}\sum_{j=1}^{N}\beta_j e^{\frac{2\pi i\lambda_j y}{2^n}}|y\rangle|u_j\rangle|0\rangle|0\rangle^{\otimes N}, \tag{S3}$$

where $y=\sum_{l=1}^{n} y_l 2^{n-l}$ and λ_j's are the eigenvalues of matrix A.

STEP 4:
Here, we apply the inverse Fourier Transform,

$$\frac{1}{2^n}\sum_{y=0}^{2^n-1}\sum_{k=0}^{2^n-1}\sum_{j=1}^{N}\beta_j e^{2\pi i\left(\frac{\lambda_j-k}{2^n}\right)y}|k\rangle|u_j\rangle|0\rangle|0\rangle^{\otimes N}. \tag{S4}$$

For a single k among the all possible values, we have $\lambda_j-k=0$, where $\lambda_j=x=k$. The other terms will be set to zero. Thus, the notation k is changed to the notation x:

$$\frac{1}{2^n}\sum_{y=0}^{2^n-1} e^{2\pi i\left(\frac{\lambda_j-x}{2^n}\right)y}=1 \tag{S5}$$

In this case, the state becomes:

$$\sum_{x=0}^{2^n-1}\sum_{j=1}^{N}\beta_j|\lambda_j\rangle|u_j\rangle|0\rangle|0\rangle^{\otimes N}=\sum_{x_1\ldots x_n=0}^{1}\sum_{j=1}^{N}\beta_j|x_1x_2\ldots x_n\rangle|u_j\rangle|0\rangle|0\rangle^{\otimes N},$$

where

$$\lambda_j=\sum_{l=0}^{n}x_l 2^{n-l}=2^n\sum_{l=0}^{n}x_l 2^{-l}=2^n\tilde{\lambda}_j\,.$$

STEP 5:
In this step, we apply the rotation operation $\mathbb{R}_l=e^{\frac{i\sigma_y}{2^l}}$, where σ_y is the Pauli matrix y, which acts on the output of QFT^{-1}:

$$\sum_{x_1\ldots x_n=0}^{1}\sum_{j=1}^{N}\beta_j|x_1\ldots x_n\rangle|u_j\rangle(\sqrt{1-\tilde{\lambda}_j^2}|0\rangle+\tilde{\lambda}_j|1\rangle). \tag{S6}$$

STEP 6:
Applying the quantum Fourier transform (QFT) results in:

$$\frac{1}{2^{\frac{n}{2}}}\sum_{y=0}^{2^n-1}\sum_{j=1}^{N}\beta_j e^{\frac{2\pi i\lambda_j y}{2^n}}|y\rangle|u_j\rangle(\sqrt{1-\tilde{\lambda}_j^2}|0\rangle+\tilde{\lambda}_j|1\rangle). \tag{S7}$$

STEP 7:
In this step, we apply the CU† operator,

$$\frac{1}{2^{\frac{n}{2}}}\sum_{y=0}^{2^n-1}\sum_{j=1}^{N}\beta_j|y\rangle|u_j\rangle(\sqrt{1-\tilde{\lambda}_j^2}|0\rangle+\tilde{\lambda}_j|1\rangle). \tag{S8}$$

STEP 8:
As $|u_j\rangle$'s are known, we repeat the algorithm N times, each time for a specific $|u_j\rangle$, and consequently we obtain the following state:

$$|0\rangle^{\otimes n}|\Psi\rangle\prod_{j=1}^{n}(\sqrt{1-\tilde{\lambda}_j^2}|0\rangle+\tilde{\lambda}_j|1\rangle). \tag{S9}$$

Now, the goal is to measure the multiplication of $\tilde{\lambda}_j$'s in the output of multiplication operation;

$$\prod_{j}^{N}\left(\sqrt{1-\tilde{\lambda}_j^2}|0\rangle+\tilde{\lambda}_j|1\rangle\right)=\left(\sqrt{1-\tilde{\lambda}_1^2}|0\rangle+\tilde{\lambda}_1|1\rangle\right)\ldots\left(\sqrt{1-\tilde{\lambda}_N^2}|0\rangle+\tilde{\lambda}_N|1\rangle\right) \tag{S10}$$

$$=\left(\sqrt{1-\tilde{\lambda}_1^2}\right)\ldots\left(\sqrt{1-\tilde{\lambda}_N^2}\right)|00\ldots0\rangle+\left(\sqrt{1-\tilde{\lambda}_1^2}\right)(\tilde{\lambda}_2)\ldots|0100\ldots0\rangle+\ldots+\overbrace{(\tilde{\lambda}_1)(\tilde{\lambda}_2)\ldots(\tilde{\lambda}_N)}^{\tilde{\lambda}_1\ldots\tilde{\lambda}_N}\overbrace{|111\ldots1\rangle}^{N}. \tag{S11}$$

The coefficient of the state $|\underbrace{11\ldots1}_{N}\rangle$ is the term $\tilde{\lambda}_1\tilde{\lambda}_2\ldots\tilde{\lambda}_N$ in the output of the multiplier, which can be obtained via a weak measurement without collapsing other lines. As $\lambda_j=2^n\tilde{\lambda}_j$, we can obtain the determinant of A (i.e. $\lambda_1\lambda_2\ldots\lambda_N$) via relation $(2^n)^N\tilde{\lambda}_1\tilde{\lambda}_2\ldots\tilde{\lambda}_N=\lambda_1\lambda_2\ldots\lambda_N=det(A)$.

A. Proof of the steps

The proof for each of the eight steps, described above, are given in details in the following expressions.

STEP 2:

$$\begin{aligned}|\Psi_2\rangle&=(H_2^{\otimes n}\otimes\mathbb{I}_N\otimes\mathbb{I}_2\otimes\mathbb{I}_2^{\otimes N})|0\rangle^{\otimes n}|\Psi\rangle|0\rangle|0\rangle^{\otimes N}=\frac{1}{2^{\frac{n}{2}}}\sum_{y=0}^{2^n-1}|y\rangle|\Psi\rangle|0\rangle|0\rangle^{\otimes N}\\&=\frac{1}{2^{\frac{n}{2}}}\sum_{y_1\ldots y_n=0}^{1}|y_1\ldots y_n\rangle|\Psi\rangle|0\rangle|0\rangle^{\otimes N}\end{aligned} \tag{S12}$$

STEP 3:

$$\begin{aligned}|\Psi_3\rangle&=\prod_{l=1}^{n}(\mathbb{I}_2^{\otimes l-1}\otimes|0\rangle\langle0|\otimes\mathbb{I}_2^{\otimes n-l}\otimes\mathbb{I}_N\otimes\mathbb{I}_2\otimes\mathbb{I}_2^{\otimes N}+\mathbb{I}_2^{\otimes l-1}\otimes|1\rangle\langle1|\otimes\mathbb{I}_2^{\otimes n-l}\otimes U^{2^{n-l}}\otimes\mathbb{I}_2\otimes\mathbb{I}_2^{\otimes N})\frac{1}{2^{\frac{n}{2}}}\times\\&\times\sum_{y_1\ldots y_n=0}^{1}|y_1\ldots y_n\rangle\sum_{j=1}^{N}\beta_j|u_j\rangle|0\rangle|0\rangle^{\otimes N}\\&=\frac{1}{2^{\frac{n}{2}}}\sum_{y_1\ldots y_n=0}^{1}\sum_{j=1}^{N}\beta_j\prod_{l=1}^{n}(\mathrm{CU})_l|y_1\ldots y_n\rangle|u_j\rangle|0\rangle|0\rangle^{\otimes N}\\&=\frac{1}{2^{\frac{n}{2}}}(\sum_{y_1\ldots y_n=0}^{1}\sum_{j=1}^{N}\beta_j\prod_{l=1}^{n}(\delta_{0,y_l}+\delta_{1,y_l}e^{2\pi i\tilde{\lambda}_j2^{n-l}})|y_1\ldots y_n\rangle|u_j\rangle|0\rangle)|0\rangle^{\otimes N}\\&=\frac{1}{2^{\frac{n}{2}}}(\sum_{y_1\ldots y_n=0}^{1}\sum_{j=1}^{N}\beta_j\prod_{l=1}^{n}e^{2\pi i\tilde{\lambda}_jy_l2^{n-l}}|y_1\ldots y_n\rangle|u_j\rangle|0\rangle)|0\rangle^{\otimes N}\\&=\frac{1}{2^{\frac{n}{2}}}(\sum_{y_1\ldots y_n=0}^{1}\sum_{j=1}^{N}\beta_je^{2\pi i\tilde{\lambda}_j\sum_{l=1}^{n}y_l2^{n-l}}|y_1\ldots y_n\rangle|u_j\rangle|0\rangle)|0\rangle^{\otimes N}\\&=\frac{1}{2^{\frac{n}{2}}}\sum_{y=0}^{2^n-1}\sum_{j=1}^{N}\beta_je^{2\pi i\tilde{\lambda}_jy}|y\rangle|u_j\rangle|0\rangle|0\rangle^{\otimes N}\end{aligned} \tag{S13}$$

STEP 4:

$$
\begin{aligned}
|\Psi_4\rangle &= (\mathrm{QFT}^{-1} \otimes \mathbb{1}_N \otimes \mathbb{1}_2 \otimes \mathbb{1}_2^{\otimes N})\frac{1}{2^{\frac{n}{2}}}\sum_{y=0}^{2^n-1}\sum_{j=1}^{N}\beta_j e^{2\pi i\tilde{\lambda}_j y}|y\rangle|u_j\rangle|0\rangle|0\rangle^{\otimes N} \\
&= \frac{1}{2^{\frac{n}{2}}}\sum_{y=0}^{2^n-1}\sum_{j=1}^{N}\beta_j e^{2\pi i\tilde{\lambda}_j y}(\mathrm{QFT}^{-1}|y\rangle)|u_j\rangle|0\rangle|0\rangle^{\otimes N} \\
&= \frac{1}{2^{\frac{n}{2}}}\sum_{y=0}^{2^n-1}\sum_{j=1}^{N}\beta_j e^{2\pi i\tilde{\lambda}_j y}(\frac{1}{2^{\frac{n}{2}}}\sum_{k=0}^{2^n-1}e^{-2\pi i\frac{k}{2^n}y}|k\rangle\langle y|y\rangle)|u_j\rangle|0\rangle|0\rangle^{\otimes N} \\
&= \frac{1}{2^n}\sum_{y=0}^{2^n-1}\sum_{k=0}^{2^n-1}\sum_{j=1}^{N}\beta_j e^{2\pi i(\tilde{\lambda}_j-\frac{k}{2^n})y}|k\rangle|u_j\rangle|0\rangle|0\rangle^{\otimes N} \\
&= \frac{1}{2^n}\sum_{y=0}^{2^n-1}\sum_{k=0}^{2^n-1}\sum_{j=1}^{N}\beta_j e^{2\pi i(\frac{\lambda_j-k}{2^n})y}|k\rangle|u_j\rangle|0\rangle|0\rangle^{\otimes N}
\end{aligned}
\tag{S14}
$$

$$
|\Psi_4\rangle = \sum_{x=0}^{2^n-1}\sum_{j=1}^{N}\beta_j|\lambda_j\rangle|u_j\rangle|0\rangle|0\rangle^{\otimes N} = \sum_{x_1\ldots x_n=0}^{1}\sum_{j=1}^{N}\beta_j|x_1x_2\ldots x_n\rangle|u_j\rangle|0\rangle|0\rangle^{\otimes N}
\tag{S15}
$$

STEP 5:

$$
\begin{aligned}
|\Psi_5\rangle &= \prod_{l=1}^{n}(\mathbb{1}_2^{\otimes n-l+1} \otimes |0\rangle\langle 0| \otimes \mathbb{1}_2^{\otimes l} \otimes \mathbb{1}_N \otimes \mathbb{1}_2 \otimes \mathbb{1}_2^{\otimes N} + \mathbb{1}_2^{\otimes n-l+1} \otimes |1\rangle\langle 1| \otimes \mathbb{1}_2^{\otimes l} \otimes \mathbb{1}_N \otimes \mathbb{R}_{n-l}) \otimes \mathbb{1}_2^{\otimes N} \times \\
&\times \sum_{x_1\ldots x_n=0}^{1}|x_1\ldots x_n\rangle\sum_{j=1}^{N}\beta_j|u_j\rangle|0\rangle \\
&= \sum_{x_1\ldots x_n=0}^{1}\sum_{j=1}^{N}\beta_j\prod_{l=1}^{n}(\mathrm{CR})_{n-l+1}|x_1\ldots x_n\rangle|u_j\rangle|0\rangle|0\rangle^{\otimes N} \\
&= \sum_{x_1\ldots x_n=0}^{1}\sum_{j=1}^{N}\beta_j|x_1\ldots x_n\rangle|u_j\rangle(\prod_{l=1}^{n}(\delta_{0,x_{n-l+1}} + \delta_{1,x_{n-l+1}}e^{\frac{i\sigma_y}{2^{n-l+1}}})|0\rangle)|0\rangle^{\otimes N} \\
&= \sum_{x_1\ldots x_n=0}^{1}\sum_{j=1}^{N}\beta_j|x_1\ldots x_n\rangle|u_j\rangle(\prod_{l=1}^{n}e^{i\sigma_y x_{n-l+1}2^{-(n-l+1)}}|0\rangle)|0\rangle^{\otimes N} \\
&= \sum_{x_1\ldots x_n=0}^{1}\sum_{j=1}^{N}\beta_j|x_1\ldots x_n\rangle|u_j\rangle(e^{i\sigma_y\sum_{l=1}^{n}x_{n-l+1}2^{-(n-l+1)}}|0\rangle)|0\rangle^{\otimes N} \\
&= \sum_{x_1\ldots x_n=0}^{1}\sum_{j=1}^{N}\beta_j|x_1\ldots x_n\rangle|u_j\rangle(e^{i\sigma_y\tilde{\lambda}_j}|0\rangle)|0\rangle^{\otimes N}.
\end{aligned}
\tag{S16}
$$

STEP 6:

$$
\begin{aligned}
|\Psi_6\rangle &= (\text{QFT} \otimes \mathbb{I}_N \otimes \mathbb{I}_2 \otimes \mathbb{I}_2^{\otimes N}) \sum_{x_1...x_n=0}^{1} \sum_{j=1}^{N} \beta_j |x_1...x_n\rangle |u_j\rangle (\sqrt{1-\tilde{\lambda}_j^2}|0\rangle + \tilde{\lambda}_j|1\rangle) \\
&= (\text{QFT} \sum_{x_1...x_n=0}^{1} |x_1...x_n\rangle) \sum_{j=1}^{N} \beta_j |u_j\rangle (\sqrt{1-\tilde{\lambda}_j^2}|0\rangle + \tilde{\lambda}_j|1\rangle) \\
&= (\frac{1}{2^{\frac{n}{2}}} \sum_{y=0}^{2^n-1} e^{2\pi i \frac{k}{2^n} y} |y\rangle\langle k| \sum_{x_1...x_n=0}^{1} |x_1...x_n\rangle) \sum_{j=1}^{N} \beta_j |u_j\rangle (\sqrt{1-\tilde{\lambda}_j^2}|0\rangle + \tilde{\lambda}_j|1\rangle) \\
&= (\frac{1}{2^{\frac{n}{2}}} \sum_{y=0}^{2^n-1} e^{2\pi i \frac{k}{2^n} y} |y\rangle \sum_{x_1...x_n=0}^{1} \langle k|x_1...x_n\rangle) \sum_{j=1}^{N} \beta_j |u_j\rangle (\sqrt{1-\tilde{\lambda}_j^2}|0\rangle + \tilde{\lambda}_j|1\rangle) \\
&= (\frac{1}{2^{\frac{n}{2}}} \sum_{y=0}^{2^n-1} e^{2\pi i \frac{k}{2^n} y} |y\rangle \sum_{x_1...x_n=0}^{1} \delta_{k,x_1...x_n}) \sum_{j=1}^{N} \beta_j |u_j\rangle (\sqrt{1-\tilde{\lambda}_j^2}|0\rangle + \tilde{\lambda}_j|1\rangle) \\
&= (\frac{1}{2^{\frac{n}{2}}} \sum_{y=0}^{2^n-1} e^{2\pi i \frac{k}{2^n} y} |y\rangle \delta_{k,\lambda_j}) \sum_{j=1}^{N} \beta_j |u_j\rangle (\sqrt{1-\tilde{\lambda}_j^2}|0\rangle + \tilde{\lambda}_j|1\rangle) \\
&= \frac{1}{2^{\frac{n}{2}}} \sum_{y=0}^{2^n-1} e^{2\pi i \frac{\lambda_j}{2^n} y} |y\rangle \sum_{j=1}^{N} \beta_j |u_j\rangle (\sqrt{1-\tilde{\lambda}_j^2}|0\rangle + \tilde{\lambda}_j|1\rangle) \\
&= \frac{1}{2^{\frac{n}{2}}} \sum_{y=0}^{2^n-1} \sum_{j=1}^{N} \beta_j e^{2\pi i \frac{\lambda_j}{2^n} y} |y\rangle |u_j\rangle (\sqrt{1-\tilde{\lambda}_j^2}|0\rangle + \tilde{\lambda}_j|1\rangle)
\end{aligned} \tag{S17}
$$

STEP 7:

$$
\begin{aligned}
|\Psi_7\rangle &= \prod_{l=1}^{n} (\mathbb{I}_2^{\otimes l-1} \otimes |0\rangle\langle 0| \otimes \mathbb{I}_2^{\otimes n-l} \otimes \mathbb{I}_N \otimes \mathbb{I}_2 \otimes \mathbb{I}_2^{\otimes N} + \mathbb{I}_2^{\otimes l-1} \otimes |1\rangle\langle 1| \otimes \mathbb{I}_2^{\otimes n-l} \otimes (U^\dagger)^{2^{n-l}} \otimes \mathbb{I}_2 \otimes \mathbb{I}_2^{\otimes N}) \times \\
&\times \frac{1}{2^{\frac{n}{2}}} \sum_{y=0}^{2^n-1} \sum_{j=1}^{N} \beta_j e^{2\pi i \frac{\lambda_j}{2^n} y} |y\rangle |u_j\rangle (\sqrt{1-\tilde{\lambda}_j^2}|0\rangle + \tilde{\lambda}_j|1\rangle) \\
&= \frac{1}{2^{\frac{n}{2}}} \sum_{y_1...y_n=0}^{1} \sum_{j=1}^{N} \beta_j e^{2\pi i \frac{\lambda_j}{2^n} y} \prod_{l=1}^{n} (\text{CU}^\dagger)_l |y_1...y_n\rangle |u_j\rangle (\sqrt{1-\tilde{\lambda}_j^2}|0\rangle + \tilde{\lambda}_j|1\rangle) \\
&= \frac{1}{2^{\frac{n}{2}}} (\sum_{y_1...y_n=0}^{1} \sum_{j=1}^{N} \beta_j e^{2\pi i \frac{\lambda_j}{2^n} y} \prod_{l=1}^{n} (\delta_{0,y_l} + \delta_{1,y_l} e^{-2\pi i \lambda_j 2^{n-l}}) |y_1...y_n\rangle |u_j\rangle (\sqrt{1-\tilde{\lambda}_j^2}|0\rangle + \tilde{\lambda}_j|1\rangle) \\
&= \frac{1}{2^{\frac{n}{2}}} (\sum_{y_1...y_n=0}^{1} \sum_{j=1}^{N} \beta_j e^{2\pi i \frac{\lambda_j}{2^n} y} \prod_{l=1}^{n} e^{-2\pi i \lambda_j y_l 2^{n-l}} |y_1...y_n\rangle |u_j\rangle (\sqrt{1-\tilde{\lambda}_j^2}|0\rangle + \tilde{\lambda}_j|1\rangle) \\
&= \frac{1}{2^{\frac{n}{2}}} (\sum_{y_1...y_n=0}^{1} \sum_{j=1}^{N} \beta_j e^{2\pi i \frac{\lambda_j}{2^n} y} e^{-2\pi i \lambda_j \sum_{l=1}^{n} y_l 2^{n-l}} |y_1...y_n\rangle |u_j\rangle (\sqrt{1-\tilde{\lambda}_j^2}|0\rangle + \tilde{\lambda}_j|1\rangle) \\
&= \frac{1}{2^{\frac{n}{2}}} (\sum_{y_1...y_n=0}^{1} \sum_{j=1}^{N} \beta_j e^{2\pi i \frac{\lambda_j}{2^n} y} e^{-2\pi i \tilde{\lambda}_j y} |y_1...y_n\rangle |u_j\rangle (\sqrt{1-\tilde{\lambda}_j^2}|0\rangle + \tilde{\lambda}_j|1\rangle) \\
&= \frac{1}{2^{\frac{n}{2}}} \sum_{y=0}^{2^n-1} \sum_{j=1}^{N} \beta_j e^{\frac{2\pi i}{2^n} (\lambda_j - \lambda_j) y} |y\rangle |u_j\rangle (\sqrt{1-\tilde{\lambda}_j^2}|0\rangle + \tilde{\lambda}_j|1\rangle) \\
&= \frac{1}{2^{\frac{n}{2}}} \sum_{y=0}^{2^n-1} \sum_{j=1}^{N} \beta_j |y\rangle |u_j\rangle (\sqrt{1-\tilde{\lambda}_j^2}|0\rangle + \tilde{\lambda}_j|1\rangle).
\end{aligned} \tag{S18}
$$

STEP 8:

$$|\Psi_8\rangle = (H_2^{\otimes n} \otimes \mathbb{I}_N \otimes \mathbb{I}_2 \otimes \mathbb{I}_2^{\otimes N}) \frac{1}{2^{\frac{n}{2}}} \sum_{y=0}^{2^n-1} \sum_{j=1}^{N} \beta_j |y\rangle |u_j\rangle (\sqrt{1-\tilde{\lambda}_j^2}|0\rangle + \tilde{\lambda}_j|1\rangle)$$

$$= |0\rangle^{\otimes n} \sum_{j=1}^{N} \beta_j |u_j\rangle (\sqrt{1-\tilde{\lambda}_j^2}|0\rangle + \tilde{\lambda}_j|1\rangle) \tag{S19}$$

$$\prod_{j}^{N} \left(\sqrt{1-\tilde{\lambda}_j^2}|0\rangle + \tilde{\lambda}_j|1\rangle\right) = \left(\sqrt{1-\tilde{\lambda}_1^2}|0\rangle + \tilde{\lambda}_1|1\rangle\right) \dots \left(\sqrt{1-\tilde{\lambda}_N^2}|0\rangle + \tilde{\lambda}_N|1\rangle\right)$$

$$= \left(\sqrt{1-\tilde{\lambda}_1^2}\right) \dots \left(\sqrt{1-\tilde{\lambda}_N^2}\right) |00\dots0\rangle + \left(\sqrt{1-\tilde{\lambda}_1^2}\right) (\tilde{\lambda}_2) \dots |0100\dots0\rangle + \dots + \overbrace{(\tilde{\lambda}_1)(\tilde{\lambda}_2)\dots(\tilde{\lambda}_N)}^{\tilde{\lambda}_1 \dots \tilde{\lambda}_N} \overbrace{|111\dots1\rangle}^{N} \tag{S20}$$

Bibliography

[1] M. Planck. "On the Law of Distribution of Energy in the Normal Spectrum". In: *Annalen der Physik* 309.3 (1901), pp. 553–563.

[2] A. Einstein. "On a Heuristic Point of View Concerning the Production and Transformation of Light". In: *Annalen der Physik* 322.6 (1905), pp. 132–148.

[3] N. Bohr. "On the Constitution of Atoms and Molecules". In: *Philosophical Magazine* 26 (1913), pp. 1–25.

[4] E. Schrödinger. "Quantisierung als Eigenwertproblem". In: *Annalen der Physik* 384.4 (1926), pp. 361–376.

[5] W. Heisenberg. "Quantum-theoretical Re-interpretation of Kinematic and Mechanical Relations". In: *Zeitschrift für Physik* 33 (1925), pp. 879–893.

[6] Albert Einstein, Boris Podolsky, and Nathan Rosen. "Can quantum-mechanical description of physical reality be considered complete?" In: *Physical review* 47.10 (1935), p. 777.

[7] R. P. Feynman. "Space-Time Approach to Quantum Electrodynamics". In: *Physical Review* 76.6 (1949), pp. 769–789.

[8] J. Schwinger. "Quantum Electrodynamics I. A Covariant Formulation". In: *Physical Review* 74.10 (1948), pp. 1439–1461.

[9] S. Tomonaga. "On a Relativistically Invariant Formulation of the Quantum Theory of Wave Fields". In: *Progress of Theoretical Physics* 1.2 (1946), pp. 27–42.

[10] Charles H Townes. *The first laser Charles H. Townes*. 2010.

[11] Roy J Glauber. "Coherent and incoherent states of the radiation field". In: *Physical Review* 131.6 (1963), p. 2766.

[12] ECG153347 Sudarshan. "Equivalence of semiclassical and quantum mechanical descriptions of statistical light beams". In: *Physical Review Letters* 10.7 (1963), p. 277.

[13] John F. Clauser. “Experimental distinction between the quantum and classical field-theoretic predictions for the photoelectric effect”. In: *Physical Review D* 9.4 (1974), pp. 853–860. DOI: 10.1103/PhysRevD.9.853.

[14] H Jeff Kimble, Mario Dagenais, and Leonard Mandel. “Photon antibunching in resonance fluorescence”. In: *Physical Review Letters* 39.11 (1977), p. 691.

[15] Frédéric Bouchard et al. “Two-photon interference: the Hong–Ou–Mandel effect”. In: *Reports on Progress in Physics* 84.1 (2020), p. 012402.

[16] Carlton M. Caves. “Quantum-mechanical noise in an interferometer”. In: *Phys. Rev. D* 23.8 (Apr. 1981), pp. 1693–1708. DOI: 10.1103/PhysRevD.23.1693.

[17] R_E Slusher et al. “Observation of squeezed states generated by four-wave mixing in an optical cavity”. In: *Physical review letters* 55.22 (1985), p. 2409.

[18] Ling-An Wu et al. “Generation of squeezed states by parametric down conversion”. In: *Physical review letters* 57.20 (1986), p. 2520.

[19] Bernard Yurke, Samuel L McCall, and John R Klauder. “SU (2) and SU (1, 1) interferometers”. In: *Physical Review A* 33.6 (1986), p. 4033.

[20] Pieter Kok, Hwang Lee, and Jonathan P Dowling. “Creation of large-photon-number path entanglement conditioned on photodetection”. In: *Physical Review A* 65.5 (2002), p. 052104.

[21] T. B. Pittman et al. “Optical Imaging by Means of Two-Photon Quantum Entanglement”. In: *Physical Review A* 52.5 (1995), R3429–R3432.

[22] S. Lloyd. “Enhanced Sensitivity of Photodetection via Quantum Illumination”. In: *Science* 321.5895 (2008), pp. 1463–1465.

[23] M. Tsang, R. Nair, and X.-M. Lu. “Quantum Theory of Superresolution for Two Incoherent Optical Point Sources”. In: *Physical Review X* 6.3 (2016), p. 031033.

[24] M. Paur et al. “Achieving the Ultimate Optical Resolution”. In: *Optica* 3.10 (2016), pp. 1144–1147.

[25] C. W. Helstrom. *Quantum Detection and Estimation Theory*. Academic Press, 1976.

[26] S. L. Braunstein and C. M. Caves. “Statistical Distance and the Geometry of Quantum States”. In: *Physical Review Letters* 72.22 (1994), pp. 3439–3443.

[27] Harry Nyquist. “Certain factors affecting telegraph speed”. In: *Bell System Technical Journal* 3.2 (1924), pp. 324–346.

[28] R. V. L. Hartley. “Transmission of information”. In: *Bell System Technical Journal* 7.3 (1928), pp. 535–563.

[29] Claude E. Shannon. “A mathematical theory of communication”. In: *Bell System Technical Journal* 27.3 (1948), pp. 379–423.

[30] R. W. Hamming. “Error detecting and error correcting codes”. In: *Bell System Technical Journal* 29.2 (1950), pp. 147–160.

[31] John S Bell. “On the einstein podolsky rosen paradox”. In: *Physics Physique Fizika* 1.3 (1964), p. 195.

[32] Stuart J Freedman and John F Clauser. “Experimental test of local hidden-variable theories”. In: *Physical review letters* 28.14 (1972), p. 938.

[33] William K Wootters and Wojciech H Zurek. “A single quantum cannot be cloned”. In: *Nature* 299.5886 (1982), pp. 802–803.

[34] Charles H. Bennett and Gilles Brassard. “Quantum Cryptography: Public Key Distribution and Coin Tossing”. In: *Proceedings of IEEE International Conference on Computers, Systems and Signal Processing*. Bangalore, India, 1984, pp. 175–179.

[35] Peter W Shor. “Algorithms for quantum computation: discrete logarithms and factoring”. In: *Proceedings 35th annual symposium on foundations of computer science*. Ieee. 1994, pp. 124–134.

[36] Anthony E. Siegman. *Lasers*. University Science Books, 1986.

[37] Bahaa E. A. Saleh and Malvin Carl Teich. *Fundamentals of Photonics*. 2nd. Wiley, 2007.

[38] Eliot Bolduc et al. “Exact solution to simultaneous intensity and phase encryption with a single phase-only hologram”. In: *Optics letters* 38.18 (2013), pp. 3546–3549.

[39] Lorenzo Marrucci, Carlo Manzo, and Domenico Paparo. “Optical spin-to-orbital angular momentum conversion in inhomogeneous anisotropic media”. In: *Physical review letters* 96.16 (2006), p. 163905.

[40] Gianluca Ruffato, Michele Massari, and Filippo Romanato. “Generation of high-order Laguerre–Gaussian modes by means of spiral phase plates”. In: *Optics letters* 39.17 (2014), pp. 5094–5097.

[41] Alan E Willner et al. “Optical communications using orbital angular momentum beams”. In: *Advances in Optics and Photonics* 7.1 (2015), pp. 66–106.

[42] Andrew Forbes, Angela Dudley, and Melanie McLaren. “Creation and detection of optical modes for communication applications”. In: *Advances in Optics and Photonics* 8.2 (2016), pp. 200–227.

[43] M Vasnetsov, V Pas’ko, and MS Soskin. “Measurement of the orbital angular momentum spectrum of a light beam”. In: *New Journal of Physics* 7 (2005), p. 46.

[44] Greg G Berkhout et al. “Efficient sorting of orbital angular momentum states of light”. In: *Physical Review Letters* 105.15 (2010), p. 153601.

[45] Mohammad Mirhosseini et al. “Efficient separation of the orbital angular momentum eigenstates of light”. In: *Nature Communications* 4 (2013), p. 2781.

[46] Ebrahim Karimi et al. “Efficient generation and sorting of orbital angular momentum eigenmodes of light by thermally tuned q-plates”. In: *Applied Physics Letters* 94.23 (2009), p. 231124.

[47] Frédéric Bouchard et al. “Measuring azimuthal and radial modes of photons”. In: *Optics express* 26.24 (2018), pp. 31925–31941.

[48] V. Giovannetti, S. Lloyd, and L. Maccone. “Quantum-Enhanced Measurements: Beating the Standard Quantum Limit”. In: *Science* 306.5700 (2004), pp. 1330–1336.

[49] Baris I Erkmen and Jeffrey H Shapiro. “Ghost imaging: from quantum to classical to computational”. In: *Advances in Optics and Photonics* 2.4 (2010), pp. 405–450.

[50] Paul-Antoine Moreau et al. “Ghost imaging using optical correlations”. In: *Laser & Photonics Reviews* 12.1 (2018), p. 1700143.

[51] Giorgio Brida, Marco Genovese, and Ivano Ruo Berchera. “Experimental realization of sub-shot-noise quantum imaging”. In: *Nature Photonics* 4.4 (2010), pp. 227–230.

[52] Mankei Tsang, Ranjith Nair, and Xiao-Ming Lu. “Quantum theory of superresolution for two incoherent optical point sources”. In: *Physical Review X* 6.3 (2016), p. 031033.

[53] Carl W Helstrom. “Quantum detection and estimation theory”. In: *Journal of Statistical Physics* 1 (1969), pp. 231–252.

[54] Alexander S. Holevo. *Probabilistic and Statistical Aspects of Quantum Theory*. Springer, 2011.

[55] Matteo G. A. Paris. “Quantum Estimation for Quantum Technology”. In: *International Journal of Quantum Information* 7.Supp01 (2009), pp. 125–137.

[56] Christian L. Degen, Friedemann Reinhard, and Paola Cappellaro. “Quantum Sensing”. In: *Reviews of Modern Physics* 89.3 (2017), p. 035002.

[57] D. W. Berry and H. M. Wiseman. “Optimal Phase Estimation with a Mach-Zehnder Interferometer”. In: *Physical Review Letters* 85.24 (2000), p. 5098.

[58] R. Demkowicz-Dobrzański, J. Kołodyński, and M. Guţă. “The Elusive Heisenberg Limit in Quantum-Enhanced Metrology”. In: *Nature Communications* 3 (2012), p. 1063.

[59] Sammy Ragy, Marcin Jarzyna, and Rafał Demkowicz-Dobrzański. "Compatibility of Quantum Measurements and Multiparameter Estimation". In: *Physical Review A* 94.5 (2016), p. 052108.

[60] Vittorio Giovannetti, Seth Lloyd, and Lorenzo Maccone. "Advances in quantum metrology". In: *Nature photonics* 5.4 (2011), pp. 222–229.

[61] Lord Rayleigh. "XXXI. Investigations in optics, with special reference to the spectroscope". In: *The London, Edinburgh, and Dublin Philosophical Magazine and Journal of Science* 8.49 (1879), pp. 261–274.

[62] Dieter W. Pohl, Winfried Denk, and Manfred Lanz. "Optical stethoscopy: Image recording with resolution $\lambda/20$". In: *Applied Physics Letters* 44.7 (1984), pp. 651–653. DOI: 10.1063/1.94865.

[63] Mats G. L. Gustafsson. "Surpassing the lateral resolution limit by a factor of two using structured illumination microscopy". In: *Journal of Microscopy* 198 (2000), pp. 82–87. DOI: 10.1046/j.1365-2818.2000.00710.x.

[64] Stefan W. Hell and Jan Wichmann. "Breaking the diffraction resolution limit by stimulated emission: stimulated-emission-depletion fluorescence microscopy". In: *Optics Letters* 19.11 (1994), pp. 780–782. DOI: 10.1364/OL.19.000780.

[65] Wing-Ki Tham, Helena Ferretti, and Aephraim M Steinberg. "Beating Rayleigh's Curse by Imaging Using Phase Information". In: *Physical Review Letters* 118.7 (2017), p. 070801.

[66] Zhen Sheng Tang, Kadir Durak, and Alexander Ling. "Fault-tolerant and finite-error localization for optical point sources". In: *Optics express* 24.19 (2016), pp. 22004–22012.

[67] Clémentine Rouvière et al. "Ultra-sensitive separation estimation of optical sources". In: *Optica* 11.2 (2024), pp. 166–170.

[68] CH Monken, PH Souto Ribeiro, and S Padua. "Transfer of angular spectrum and image formation in spontaneous parametric down-conversion". In: *Physical Review A* 57.4 (1998), p. 3123.

[69] SP Walborn et al. "Spatial correlations in parametric down-conversion". In: *Physics Reports* 495.4 (2010), pp. 87–139.

[70] CC Law and JH Eberly. "Analysis and interpretation of high transverse entanglement in optical parametric down conversion". In: *Physical Review Letters* 92.12 (2004), p. 127903.

[71] Juan P Torres et al. "Quantum spiral bandwidth of entangled two-photon states". In: *Physical Review A* 67.5 (2003), p. 052313.

[72] Filippo M Miatto, Thomas Brougham, and Alison M Yao. "Cartesian and polar Schmidt bases for down-converted photons: How high dimensional entanglement protects the shared information from non-ideal measurements". In: *The European Physical Journal D* 66 (2012), pp. 1–8.

[73] SS Straupe et al. "Angular Schmidt modes in spontaneous parametric down-conversion". In: *Physical Review A—Atomic, Molecular, and Optical Physics* 83.6 (2011), p. 060302.

[74] Dilip Paneru, Alessio D'Errico, and Ebrahim Karimi. "Transverse distance estimation with higher-order Hermite-Gauss modes". In: *Physical Review A* 113.1 (2026), p. L011702.

[75] F. Grenapin et al. "Superresolution enhancement in biphoton spatial-mode demultiplexing". In: *Physical Review Applied* 20 (Aug. 2023), p. 024077. DOI: 10.1103/PhysRevApplied.20.024077.

[76] Chong-Ki Hong, Zhe-Yu Ou, and Leonard Mandel. "Measurement of subpicosecond time intervals between two photons by interference". In: *Physical review letters* 59.18 (1987), p. 2044.

[77] Chuan Wang et al. "Quantum secure direct communication with high-dimension quantum superdense coding". In: *Physical Review A—Atomic, Molecular, and Optical Physics* 71.4 (2005), p. 044305.

[78] Paul G Kwiat et al. "New high-intensity source of polarization-entangled photon pairs". In: *Physical Review Letters* 75.24 (1995), pp. 4337–4341.

[79] Thomas Monz, Kil Hwan Kim, et al. "Realization of universal quantum gate sets with trapped ions". In: *Physical Review Letters* 102.4 (2009), p. 040501.

[80] Ramiros Barends, Julian Kelly, Anthony Megrant, et al. "Superconducting quantum circuits at the surface code threshold for fault tolerance". In: *Nature* 508.7497 (2014), pp. 500–503.

[81] Hannes Bernien, Bas Hensen, et al. "Heralded entanglement between solid-state qubits separated by three metres". In: *Nature* 497.7447 (2013), pp. 86–90.

[82] Daniel FV James et al. "Measurement of qubits". In: *Physical Review A* 64.5 (2001), p. 052312.

[83] Charles H Bennett et al. "Teleporting an unknown quantum state via dual classical and Einstein-Podolsky-Rosen channels". In: *Physical Review Letters* 70.13 (1993), pp. 1895–1899.

[84] Charles H Bennett and Stephen J Wiesner. "Communication via one- and two-particle operators on Einstein-Podolsky-Rosen states". In: *Physical Review Letters* 69.20 (1992), pp. 2881–2884.

[85] Marek Zukowski et al. ""Event-ready-detectors" Bell experiment via entanglement swapping". In: *Physical Review Letters* 71.26 (1993), pp. 4287–4290.

[86] Xiaoqin Gao et al. "Generation of the complete Bell basis via Hong-Ou-Mandel interference of vector modes". In: *Physical Review A* 112.1 (2025), p. 012215.

[87] Michael A. Nielsen and Isaac L. Chuang. *Quantum Computation and Quantum Information*. 10th Anniversary Edition. Cambridge University Press, 2010.

[88] Dilip Paneru et al. "Nonlocal transfer of high-dimensional unitary operations". In: *Quantum* 9 (2025), p. 1855.

[89] Francesco Di Colandrea et al. "Engineering qubit dynamics in open systems with photonic synthetic lattices". In: *Physical Review Research* 7.2 (2025), p. 023236.

[90] Marco Genovese. "Real applications of quantum imaging". In: *Journal of Optics* 18.7 (2016), p. 073002.

[91] Omar S Magana-Loaiza and Robert W Boyd. "Quantum imaging and information". In: *Reports on Progress in Physics* 82.12 (2019), p. 124401.

[92] Agedi N Boto et al. "Quantum interferometric optical lithography: exploiting entanglement to beat the diffraction limit". In: *Physical Review Letters* 85.13 (2000), p. 2733.

[93] M. Genovese. "Real applications of quantum imaging". In: *Journal of Optics* 18.7 (2016), p. 073002. DOI: 10.1088/2040-8978/18/7/073002.

[94] Miles J Padgett and Robert W Boyd. "An introduction to ghost imaging: quantum and classical". In: *Philosophical Transactions of the Royal Society A: Mathematical, Physical and Engineering Sciences* 375.2099 (2017), p. 20160233.

[95] A. Gatti et al. "Ghost imaging with thermal light: Comparing entanglement and classical correlation". In: *Physical Review Letters* 93.9 (2004), p. 093602. DOI: 10.1103/PhysRevLett.93.093602.

[96] Kam Wai Clifford Chan, Malcolm N O'Sullivan, and Robert W Boyd. "Two-color ghost imaging". In: *Physical Review A—Atomic, Molecular, and Optical Physics* 79.3 (2009), p. 033808.

[97] Vladimir Katkovnik and Jaakko Astola. "Compressive sensing computational ghost imaging". In: *Journal of the Optical Society of America A* 29.8 (2012), pp. 1556–1567.

[98] Lov K. Grover. “A fast quantum mechanical algorithm for database search”. In: *Proceedings of the 28th Annual ACM Symposium on Theory of Computing (STOC)*. Philadelphia, PA, USA, 1996, pp. 212–219.

[99] Don Coppersmith. “An approximate Fourier transform useful in quantum factoring”. In: *arXiv preprint quant-ph/0201067* (2002).

[100] V. Salari et al. “Quantum face recognition protocol with ghost imaging”. In: *Scientific Reports* 12 (2022). DOI: 10.1038/s41598-022-25280-5.

[101] Guillaume Labroille et al. “Efficient and mode selective spatial mode multiplexer based on multi-plane light conversion”. In: *Optics express* 22.13 (2014), pp. 15599–15607.

[102] Alessio D’Errico et al. “Two-dimensional topological quantum walks in the momentum space of structured light”. In: *Optica* 7.2 (2020), pp. 108–114.

[103] Ting Yu and JH Eberly. “Sudden death of entanglement”. In: *Science* 323.5914 (2009), pp. 598–601.